DESIGN OF A 5 DEGREE OF FREEDOM KINEMATIC STAGE FOR THE DUAL CRYSTAL BACKLIGHTER IMAGER DIAGNOSTIC

A Thesis

presented to

the Faculty of California Polytechnic State University,

San Luis Obispo

In Partial Fulfillment

of the Requirements for the Degree

Master of Science in Mechanical Engineering

by

Nicholas Nguyen

June 2020

COMMITTEE MEMBERSHIP

TITLE: Design of a 5 Degree of Freedom Kinematic Stage for the Dual Crystal Backlighter Imager Diagnostic

AUTHOR: Nicholas Nguyen

DATE SUBMITTED: June 2020

COMMITTEE CHAIR: Lauren Cooper, Ph.D.
Professor of Mechanical Engineering

COMMITTEE MEMBER: Joseph Mello, Ph.D.
Professor of Mechanical Engineering

COMMITTEE MEMBER: Jonathan Fry, M.S.
LLNL National Ignition Facility
Senior Mechanical Engineer

ABSTRACT

Design of a 5 Degree of Freedom Kinematic Stage for the Dual Crystal Backlighter Imager Diagnostic

Nicholas Nguyen

The National Ignition Facility (NIF) is home to the world's most energetic laser. The facility is one of the leading centers in inertial confinement fusion (ICF) experiments to research and understand sustainable fusion energy. To fully document and understand the physics occurring during experiments, precise diagnostics are used for a wide range of purposes. One diagnostic, the crystal backlighter imager (CBI), allows for X-ray imaging of the target at late stages of its implosion.

The aim of this project was to increase the current capabilities of the CBI diagnostic with the addition of a second crystal. This thesis focuses on the design development of the 5 degrees of freedom precision stages used to align each of the crystals. The motivations for the addition of a second crystal are covered in the introduction. A ray tracing model was generated to explore the required range of travel for both crystals, as well as explore potential effects of transitioning to a two-crystal system. The requirements of the precision stage are outlined based on the flaws of the current stage and areas with desired improvements. A dynamic analysis was performed on modified supporting hardware for CBI, to determine areas of interest in redesigning components for the two-crystal system. Further research is performed on commercial and literature methods used to design precision optomechanical stages. Finally, the design development is documented outlining the considered options, modifications to the existing system, and the proposed design solution. A design is proposed that meets the project requirements set at the beginning of design development.

ACKNOWLEDGMENTS

This work was performed under the auspices of the U.S. Department of Energy by Lawrence Livermore National Laboratory under Contract DE-AC52-07NA27344. This work was reviewed through LLNL's information management process and was assigned a release number of LLNL-MI-811413.

Thanks to:

- Dr. Lauren Cooper

  Thank you for being my thesis adviser. Your passion and excitement in helping your students grow is unparalleled. Your enthusiasm for taking on new and challenging projects such as this, drove me to produce a thesis I can be proud of.

- My Family

  Thank you Dad for being a constant role model in my life both as an engineer and as a person. I appreciated and valued every phone call we had, and your constant words of encouragement to get me through my Masters program. Thank you Mom for always being there for me and letting me share my graduation date with your 50th birthday. Thank you for sending me home with eggrolls to keep my homesickness at bay and for always supporting me when I am feeling down. Thank you Andrew for welcoming me into your community of friends with open arms. I will cherish the times spent playing games and laughing over the weirdest things.

- Nathaniel Thompson

  Thank you for taking me under your wing and helping me grow exponentially as an engineer through the course of this thesis. I felt like I could come to you with any question and you would have the right answer to lead me down the path to success. I look forward to working together in the future and developing a three crystal system when the time comes.

- Gareth Hall

  Thank you for having the patience to explain any and all concepts I struggled with learning during this project. Your sense of humor and optimism made working on this thesis an unforgettable experience and I look forward to the many opportunities of working with you again.

- Jon Fry

  Thank you for introducing me to the vast opportunities present at LLNL and at the NIF. I appreciated all the advice you gave me to advance in my career and to eventually land a full-time position at the Lab.

- Dr. Joseph Mello

  Thank you for taking the time to help guide me through some of the tough analysis challenges I faced during this thesis. I appreciated your help in brainstorming many different design concepts when I was unsure how to move forward.

- Sam Clements

  Thank you for taking the time to introduce and teach me all about debris wind analysis. I appreciated the time you spent outside your work to mentor me and to always let me squeeze in one ”last” simulation before the weekend.

- Jay Ayers

  Thank you for welcoming me into the group and treating me like I have been with the team for years. I look forward to being officially part of the group this Summer and the opportunities awaiting me.

- Trey

  Thank you for constantly pushing me to improve myself throughout my time here at Cal Poly. I appreciated all the time you spent helping me refine my thesis and giving me a vote of confidence going into my defense.

- My Friends

  Thank you to all my friends that have supported me throughout the years. Thank you especially to those who helped refine the early chapters of this thesis.

- Andrew Guenther

  Thank you for uploading this Latex template.

TABLE OF CONTENTS

CHAPTER

APPENDICES

LIST OF TABLES

Table Page

LIST OF FIGURES

LIST OF ACRONYMS

CMM	Coordinate Measuring Machine
CBI	Crystal Backlighter Imager
DOF	Degree of Freedom
DCBI	Dual Crystal Backlighter Imager
EMP	Electromagnetic Pulse
FOV	Field of View
HGXD	Hardened Gated X-Ray Detector
hSLOS	hardened Single Line of Sight
ICF	Inertial Confinement Fusion
MEMS	Micro-Electronic-Mechanical Systems
NIF	National Ignition Facility
PSM	Point Source Microscope
SLOS	Single Line of Sight
TCC	Target Chamber Center

Chapter 1

INTRODUCTION

The objective of this project was to design a kinematic stage capable of moving a pair of X-ray optics in 5 degrees of freedom (DOF). This newly designed stage would serve as an upgrade on the current capabilities of an existing system. The creation of this design will allow for new and exciting experiments to be performed at the National Ignition Facility (NIF). The design development was tracked throughout this thesis, ranging from background research on common optomechanical stages to analyses to define the range of motion of the stage and the unique loading conditions specific to the NIF.

1.1 Background on the NIF

Since the early 1960s, scientists across the world have been exploring the possibility of generating energy the same way stars do in the Universe [1]. Today, facilities across the globe are researching methods to achieve self-sustaining fusion energy, an achievement that would allow for a clean energy source to be utilized by mankind. One facility in particular, the National Ignition Facility, is home to the most energetic laser in the world. One of the primary missions of the NIF is to reach ignition, which is defined as having a net gain in energy from the fusion reaction [2]. Achieving ignition is not a trivial task, as conditions need to be controlled precisely for self-sustaining fusion reactions to occur. Therefore, advanced diagnostics are necessary to properly measure and investigate several factors during an experiment. One of these diagnostics is the Crystal Backlighter Imager (CBI), which produces radiographic images of experiments at the NIF.

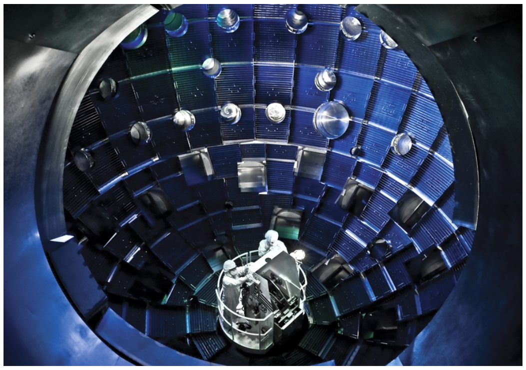

Figure 1.1: Operators inside the Target Chamber at the NIF [3]

In 2009, the NIF was officially established and commissioned to research inertial confinement fusion (ICF). ICF attempts to achieve a fusion reaction by imploding a spherical capsule containing fuel (generally a combination of deuterium and tritium) by heating the capsule in an X-ray bath. Significantly larger than previous facilities, the NIF consists of 192 individual beam paths capable of delivering almost 2 MJ of laser energy into the target chamber [4]. The NIF uses the indirect-drive approach, in which the lasers enter a hohlraum (a gold or uranium cylinder, shown in Figure 1.2) where the laser energy is converted into X-rays.

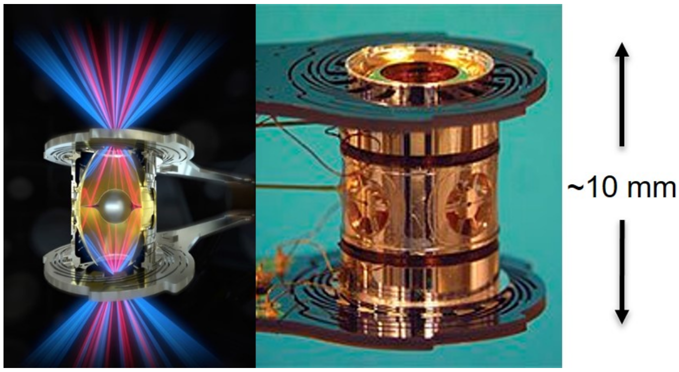

Figure 1.2: Hohlraum Models Rendering of Hohlraum and Laser Light (Left) [5], Manufactured Hohlraum (Right) [6]

The X-rays radiate from the inner walls of the hohlraum to heat the fuel capsule located at its center and causes the outer surface of the capsule to expand. Due to the rapid expansion, there is an equal and opposite action that rapidly compresses the inside of the capsule. This compression rapidly heats and pressurizes the fuel inside the capsule, creating fusion conditions and the release of energy [7]. Figure 1.3 highlights this process in several stages, presenting the capsule changes during the experiment.

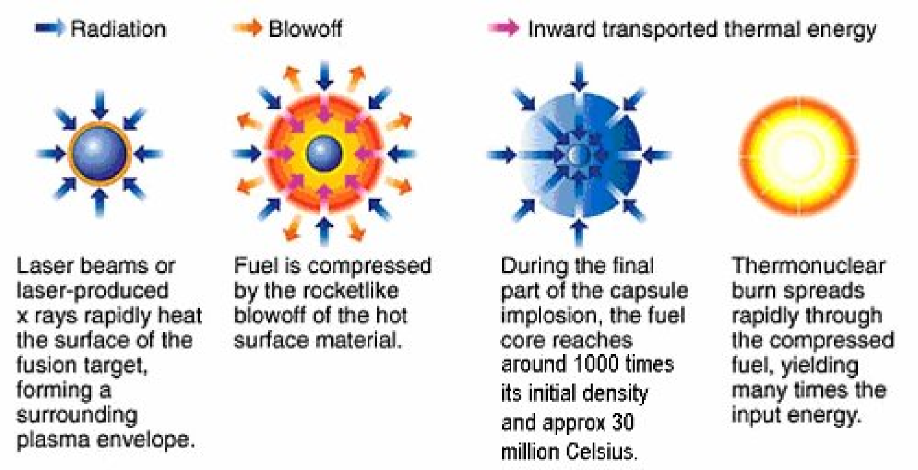

Figure 1.3: Inertial Confinement Fusion Process [7]

Indirect drive methods are especially appealing due to the uniform heating produced by the X-ray bath from the radiating hohlraum walls. The indirect-drive approach to ICF is more inefficient than the direct-drive method, in which the laser is directly shot at the capsule and more of the laser energy directly contributes to the capsule implosion. However, it is much more difficult to drive the capsule uniformly with the direct-drive approach. Facilities such as the OMEGA laser in Rochester utilize the direct-drive approach to ICF [8]. The NIF also performs some work using the direct-drive method, but the vast majority of experiments at the NIF use the indirect-drive approach.

The capsule behavior in the last stages of the implosion plays a key factor in the success of an experiment. This includes the shape of the capsule during the implosion, its overall stability and if any mixing occurs between the capsule ablator (the material that is blown off to drive the implosion) and the fuel itself. To observe these factors, X-ray radiography is used.

1.2 Background on CBI and X-ray Radiography

Previous methods to capture images of the capsule during implosion used backlit pinhole systems [9]. Illustrated in Figure 1.4, a backlighter is positioned behind the target and is shot with laser light. The backlighter emits X-rays with some X-rays passing through the target reaching the pinhole array. The pinholes act as a simple optic (capable of producing an image) and project a shadow image of the target onto the camera. This is analogous to having an X-ray of a bone at a hospital. The desired image is of the projected shadow of the object, where the light/dark regions of the image can reveal how many X-rays passed through the object to the camera.

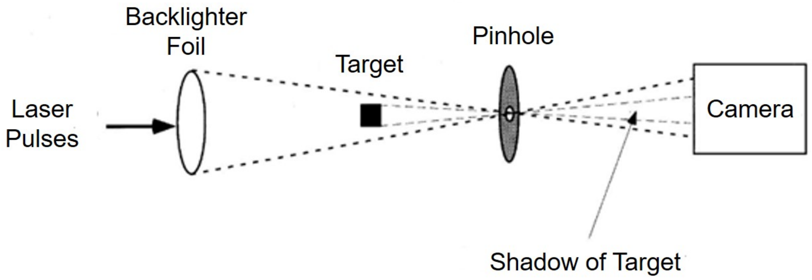

Figure 1.4: Example of a Pinhole Backlighter Radiography Setup [9]

One of the primary issues with this technique occurs during the later stages of the capsule implosion. The fuel inside the capsule begins to self-emit X-rays. The pinhole array can be filtered to remove a wide range of the self-emitted rays but is still broadband in nature [10]. The X-rays produced by the backlighter are within a narrow band of energy (typically atomic line emission) that is easily overpowered by the broadband self-emission from the fuel. Looking at Figure 1.5, the black curve represents the self-emission spectrum of a capsule, and the red-shaded region represents the range of X-ray energies that a filtered pinhole is sensitive to. The area under the black curve in this red-shaded region therefore represents the amount of self-emission X-rays that will be present in the image produced by the pinhole. It is clear that the amount of emitted X-rays from the backlighter (represented by the area under the narrow blue line) would easily be overpowered from the self-emission of the capsule.

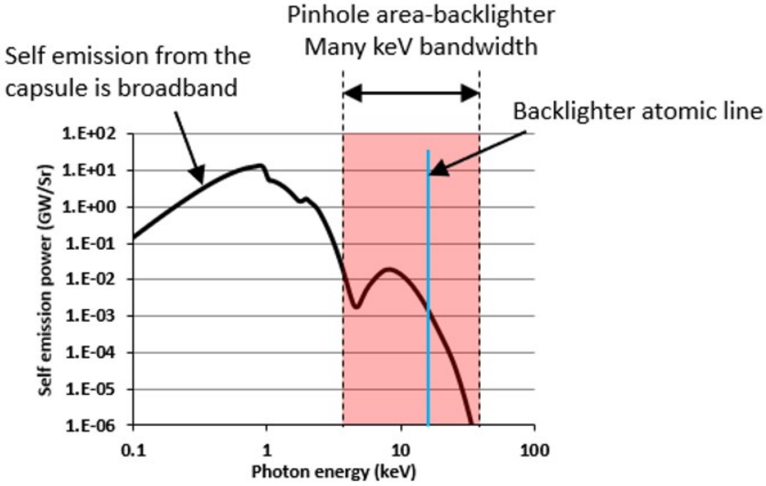

Figure 1.5: Accepted Bandwidth of X-rays from a Pinhole Array Setup where the self-emission X-rays dominate over the backlighter atomic line [10]

As a result, at later stages of the implosion the self-emission overwhelms and contaminates the radiograph, making it impossible to discern the behavior of the capsule. An example of this problem is shown in the image on the right in Figure 1.7.

To combat this, if the imaging technique has a narrower bandwidth that is centered on the backlighter atomic line, it would be possible for the backlighter X-rays to dominate. This would allow for a much clearer image at later points in time minimizing the amount of self-emission X-rays in the image. This can be achieved through a different imaging technique that uses X-ray Bragg reflection from a spherically-bent crystal, the method which CBI uses. The crystal acts as a filter that narrows the accepted bandwidth of X-rays, allowing for the backlighter emission line to dominate over the self-emission of the fuel capsule [11]. On the right side of Figure 1.6, the dashed vertical lines show the narrow range of accepted bandwidth, closely centered to the backlighter atomic line. Over this very narrow bandwidth, the amount of emitted X-rays from the backlighter line (blue-shaded area) dominates the self-emission.

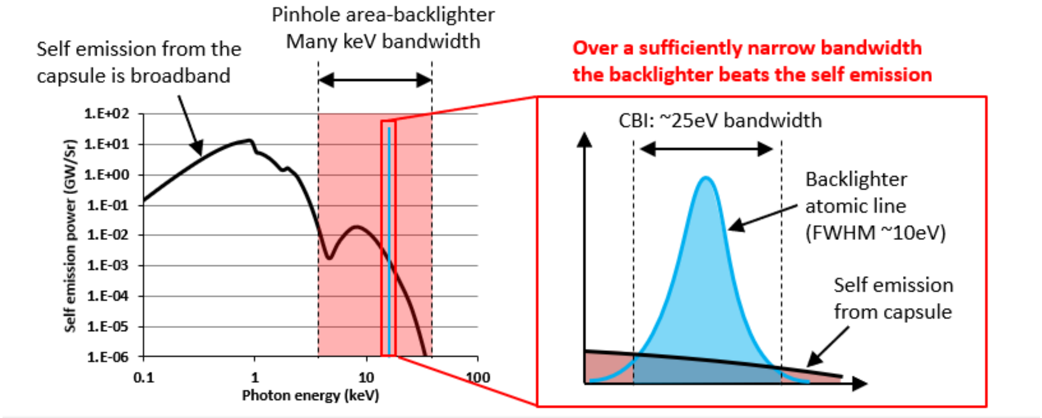

Figure 1.6: CBI Accepted Bandwidth to Filter out Self-Emission from the Fuel Capsule [10]

The effect of this narrow bandwidth on the images produced by CBI in comparison to the pinhole array can be seen in Figure 1.7, where the CBI image is shown on the left. The CBI produced image eliminates most of the self-emission noise compared to the pinhole setup.

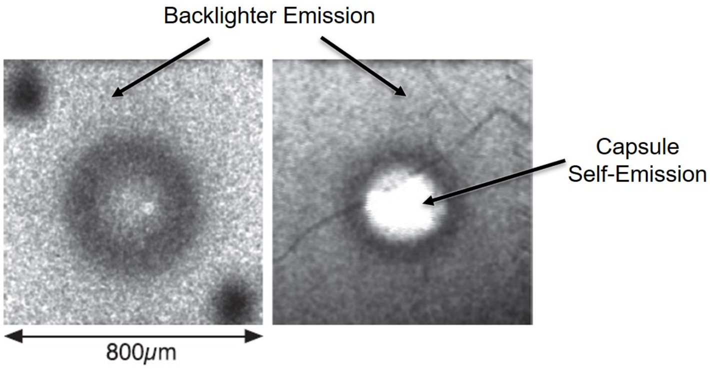

Figure 1.7: Capsule Image Produced by CBI (Left), Capsule Image Produced by Pinhole Array Setup (Right) [11]

Bragg-reflection is the crux of CBI's effectiveness in creating a narrow bandwidth of accepted wavelengths. When waves scatter off atoms on different planes of a crystalline lattice, the waves can constructively or destructively interfere with one another, shown in Figure 1.8. The waves will constructively interfere at a wavelength determined by Bragg's Law:

$$n\lambda = 2d\sin(\theta) \tag{1.1}$$

Where n is an integer, λ is the wavelength, d is the spacing between atomic planes and θ is the Bragg angle. The Bragg angle is defined as the angle between the incident ray and the atomic plane. If this relation holds true, X-rays at this specific wavelength will constructively interfere and be reflected.

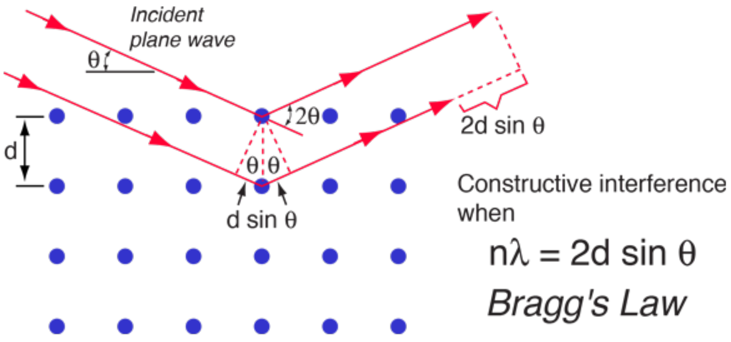

Figure 1.8: Example of Bragg Reflection [12]

Crystals are chosen to match a given wavelength and thus create a narrow bandwidth of accepted X-rays. For most experiments the wavelength is that of the backlighter atomic line, and the Bragg angle must be close to 90° (typically 85-88° is acceptable for CBI) to achieve a well-focused image. As a result, a crystal must be chosen which has a *d*-spacing that satisfies the Bragg condition for these values. While one of the crystal's main functions is its filtering properties through Bragg-reflection, the spherical-bent crystals also act as a focusing optic and behaves similar to a concave mirror to form an image.

High spatial resolution is required to image ICF capsule implosions, and one requirement for high resolution imaging when using crystals is a near-perfect crystal lattice. Therefore, for the NIF crystal imaging system, silicon is the preferred crystal material since near-perfect mono-crystalline silicon has been made readily available by the electronics industry. To achieve different atomic plane spacing, the crystals can be cut at specific angles. These angles are commonly defined through the Miller Index. With this method the same material can be used, but the atomic spacing can be varied depending on the cut and orientation of the front surface depicted in Figure 1.9.

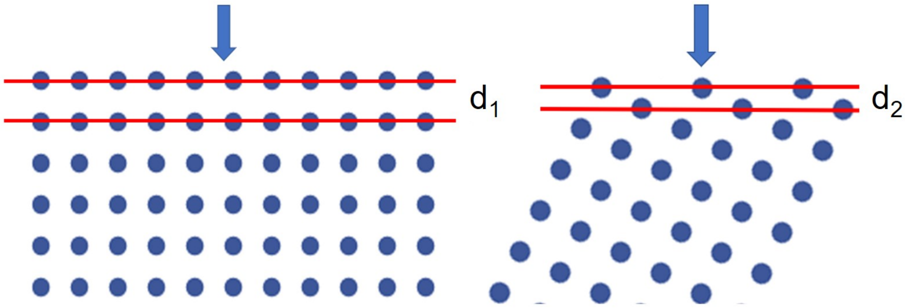

Figure 1.9: Examples of different plane spacing (d), depending on surface cut and orientation

1.3 CBI Diagnostic

To utilize crystal Bragg-reflection to make a well-focused image, the system must operate at near normal incidence (i.e. θ must be close to 90°). In this case, the crystal needs to be positioned on the opposite side of the target relative to the backlighter and the detector. In experiments, the target is located in the same position inside the target chamber, known as target chamber center (TCC). The X-rays are generated from the backlighter (driven by a laser pulse) and pass through the target. The X-rays that reflect off the crystal travel back past the target and onto the detector. A simplified representation of this setup is shown in Figure 1.10.

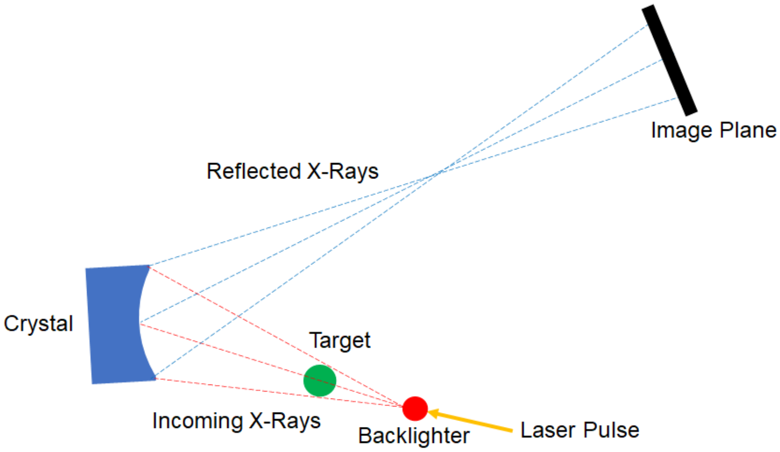

Figure 1.10: Basic Representation of Crystal Bragg-Reflection Radiography Setup

This geometry, in which the detector and crystal are on opposite sides of the target, means that CBI has a unique design amongst NIF diagnostics: the CBI "snout" attaches onto a detector with the crystal mounted on an arm that curves around the target to position it on the opposite side, as shown in Figure 1.11.

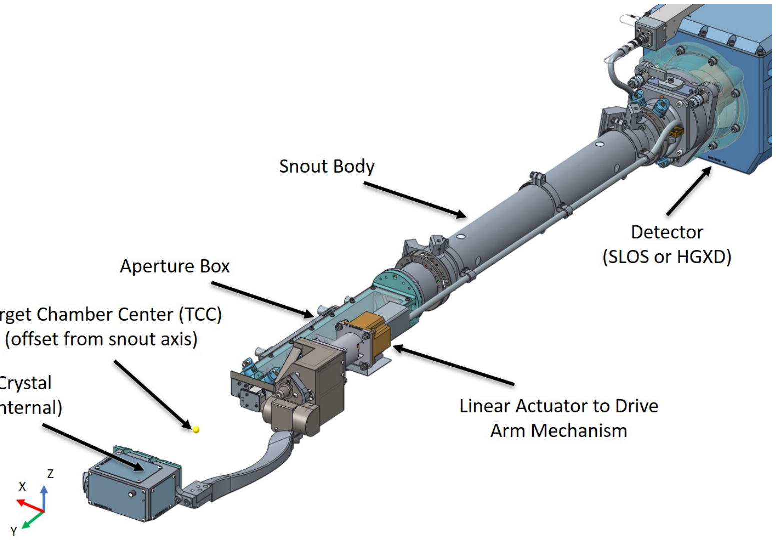

Figure 1.11: 2nd Generation CBI Diagnostic

Figure 1.12 contains a more detailed representation of the Bragg-reflection method with the physical CBI hardware. The backlighter is attached to the target and driven by the NIF laser to produce the X-rays. Precise alignment of the crystal is required to allow for the reflected X-rays to land on the X-ray sensitive areas of the detectors located behind CBI.

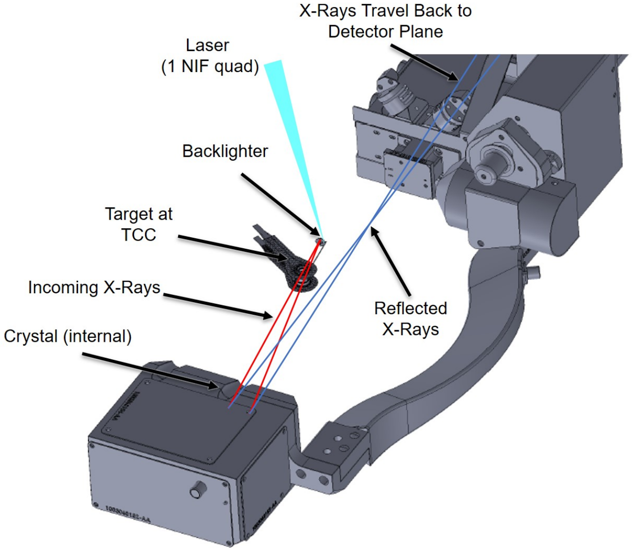

Figure 1.12: Detailed Representation of Crystal Bragg-Reflection with the CBI diagnostic

Currently, one crystal is used in CBI. Adding more crystals using the current hardware is not possible due to the large size of the stage used to align the crystal. The stage can align the stage in 5 degrees of freedom (XYZ translations and pitch and yaw rotations). In Figure 1.13, the current stage setup is shown inside the housing.

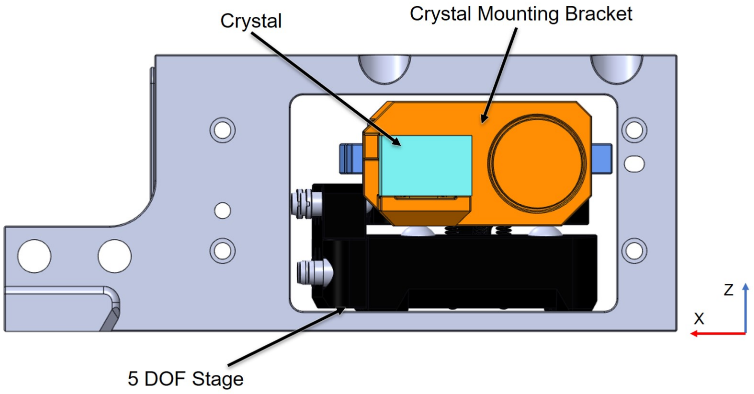

Figure 1.13: Crystal Mounting Scheme in CBI Housing

The focus of this project is to upgrade the current capabilities of the CBI diagnostic. This upgrade focuses on the addition of a second crystal within the housing to allow scientists to perform a multitude of new experiments to understand the capsule behavior better.

1.4 Motivations for a 2^{nd} Crystal

Upgrading the current CBI to allow for 2 crystals will provide opportunities for brand new, sophisticated measurement techniques that are not possible with a single crystal. These 2-crystal techniques will allow aspects of the capsule implosion to be measured that will be extremely valuable to understanding the capsule behavior. With this information, physicists at the NIF can improve the capsule performance to gradually step closer to achieving ignition. These different techniques are not limited to ICF experiments but can be extremely valuable in a wide range of other physics experiments performed at the NIF. A couple of these 2-crystal techniques and experiments are outlined below.

1. Multiple images at different points in time

One of the major disadvantages from the CBI diagnostic in comparison to the pinhole backlighter system is that CBI is limited on the amount of images captured during an experiment. This is partly due to the cameras used to capture the radiographic images, as some are only able to take one image per shot. For a pinhole setup, it is simple enough to add and manufacture additional holes to produce several more images. However, for a crystal setup adding an additional crystal introduces new complications for alignment and packaging just to produce another image. With the addition of another crystal it would be possible to double the number of images captured during a shot, significantly increasing the accuracy with which the evolution of a capsule implosion can be measured/imaged.

2. Subtractive Imaging technique

While CBI is able to narrow the bandwidth of accepted wavelengths to limit the impact of self-emission, some self-emission can still be present at later stages of a shot if it is very intense. One particular experimental configuration that could be performed with a dual crystal setup involves capturing two images at the same energy level to produce one clean image. The experiment would be setup with two crystals with the same Bragg angle and desired reflected energy level. However, only one crystal would have an assigned backlighter. The two images would both contain the same self-emission signal, but only one would contain the backlighter signal, and so by subtracting one from the other a clean, self-emission-free radiograph can be produced. An illustration of this concept is shown below in Figure 1.14.

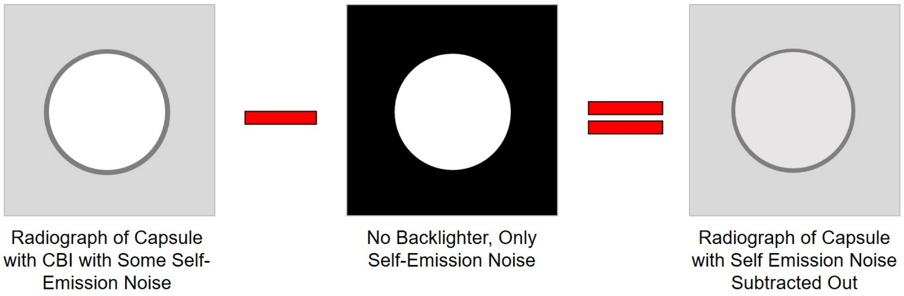

Figure 1.14: Simplified Representation of Subtracting Self-Emission Noise from CBI Radiographs

Being able to subtract the self-emission X-rays allows for images to be taken at later points of time during the implosion, where self-emission begins to introduce too much unwanted signal into the radiographs.

1.5 Current Stage Background

One of the challenges with deploying CBI is to ensure that proper alignment is achieved when the diagnostic is inserted into the target chamber. The overall budget for how accurately the crystal must be positioned in the chamber is close to 200 μm, which includes uncertainty in the insertion of the diagnostic into the chamber paired with the physical alignment of the crystal inside the diagnostic housing. The current setup is capable of meeting the specific alignment budget as the diagnostic is able to position itself better than 150 μm at 2σ uncertainty to the specified location. The current stage can position the crystal to an accuracy of close to 5 μm. The alignment of the crystal is performed offline outside of the target chamber. A stage with high resolution is necessary to ensure proper alignment of the crystal and stay within the alignment budget. Currently, CBI uses a commercial stage to position the single crystal within the housing. The current stage is not capable of positioning two separate crystals independently. Due to its size, only one stage is capable of being packaged in the current housing, so the need for designing a new stage to align both crystals is required.

The CBI diagnostic currently utilizes a 5 DOF linear stage developed by Thorlabs [13]. The stage is capable of translating in the principle XYZ directions and is able to pitch and yaw the top surface about the center of the primary stage. The stage is actuated through a set of 5 fine pitch screws shown in Figure 1.15.

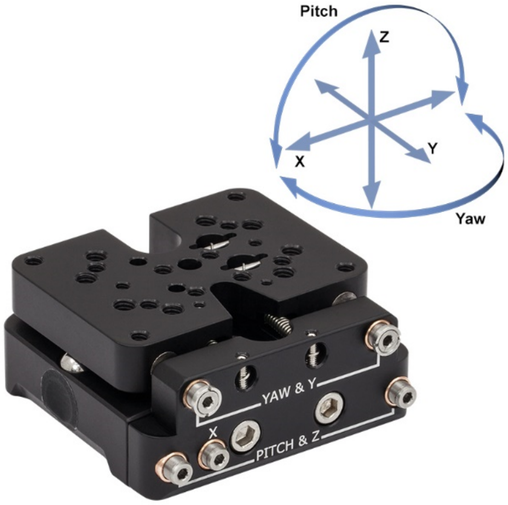

Figure 1.15: Thorlabs Compact 5 DOF Stage [13]

Due to shared sets of screws, the yaw and pitch motions are coupled with the Y and Z translations, respectively. As such, the stage can be moderately unintuitive to align since an operator must be cognizant that single translations may cause a misalignment with its paired axis.

The stage is capable of actuating precise distances through 100 thread per inch screws which are further amplified by angled ramps internal to the stage itself. These ramps implement spring plungers that are compressed when the ramps are pushed forward by the screw motion. As the spring plunger is compressed, ball bearings travel along the ramp which then push against the main stage through its bottom surface. This can raise or lower stage depending on the position of the spring plunger and is depicted in Figure 1.16. This same mechanism was applied to the X-motion as well to further improve the resolution of the stage.

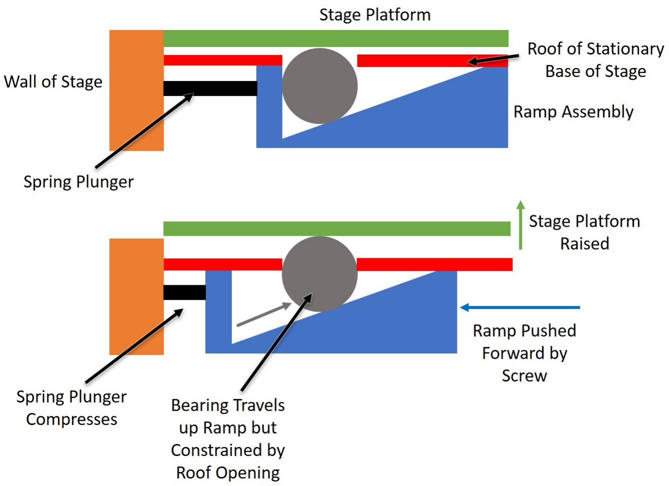

Figure 1.16: Ramp Mechanism Visual

To increase the overall range that the crystal can translate, custom coarse adjustment mechanisms were implemented in addition to the existing stage illustrated in Figure 1.17. Vertical shim stacks were used to increase the overall height (Z direction) of the stage (shown in green), and two custom brackets with slots allow the crystal to translate in the X and Y directions (shown in blue and orange respectively). With both adjustment mechanisms, the current system can translate 6 mm in the principle directions. The stage can rotate in the pitch and yaw axis a total of 3.5° and 5° respectively. While the stage can position the crystal rather effectively (i.e. it can achieve the required 5 μm accuracy) there are several issues present in the current system.

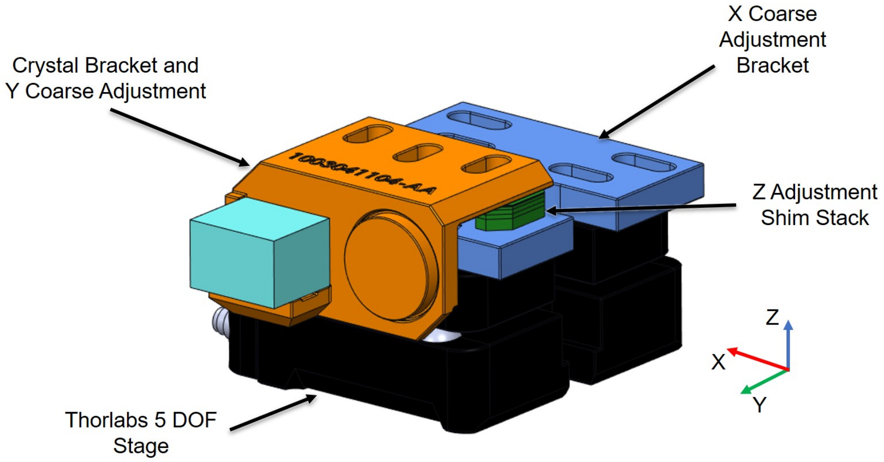

Figure 1.17: Current Full Assembly of the 5 DOF Stage

The Thorlabs stage uses restoring springs to secure the main stage in one position. Theoretically if the stage were to be displaced due to an external force, the restoring springs would return the stage to its original position to remain in contact with the actuation screws. However, the CBI team noted during an experiment if the stage were forcibly displaced the returned position could be off by an order of 10s of microns. Since the crystal is aligned offline and then transported to the target chamber, the team was concerned that the current stage may be sensitive to bump/acceleration loads in transit to the target chamber. In its current use, there have only been a few occurrences that the stage has been suspected to be moved out of alignment during transportation. Errors produced from misalignment during transportation can be extremely costly, since often they cannot be determined until after an experiment is performed. As such, one of the desired aspects for the newly designed stage would be insensitivity to bump or acceleration loads. Current users of the system noted that the Thorlabs stage suffers from issues of stiction after prolonged use. Aligning the crystals became more tedious due to stiction issues which in turn caused complications with overall system responsiveness. The new system should address these issues to help improve the operator's user experience when aligning the crystals.

1.6 Objective

The objective of this thesis is to record the design development of the 5 degrees of freedom stage for the new dual crystal backlighter imager (DCBI). Before design development began, the requirements of the range of motion for the new stages needed to be defined. A ray tracing analysis was performed to help visualize the location of different crystals that could be used in an experiment. This analysis also provided insight into potential complications that would be introduced with transitioning to a dual crystal setup. In addition, some of the existing hardware would need to be modified to accommodate for a dual crystal setup. A preliminary dynamic analysis was performed to determine if minor modifications could be made to the existing hardware to survive the unique loading case specific to experiments performed at the NIF. Throughout the design development, background research was performed to investigate and learn techniques used to actuate optomechanical stages in a precise manner. Common industry techniques as well as methods used in academic settings were investigated. Finally, a proposed design solution is presented that meets the requirements set. Further work and conclusions are discussed to ensure consistent performance from the proposed solution, primarily through testing means.

Chapter 2

RAY TRACING MODEL

A ray tracing model was developed to define the required range of motion of the crystals. The purpose of this model was to track the path of the X-rays produced from the backlighter source. The X-rays would pass through the target onto the crystal, where the X-rays reflect off the crystal onto the detector. A simplified representation of the key components and layout of the ray tracing model are shown in Figure 2.1.

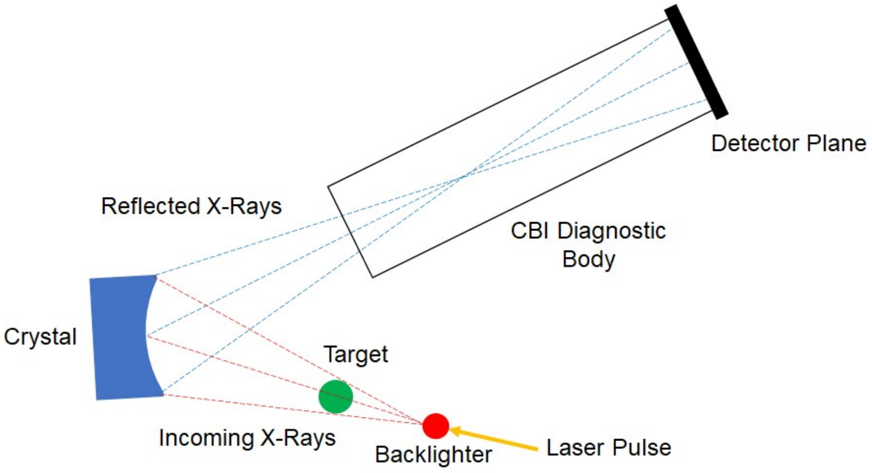

Figure 2.1: Simplified Representation of Key Components in the Ray Tracing Model

2.1 Model Setup

The models presented earlier in Chapter 1 were all developed with one crystal. The purpose of the ray tracing study was to have a reliable model on the X-rays path for a dual crystal system. Several changes needed to be made on the original CBI system to allow for a dual crystal setup. Illustrated in Figure 2.2, two backlighters would be vertically offset from the target. Each backlighter would be targeted to one of the two crystals that are offset vertically from one another within the housing.

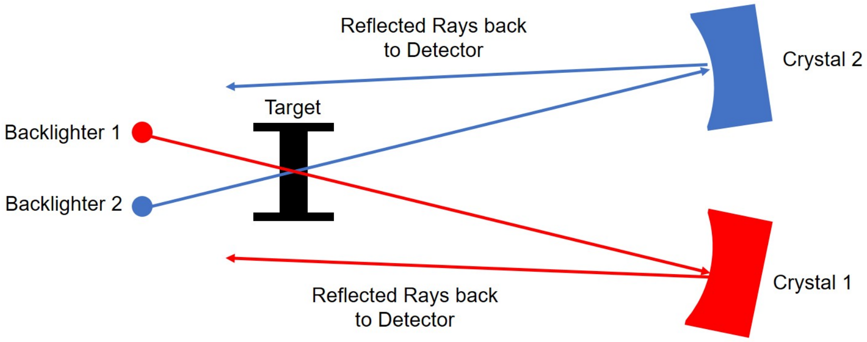

Figure 2.2: Simplified Representation of a Dual Crystal Setup

Using CAD software, such as Creo Parametric, distance constraints could be maintained between components while also having enough versatility to investigate relations between the X-rays to the components in the same model. Besides defining the range of motion of the stage, the model revealed potential issues that could be generated as a result of a dual crystal system. These potential issues focused on the sizing of the target window and the clearance between the reflected X-rays and the hohlraum. The reflected rays would need to be sufficiently far away from the target to prevent the X-rays from being blocked by the target itself. As part of the target design, there are dimpled shields on the top and bottom of the hohlraum, shown in Figure 2.3. These dimpled shields are implemented to shield the hohlraum from unconverted laser light whilst simultaneously protecting the laser against dangerous reflections from the target.

Figure 2.3: Dimpled Shields on Upper and Lower Surfaces of the Hohlraum [14]

Depending on the crystal Bragg angle and chosen detector, the reflected X-rays could potentially interfere with the dimpled shields on the target. Figure 2.4 provides an example of a potential reflected X-ray interfering with the target if higher Bragg angles are used.

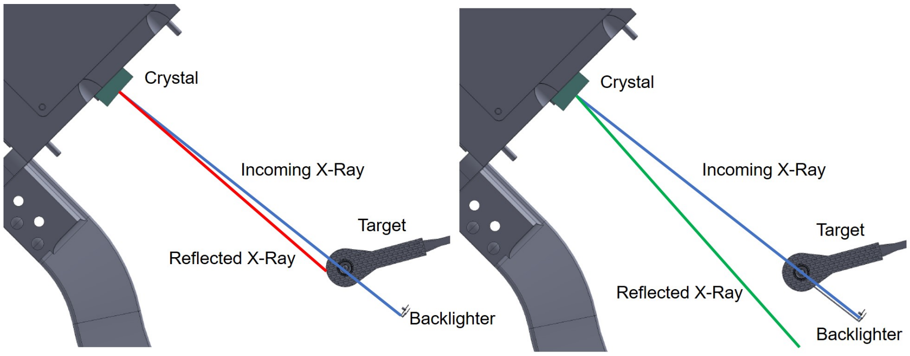

Figure 2.4: Target Interference with Higher Bragg Angle (Left), Clearance with Target with Reflected X-Ray (Right)

The dimpled shields on the target may be modified depending on how close the reflected X-rays pass by the target. One of the outcomes of the ray trace model was to learn about the limitations on particular crystal configurations from a target interference perspective.

To allow for X-rays to pass through the fuel capsule and produce a radiograph of the implosion, windows need to be created in the hohlraum as shown in Figure 2.5.

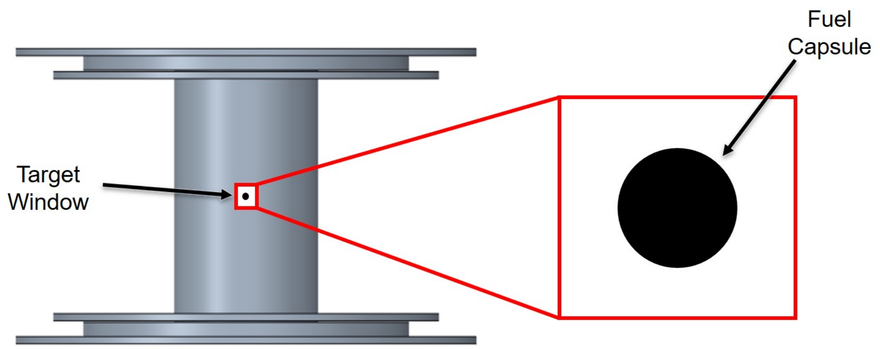

Figure 2.5: Target Windows Implemented in the Hohlraum

Generally, the target windows are sized to be 0.8 by 0.8 mm. For a single line of sight, i.e. CBI with 1 crystal, a square window produces square images. However, when two lines of sight pass through the windows at different angles, i.e. CBI with 2 crystals, the window size would need to be modified to accommodate for the differing crystal positions. In the standard CBI setup, the backlighter is positioned on the same horizontal plane as the center of the target. The maximum field of view (FOV) for the radiograph is defined by the exit edges of the target window, producing an FOV close to the same size as the window. However, for the dual crystal setup, two backlighters will be positioned above and below the horizontal plane of the target (since each crystal needs a specific backlighter). By doing this, the FOV becomes reduced because the top entrance edge becomes a clip point. In Figure 2.6 the two setups are described showing the reduction in overall FOV with the dual crystal setup. The setup on the left represents a setup with the backlighter, target and crystal all on the same horizontal plane. The setup on the right shows one crystal and backlighter for a 2-crystal setup.

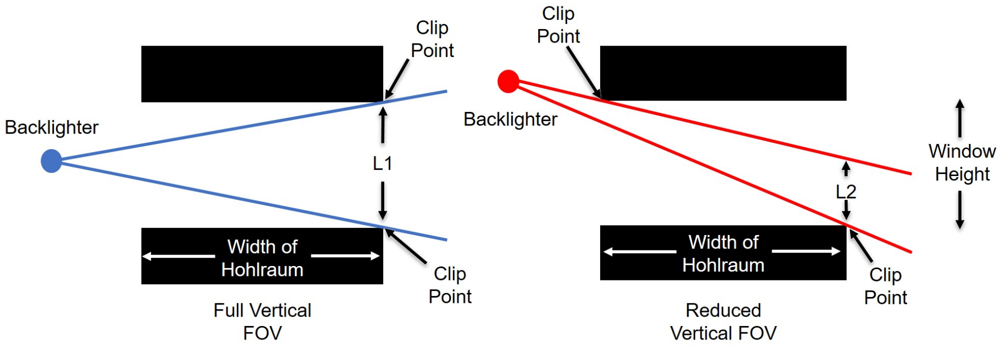

Figure 2.6: Difference in FOV based on Backlighter position

To maintain a sufficient vertical FOV, the target window would need to be modified. If the target windows were taller this would allow for the vertical FOV to increase. Figure 2.7 provides an example of the vertical FOV increasing due to increasing the target window height.

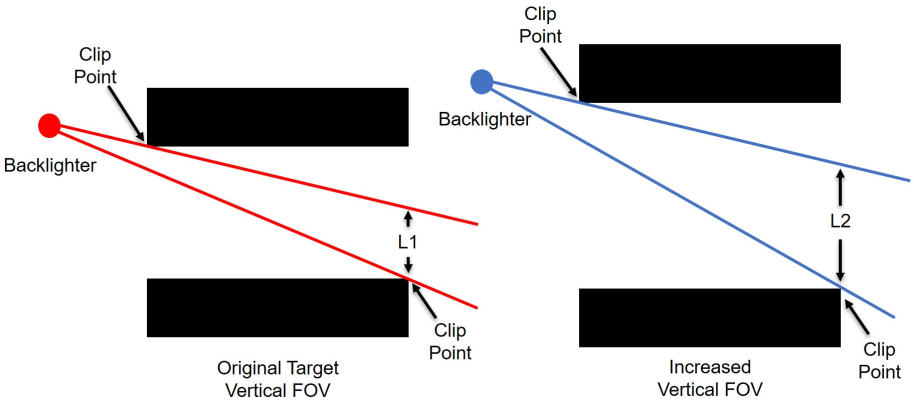

Figure 2.7: Vertical FOV differences based on Target Window Height

Due to the implementation of two crystals, the window would need to be slightly modified to allow for both images to have a sufficiently sized FOV. The reduction in FOV is inherently caused by the system setup, due to parallax with both crystals being vertically offset from the center plane of the target. The requirement for the minimum field of view is 0.6 by 0.6 mm centered on the capsule at target chamber center (physicists want to be able to have a full view of the capsule up to radii of

300 μm). The windows are limited in size since energy losses from the hohlraum are directly proportional to the overall window area. It was desired to maintain the same window area as the previously used 0.8 by 0.8 mm windows. As a result, the window area was considered to be fixed, but the dimensions for the length and height were varied to determine what change was necessary to match the 0.6 by 0.6 mm FOV requirement.

For experiments at the NIF, different detectors can be utilized depending on the desired outcomes of the experiment. The Single Line of Sight camera (SLOS), Hardened Gated X-Ray Detector (HGXD), and the hardened Single Line of Sight camera (hSLOS) are the detectors used to capture radiographs. Each of these detectors have sensitive locations where the X-rays need to land to capture a radiograph. Figure 2.8 shows the different sensitive regions for each detector.

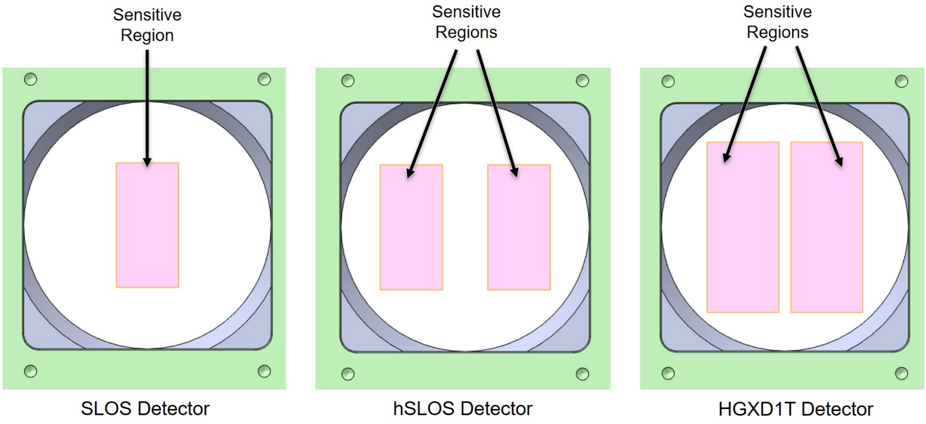

Figure 2.8: Detector Sensitive Regions as Viewed through CBI

Each of these detectors have different capabilities, with their own advantages and disadvantages. For different physics experiments, each detector could potentially be used depending on the need. So, it is important that the X-ray paths for each detector are considered to ensure that the 2-crystal CBI design can accommodate all of them.

2.2 Model Cases

To analyze these two conditions, three different cases were considered based on feedback from stakeholders at the NIF. These three cases were described as:

1. Using the same Bragg Angle for both the top and bottom crystal, find the window size that allows a minimum FOV of 0.6 by 0.6 mm at the target. This must be assessed for 3 different detectors (hSLOS, SLOS, and HGXD). Find the distance of the closest reflected ray to the dimpled shields for Bragg angles of 88° and 87.53°.

2. Allow for the 2nd crystal to vary in Bragg angle by 1° and 2° from the original Bragg angles analyzed in case 1. Find the required window size for the 0.6 by 0.6 mm FOV and closest reflected ray to the dimpled shields.

3. For the hSLOS detector and two crystals with the same Bragg angle of 88°, find the window size and target clearance based on a staggered or aligned image configuration.

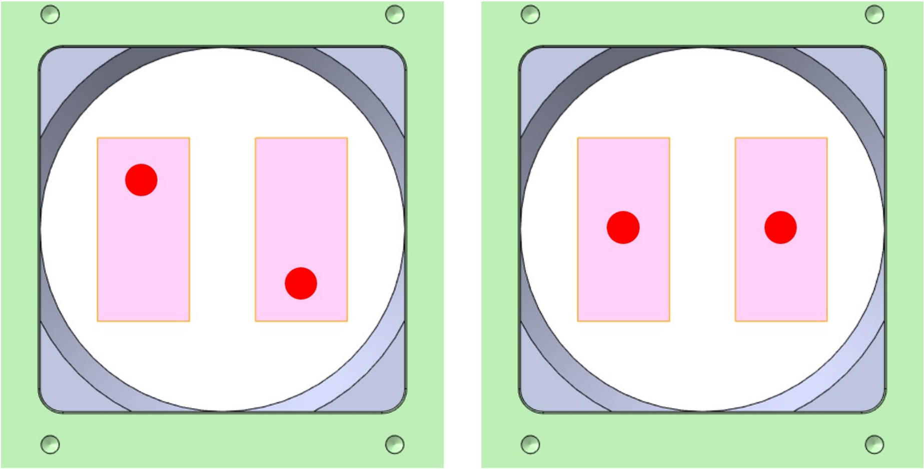

Figure 2.9: Staggered (Left) vs Aligned (Right) Radiograph Configurations for hSLOS

With these cases, the ray trace model would cover the typical ranges and applications that the dual crystal CBI may encounter.

2.3 Assumptions

For developing the model there were assumptions that were implemented to maintain consistency between all three cases:

1. The center of the crystals would remain 7 mm above and below the equatorial plane to allow for a 2 mm separation between the closest edges of each crystal.

The equatorial plane is defined as the level horizontal plane that intersects the center of the target chamber. In the standard CBI setup, the crystal is typically located on the equatorial plane. However, with the modified system of 2 crystals, each crystal is separated vertically to prevent any interference between the crystals regardless of required Bragg angle. In contrast, if the crystals were positioned horizontally next to each other, similar Bragg angles could not be used due to overlapping positions. In the future, if the crystals were slightly smaller, the crystals could be positioned closer together which would reduce issues with parallax and increase the vertical FOV.

2. The Bragg angles would be constrained from a range of 85.5° to 88°.

These angles were deliberately chosen to accurately represent the current crystals being used or considered for CBI. As of now, the highest Bragg angle used in experiments is 87.53° to satisfy the Bragg relation and match the commonly used backlighters for experiments. However, in the future higher Bragg angle crystals may be considered for use. As part of the ray tracing model and investigated in the outlined cases, the main concern is with clearance between the reflected rays and the target (specifically the shields) for high Bragg angle crystals.

3. The distance between TCC and the center of each crystal is fixed at 137.5 mm.

This is necessary for CBI to maintain its current 10x magnification. With the standard CBI setup, a FOV centered about TCC of 0.8 by 0.8 mm would produce a radiograph image that is 8 by 8 mm in size.

2.4 Creating the Model

To develop the ray tracing model, three points in space were defined for each given Bragg angle. These points include, TCC, the center of the front surface of the crystal, and one of the detector sensitive areas. To locate the center points of the crystal, two separate planes were created 7 mm above and below the equatorial plane. From this plane, the fixed distance of 137.5 mm from TCC and the crystal centers could be defined to ensure a 10x magnification was achieved.

The ingoing ray was defined fully by the TCC and the crystal center location. The outgoing ray was defined by the crystal center to the detector area. With these rays, a plane could be defined which contains the full path of the center X-rays from the backlighter to the detector. The Bragg angle is measured as the angle between the reflected ray and the line perpendicular to the midpoint between the incoming and reflected rays. An example Bragg angle measurement is shown in Figure 2.10. For each angle of interest this process was repeated to track the center rays for each crystal Bragg angle and detector areas.

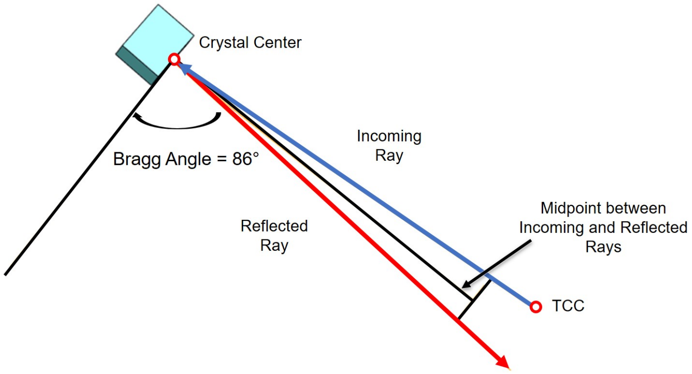

Figure 2.10: Example Bragg Angle Measurement

This process was repeated to define the points necessary for the three test cases. Once all the points were defined, it was then possible to define the volume of X-rays that originate from the backlighters. For both the bottom and top backlighters, the volume of X-rays were defined by the clip points on the target window. Regardless of the chosen Bragg angles, both the top and bottom backlighters would have clip points on the front and rear edges of the windows. Examples of these clip points are shown in Figure 2.11.

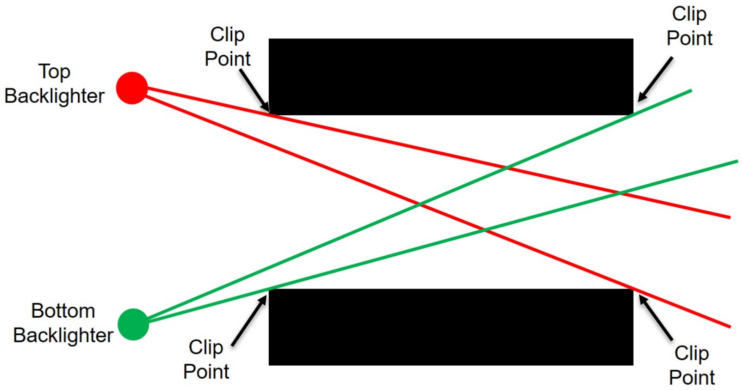

Figure 2.11: Vertical Clip Points for the Top and Bottom Backlighter on the Target Window

If similar Bragg angle crystals were chosen, the horizontal clip points would be determined by the exit edges of the window. However, if dissimilar crystal Bragg angles were used, the backlighters would also be skewed horizontally relative to the target. A similar principle was applied to define the horizontal volume of rays, with the front and exit edges of the windows defining the clip points.

Measurements were taken at TCC to measure the produced FOV based on the clip points of the target window. Depending on the measured FOV, the window size would be modified until the required 0.6 by 0.6 mm FOV centered on TCC measurement was met. With the defined clip points, the volume of X-rays could be fully represented in the model as shown in Figure 2.12. The rays shown in Figure 2.12 represent the path of the full volume of X-rays that are produced from the backlighter, pass through the target and windows, reflect from the crystals, and eventually end up on the detector.

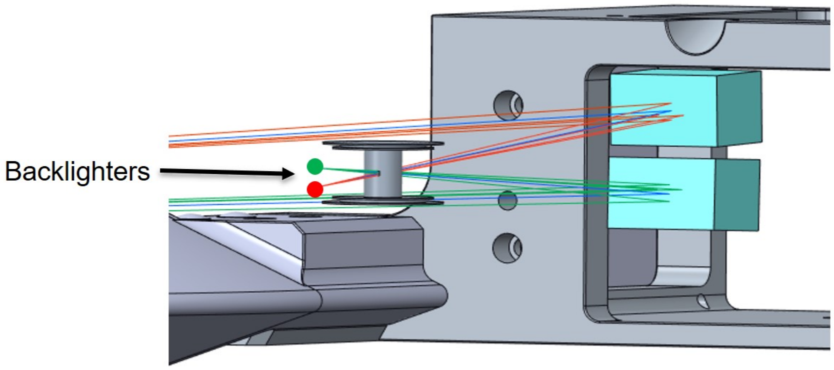

Figure 2.12: Volume of X-rays for Both Crystals

With the volume of X-rays defined, the distance from reflected rays to the target could be measured to determine if interference would occur for different Bragg angles and detector configurations.

After analyzing each of the desired cases, a window size was found that provides a minimum 0.6 by 0.6 mm FOV (centered at TCC) for crystals with similar Bragg angles, while simultaneously maintaining the same area as the standard 0.8 by 0.8 mm windows. Such a window is required to be 0.96 mm high and 0.66 mm wide. For cases with different Bragg angles between crystals, the window area would need to be increased to meet the minimum 0.6 by 0.6 mm FOV. In addition, for the 3 cases the closest reflected ray to the dimpled shields was measured from the projected cone of rays. In all 3 cases the highest Bragg angle crystal was considered. The 88° reflected rays passed too close to the target, where the reflected X-rays interfered with the hohlraum shields. Higher Bragg angle crystals like 87.5° also had the potential risk of colliding into the target shields, however the shields could be modified to mitigate this risk. A potential modification to the dimpled shields would be to cut away the section closest to the reflected ray and fold them downwards, depicted in Figure 2.13. This would allow for the same effective protection of the target while reducing the overall radius of the target in the direction closest to the reflected CBI rays. The measurements for the ray interference as well as the window modifications for the different cases can be found in Appendix A.

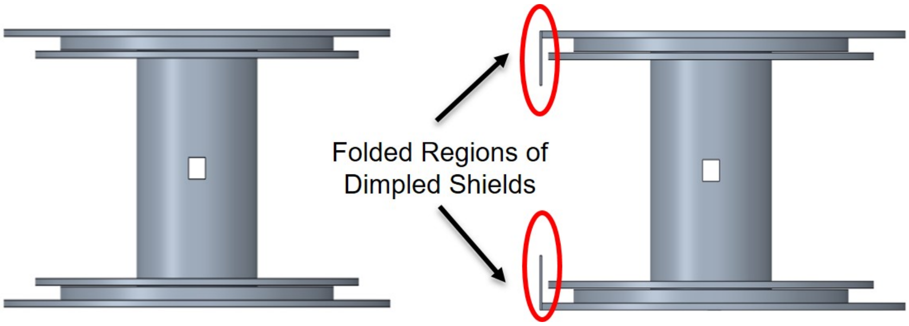

Figure 2.13: Potential Shield Modifications for High Bragg Angle Crystals

If 88° crystals were ever needed in a dual crystal system, more dramatic adjustments to the target shields would have to be undertaken. These adjustments would not be impossible, but with this knowledge physicists at the NIF can be notified beforehand if they desire to use high angle crystals for future experiments.

Another important result from this modeling was that it provides the required range of motion of the crystals. Based on certain combinations of Bragg angles and detectors, the right sided limit (relative to facing the front of the housing) was a high Bragg angle of 88° pointed at the left strip of hSLOS. The left sided limit was a low Bragg angle of 85.5° pointed at the right strip of hSLOS. Both of these limit cases are depicted in Figure 2.14. These two cases define a requirement that the new crystal mounting system must be capable of at least 18 mm of horizontal translation.

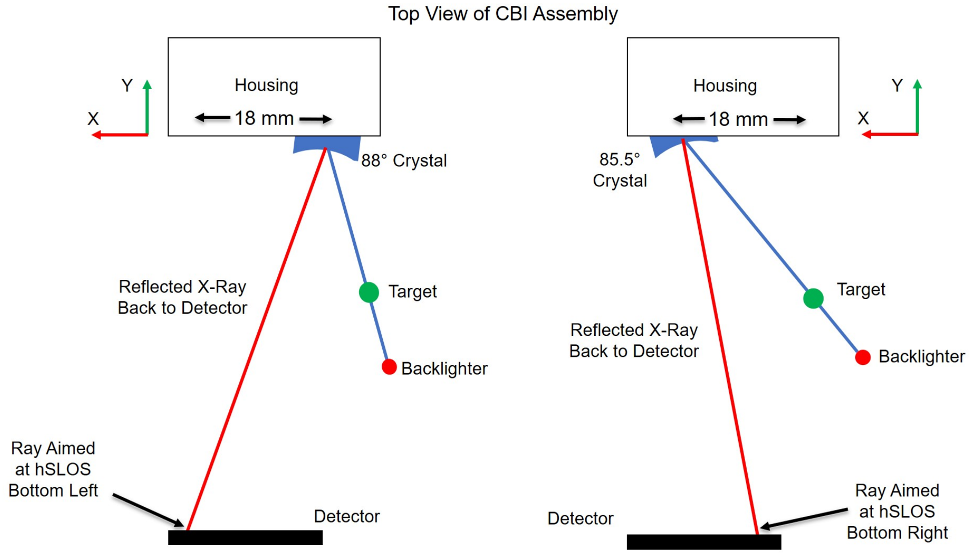

Figure 2.14: Horizontal Range of Motion Defined Limits

This combination of Bragg angles and detectors also provided the range limits for the depth of insertion of the crystals. Moving from a high Bragg angle to a lower Bragg angle generally follows an arc centered around TCC. For the chosen Bragg Angles, the 88° crystal had the lowest depth of insertion while the 85.5° crystal had the furthest depth of insertion. This defines the required range of Y-travel as 3 mm. These measurements are shown in Figure 2.15.

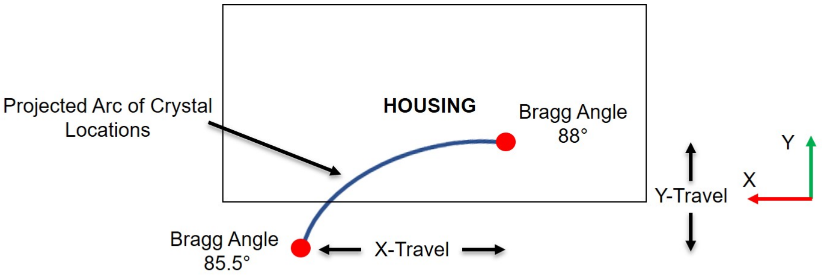

Figure 2.15: Simplified Representation of Planar Travel Limits Based on Bragg Angle

From a similar measurement, the required yaw angle range could be found as the difference in angle from TCC between the lowest and highest Bragg angles used. This resulted in a total yaw range of 7°.

The vertical distance of the crystals was set at the desired height of 7 mm above and below the equatorial plane. In the model these locations were idealized as fixed positions. To accommodate for machining tolerances, it was chosen that the vertical adjustment range of the new crystal mounts would be 2 mm. The pitch rotation was small but varied depending on the desired detector locations. The required rotation for pitch was found to be close to 2° of travel. The collection of required travel ranges are shown in Table 2.1.

Table 2.1: Defined Travel Ranges for the 5-DOF Stage

Translation or Rotation	Required Travel
X-Translation	18 mm
Y-Translation	3 mm
Z-Translation	2 mm
Pitch (X-Rotation)	2°
Yaw (Z-Rotation)	7°

These ranges define the travel requirements for the 5 DOF stage.

Chapter 3

SYSTEM REQUIREMENTS

Before design development began, the requirements that would drive the design choices for the new stage had to be defined. After the ray tracing analysis, the full range of motion of the stage was defined based on combinations of detectors and commonly used Bragg angle crystals. However, besides these basic performance requirements there were other quality-based requirements defined. In developing these requirements, two sets of requirements were defined with guidance from stakeholders at the NIF. Hard and soft requirements were used to define the design space the final design would need to encapsulate. Hard requirements were defining factors that were necessary to achieve to ensure the success of the design. Soft requirements were defined as ideal aspects that would be overall beneficial to the system but were not required for the system to perform its basic functions. These soft requirements could be omitted or modified throughout the project with sufficient evidence that they could not be satisfied.

3.1 Hard Requirements

The base requirements that the 5 DOF stage must achieve are listed below:

1. The stage must be capable of 5 degrees of freedom, XYZ translation and pitch and yaw rotation.

Due to using a spherically bent crystal, the crystal is insensitive to roll in terms of alignment. As such, all other degrees of freedom need to be adjustable to properly position the crystal.

2. The newly designed stage must be capable of translating to positions for commonly deployed crystals.

The range of travel limits were found through the ray tracing analysis which considered commonly used Bragg angle crystals. The defined axis of motion for the crystals as well as the defined range of motion are presented in Figure 3.1 (the rotations are not shown but are assumed to follow the right-hand rule). The current crystals deployed have Bragg angles that range from 85-87.5°. It was desired for the newly designed stage to accommodate for the current deployed crystal angles in addition to other crystal angles that may be used in future experiments. Based on the ray tracing model, the dimension that would vary the most would be the X-translation movement based on the addition of crystals outside the typical range. As such, the range of travel for the X-translation was increased.

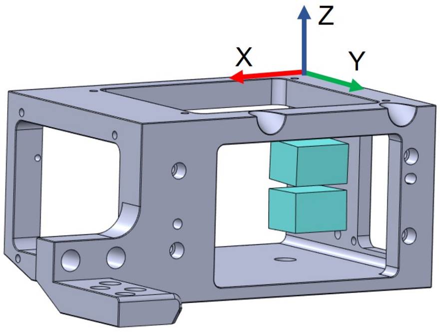

Translation or Rotation	Required Travel
X-Translation	22 mm
Y-Translation	3 mm
Z-Translation	2 mm
Pitch (X-Rotation)	2°
Yaw (Z-Rotation)	7°

Figure 3.1: Defined Coordinate System for the Crystals and Required Range of Travel

3. The stage must match the precision of the current system.

The current stage has a precision that was primarily driven by the 100 thread per inch screws that translate the stage. However, with the implemented ramp system the precision was improved to 146.5 μm/rev, compared to the 254 μm/rev possible with a direct drive fine pitch screw. For the rotation adjustments the precision is 2.9 mrad/rev and 6.25 mrad/rev for the pitch and yaw respectively. During the offline alignment process, the precision of 254 μm/rev was sufficient in aligning the crystals (in the X direction). The newly designed stage should be capable of matching this level of precision, but if a higher precision could be achieved (such as using a similar method as the ramp mechanism) that would be ideal. With this level of precision, the crystal alignment would be within the aiming budget necessary to ensure the X-rays land on the sensitive regions of the detectors.

4. The stage must be accessible from certain locations in the existing housing.

In the future, the CBI diagnostic is changing its offline alignment process. As part of this alignment process, a hexapod with a mounted point source microscope (PSM) will be positioned in front of the housing. To reduce the risk of injury, an operator would be unable to access the front of the housing as shown in Figure 3.2. The new stage can be accessed from any other region of the housing. However, the side, top and back should be prioritized for ease of accessibility.

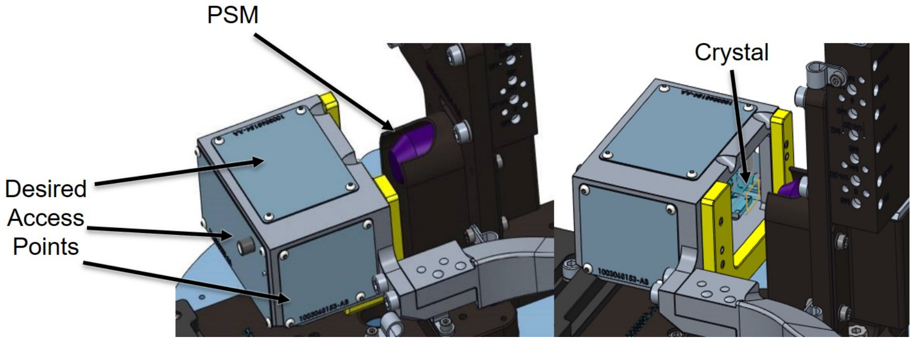

Figure 3.2: PSM Positioned in Front of Housing as part of the Alignment Process

5. The precision range of travel must be sufficient for an operator to easily align the crystal.

After the ray tracing analysis it was predicted that the adjustment system would be split into precision and coarse adjustment mechanisms (due to the large range of travel in the X direction). The coarse adjustment would first be adjusted to position the crystals a few hundred microns from the desired location. The precision adjustment mechanism would then be used to fine-tune the final crystal position. To easily interface with the system, the precision travel range should be sufficiently large to prevent constant re-alignment from a coarse adjustment system. After discussing with stakeholders at the NIF, it was decided that a range of travel for principle translations at minimum range from ± 1.5 mm and for rotations to range from ± 3°.

6. Acceleration or bump loads must not affect the alignment of the crystal.

To reduce risk of misalignment during transportation, the new stage must be able to maintain its position regardless of external disturbances. This could be achieved either through a restoring system improved upon from the current stage, or a stiff enough system that errant accelerations do not translate the system.

3.2 Soft Requirements

The soft requirements listed below would either enhance or improve upon the capabilities of the current 5 DOF stage. It was recognized that these requirements may be difficult to implement or need to be revised based on the design development.

1. The housing for the new system remains the same volume.

The current housing used has the layout and dimensions shown in Figure 3.3. The current stage occupies a majority of the housing volume, making it impossible to accommodate for a second crystal.

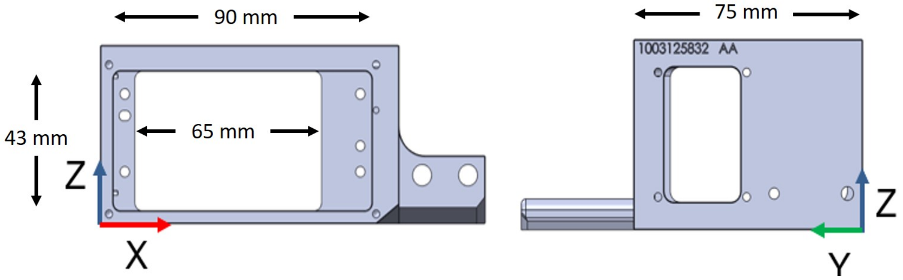

Figure 3.3: Current CBI Housing Dimensions

The CBI team recognized that this requirement would be one of the first to be modified, since most commercial solutions already encompass a large amount of the space provided. The most constraining dimension of the current housing would be the 43 mm height limit. Since the top crystal is closely located to the top surface of the housing as shown in Figure 3.4, packaging components to align the top crystal was anticipated to be the most challenging aspect.

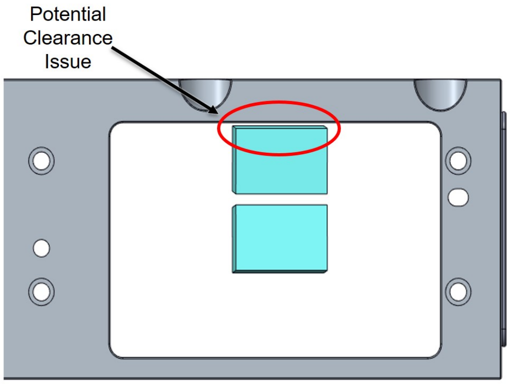

Figure 3.4: Top Crystal Clearance from Roof of Housing

If this requirement were to be met, this would prevent a redesign of interfacing components, such as the mating nose-cap. In addition, analysis performed in the past for the current CBI housing would not have to be repeated if previous hardware could be used.

2. Each crystal is adjusted independently from one another.

Allowing for both crystals to be independently adjusted would allow for operator convenience and ease of alignment. However, if two separate 5 DOF stages could not be developed to fit within the packaging, a different approach could be taken. As an example, both crystals could be mounted to the same bracket relative to one another. This way, one stage would be able to move both crystals. With the proper setup, the combined movement from the stage would still allow for both crystals to be positioned to their correct locations. This would shift the focus of developing a 5 DOF stage, to developing a method to ensure both crystals can be aligned properly. This would include a consistent process of locating both crystals relative to one another on the bracket. This approach is not preferential for the team, however, was considered if development of the stage was too difficult.

3. Each degree of freedom is completely uncoupled from one another.

One of the main faults with the previous stage was due to the coupling of the X and Z translations to the pitch and yaw rotations respectively. In the interest of smaller packaging, movements are often coupled together, however this removes some natural intuition in properly positioning the optic. For CBI, to allow for uncoupled rotations, the pitch and yaw rotation axis would need to be located on the front surface of the crystal. While uncoupled movements are not required, it would be expected to reduce the overall alignment time for both crystals.

4. Complications due to stiction should be minimized.

The newly designed stage should be robust enough that feedback from adjusting a degree of freedom should feel responsive. Removing complications due to stiction would contribute to improved control with aligning the crystals. This parameter is difficult to quantify but can be validated through repeated use and testing.

With these defined requirements the solution proposed could implement purely commercial off the shelf parts. It was expected that a custom designed solution may be necessary, due to attempting to achieve the soft requirements set. With these stated requirements design development and research could begin. These requirements served as guidelines and direction for developing new designs.

Chapter 4

DEBRIS WIND ANALYSIS

With the addition of a second crystal, stakeholders at the NIF were interested in investigating the required changes in supporting hardware for a dual crystal backlighter imager. The supporting hardware's purpose is to protect the crystals and components inside the housing. One of the load cases that would put these components at risk is unique to ICF experiments. This load case is referred to as debris wind and is produced from the implosion of the target. During ICF experiments, the target and components surrounding it do not become completely vaporized during the implosion. A large pressure-like wave propagates from the target and launches debris in approximately a 1-meter radius. The debris and pressure wave generated from these experiments can cause damage to the nearby diagnostics. Generally, two separate analyses are performed to model the components at risk. Predictive models have been created to anticipate where the un-vaporized material may be launched during an experiment and separate dynamic models are used for the pressure wave loading on components close to the target. For this analysis, the CBI team was concerned with finding the stresses and strains of at-risk components due to the produced pressure wave. The timescale for a debris wind load case is less than a second, with rapid changes in stress on the microsecond scale. One of the difficult aspects of modeling debris wind loads are the inputs into generating a pressure versus time relationship. Primary inputs include, the amount of laser energy used in the experiment, the mass of the target, the proximity to the target, and how the diagnostic is mounted in the target chamber. Robust models have been created to accurately approximate a pressure versus time relationship as a function of distance from the target. The models used to predict the generated pressure waves are related to the input laser energy delivered to the target and the estimated conversion into kinetic energy. The kinetic energy is then related to the momentum and impulsive loads based on the target mass and the radial distance. Based on these models, unique pressure curves can be produced that use the given inputs (target mass, laser energy, proximity to the target and mounting schemes), and can be applied to any surface exposed to the target. These pressure curves were validated through experimental data by analyzing the final deflections of collimators and filters used in experiments [15]. To implement these load curves, a dynamic analysis using a finite element model was used to observe the stress developed in components that are close to the target.

4.1 Model Creation

For CBI, there are several components that are exposed to the target during an experiment. These components include the stainless steel nose-cap, tantalum cover, polycarbonate shield, and a stainless steel retaining cover. The bolted retaining cover helps maintain the position of the tantalum, and polycarbonate shield assembly. For the debris wind analysis, the model was simplified to only include components that were necessary for stress analysis. The pins and bolts that secured the assembly were not included since they could be represented as boundary conditions. As part of a more conservative analysis a few geometric features were removed, such as rounds and small chamfers, to simplify the model. The model used for the debris wind analysis is shown in Figure 4.1. Shown in the cross-sectional view as the red and orange parts respectively, the number of polycarbonate and tantalum components were doubled to cover each separate window.

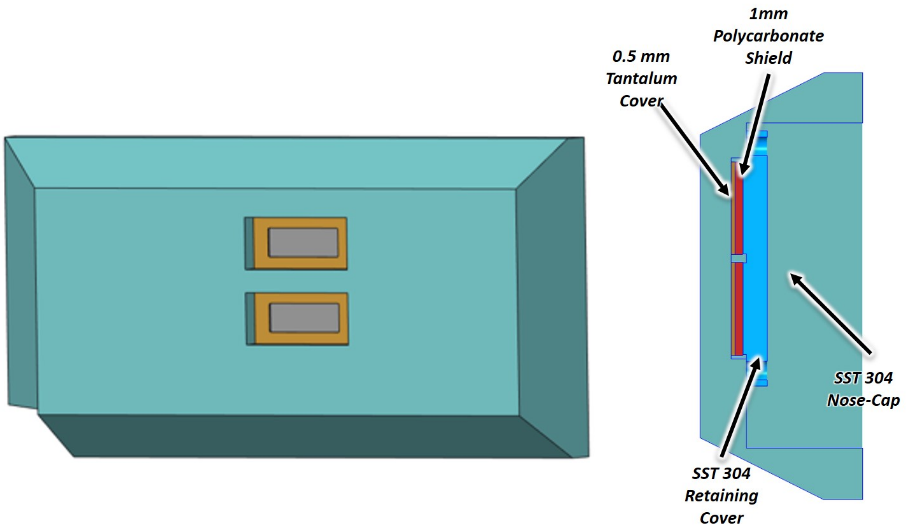

Figure 4.1: Simplified Model and Cross Section of Components

There were primarily two main goals that were to be investigated with the debris wind analysis. The first was to determine if simple changes to the original nose-cap and retaining cover would fail under the highest loading conditions. Depending on the stresses developed, a more thorough re-design may be required for the current laser energy levels tested at the NIF (1.0-2.1 MJ laser energy levels). The second goal was to determine the required sizing of the polycarbonate shields for higher energy level experiments. The main purpose of the polycarbonate shields is to ensure that stray shrapnel does not make its way into the housing and damage the crystals. However, the polycarbonate shields absorb some of the X-rays emitted from the backlighter during the shot. This reduces the amount of X-rays that can be processed by the detectors to produce the desired radiographs. The amount of energy absorbed by the polycarbonate shields are proportional to the thickness and the energy of the X-rays passing through. In fact, the polycarbonate shields will absorb a higher percentage of total energy for low energy X-rays. For the higher laser energy load cases, it was desired to find the minimum polycarbonate shield thickness required to prevent catastrophic failure. Analyses were performed at the highest laser energy level (2.1 MJ) and largest target mass (1 gram) to observe the stress and strain developed in the polycarbonate shields with varying thicknesses. The desired outcomes of this analysis were not to necessarily propose the complete design solution for the supporting hardware for CBI. However, it was to provide initial data to stakeholders on areas of concern that would require redesign of the existing components.

The primary change to the nose-cap was the addition of a second window which can be seen in Figure 4.2. Due to the crystals being placed above one another, this would cause a thin member to separate the two windows. Two separate windows are preferred to hold the tantalum cover and polycarbonate shields in place and to minimize the amount of exposed area for the internal components. However, there was concern that the separating material would be an early point of failure on the new nose-cap. When analyzing the results, the separating center bar was one of the primary locations checked for failure.

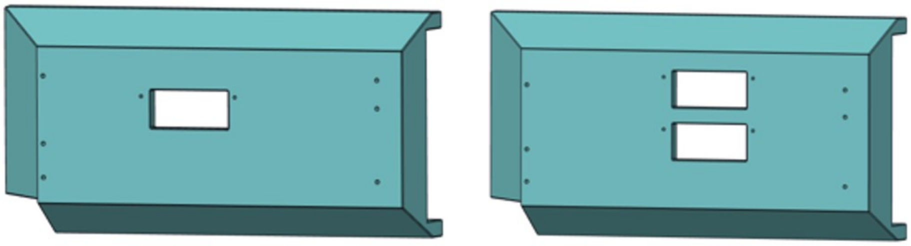

Figure 4.2: Original CBI Nose-cap (Left) and the Modified DCBI Nose-cap (Right)

In the original assembly, the only other component that would need to be modified to accommodate for a second crystal is the retaining cover. The retaining cover was expanded in size and the amount of bolt holes was increased to strengthen the retaining force of the entire assembly as shown in Figure 4.3. The rounds and chamfers on the retaining cover were removed to simplify the model.

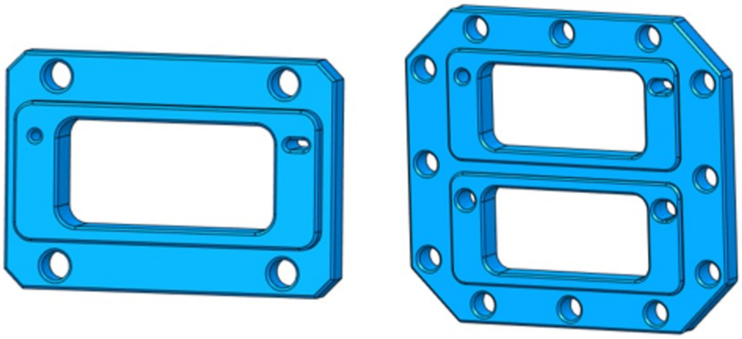

Figure 4.3: Original Retaining Cover (Left) and Modified Version (Right)

Once the simplified models were created, the entire assembly was passed into a mesh creation software, known as Cubit. Cubit is used primarily to generate meshes for components to be later used by analysis programs such as LS-PrePost or ANSYS. For parts that are uniform through their thickness, it is possible to generate hexahedral meshes from Cubit. However, for non-uniform parts, Cubit is only capable of generating a tetrahedral mesh, that could be later converted to a hexahedral mesh. Hexahedral meshes are preferred due to reducing the overall simulation time in finite-element models. Solid element meshes were used on all components, since it was desired to know the stresses developed through the thickness. The polycarbonate shields, tantalum cover, and retaining cover were able to generate hexahedral meshes due to being uniform parts across their thickness. However, a tetrahedral mesh was created for the nose-cap due to its complex geometry.

To optimize the overall simulation time, the minimum number of elements were generated to accurately represent the behavior of the assembly. For debris wind analysis, common practice was to allow for 6 elements across the thickness of parts, shown in Figure 4.4 across the nose-cap center bar.

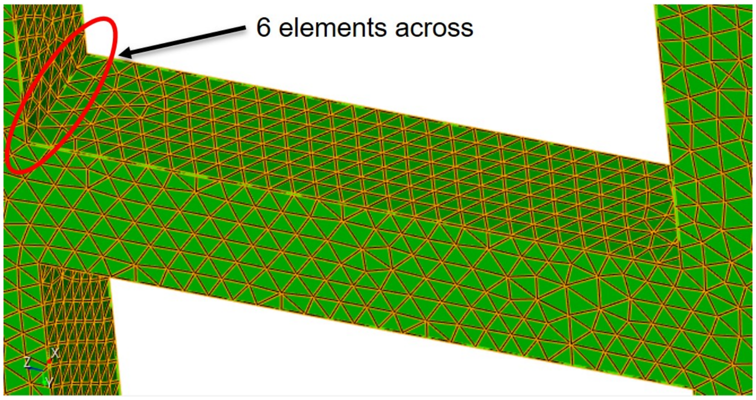

Figure 4.4: Example of 6 Elements Across Center Bar on the Nose-Cap

To evaluate if the mesh generated was ready for analysis, Cubit has quality metrics that could be used to find more information about the produced meshes. Quality metrics such as the Jacobian and aspect ratio can help determine if a uniform mesh was produced or if irregularities are present in specific regions of the mesh. The list of quality metrics used is shown in Figure 4.5.

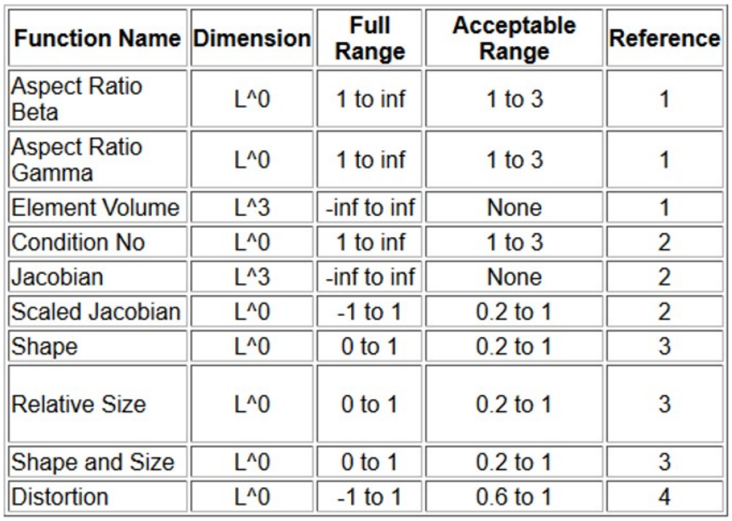

Function Name	Dimension	Full Range	Acceptable Range	Reference
Aspect Ratio Beta	L^0	1 to inf	1 to 3	1
Aspect Ratio Gamma	L^0	1 to inf	1 to 3	1
Element Volume	L^3	-inf to inf	None	1
Condition No	L^0	1 to inf	1 to 3	2
Jacobian	L^3	-inf to inf	None	2
Scaled Jacobian	L^0	-1 to 1	0.2 to 1	2
Shape	L^0	0 to 1	0.2 to 1	3
Relative Size	L^0	0 to 1	0.2 to 1	3
Shape and Size	L^0	0 to 1	0.2 to 1	3
Distortion	L^0	-1 to 1	0.6 to 1	4

Figure 4.5: Quality Metrics List for Tetrahedral Elements [16]

The output from the quality metrics test produces a gradient of colors representing the elements value when assessed against a chosen function. If any of the parts fell outside of the provided criteria, the mesh was refined and iterated until the quality metric parameters were met. An example of an approved mesh of the nose-cap is depicted in Figure 4.6. All of the elements fall within the acceptable range for the scaled Jacobian quality metric.

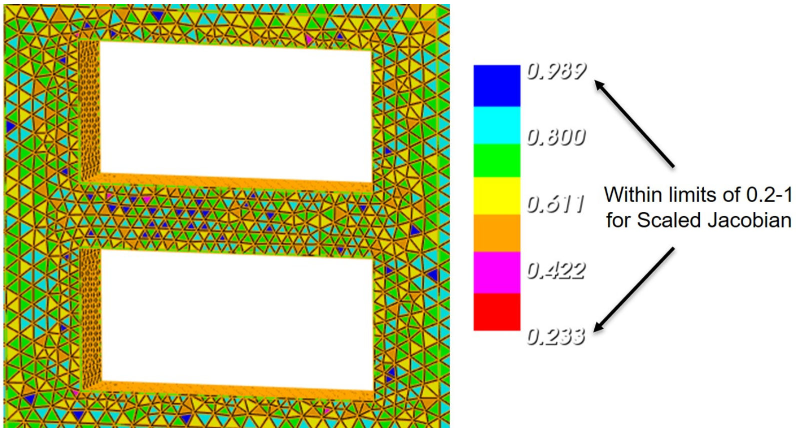

Figure 4.6: Example Mesh Evaluated with Scaled Jacobian Metric

Once the initial meshes were generated, the assembly was exported into LS-PrePost. LS-PrePost would allow for the desired simulation parameters to be defined and imparted on the model. The next few sections outline the general process for preparing the model for the debris wind analysis. Most of the setup between the models was kept consistent, such as the material assignment and boundary conditions. The primary variance between models was the applied pressure vs time curve.

4.1.1 Boundary Conditions

On the back of the nose-cap there are several bolted connections to bind the nose-cap to the housing. To model these boundary conditions, nodes on the backside of the boundary condition were constrained to have no translation. This region matched the same area where the bolted connections were in the original model. Illustrated in Figure 4.7, the region highlighted in red represents the nodes selected to represent the bolted boundary condition on the back of the nose-cap.

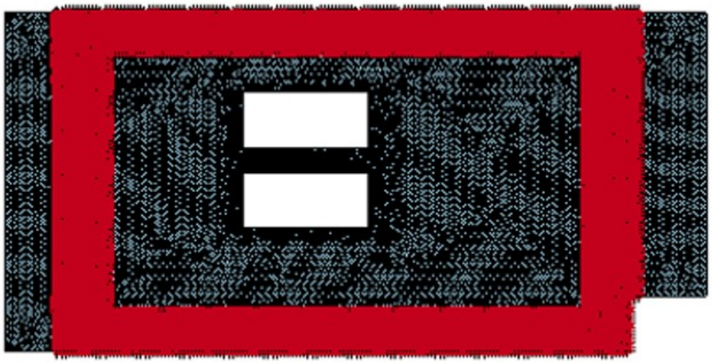

Figure 4.7: Boundary Condition Region on Back Surface of Nose-Cap

In addition to the boundary conditions to the housing, the bolt connections for the retaining cover and nose-cap were defined. This was modeled as a tied connection where the mating surfaces of the nose-cap and retaining cover were modeled as the compressive force of the bolts. A minimum of 2-3 elements were defined around the bolt holes of the retaining cover as shown in Figure 4.8. These elements were between the mating surface of the retaining cover and the nose-cap to model the bolted connections.

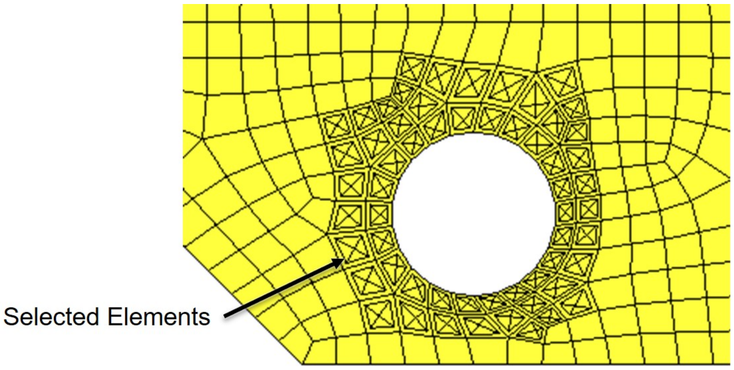

Figure 4.8: Example of Elements to Model Bolted Connection on the Retaining Cover

Additional surface contacts were defined between each part in the assembly as well. “Master” and “slave” contacts between parts were defined to allow for the appropriate interactions between each of the components. The "slave" contact displacements would be dependent on the "master" contact displacements. This helped ensure proper modeling of the load transmission throughout the assembly without adding artificial stiffness.

4.1.2 Applied Load

Regions that were exposed to the target had specific load curves applied that were a function of the distance away from the target. For most surfaces that were in direct line of sight, these load curves were applied to the elements that were exposed rather than the entire part itself. In Figure 4.9 the exposed elements of the polycarbonate that are not blocked by the tantalum cover are selected for a specific load curve.

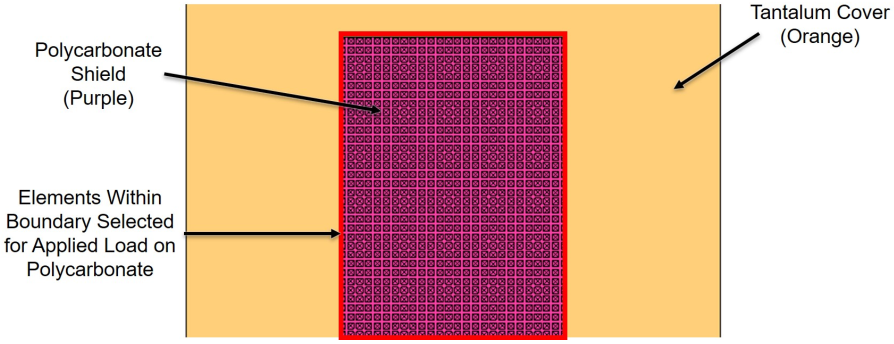

Figure 4.9: Selecting Exposed Elements to Target for Polycarbonate Shield

For angled surfaces, such as the chamfered surfaces on the nose-cap, the same load curves were applied, however a "view factor" was used that considered the angle the surfaces were at from the incoming load direction. This view factor was calculated as the cosine of the angle of the chamfered surfaces relative to the front of the nose-cap. This effectively applied a load equivalent to the projected frontal area. This was only applied to the angled surfaces of the nose-cap.

4.1.3 Failure Criteria

The remaining sections of this chapter will outline the results for the different energy levels tested. For each of the components in the model there were two primary failure criteria that were considered, the largest von-mises stress and plastic strain. This included the stress and strain developed on the surface as well as through the thickness of the parts. Stresses could be extracted early in the simulation however, plastic strain needed to be examined at the end of the simulation, to find regions that plastically deformed. The von-mises stress is being compared to the yield strength of the material which models the end of the linear region of the stress-strain relationship. In comparison, the plastic strain provides results on the non-linear relationship between stress and strain. When analyzing the results, we would only expect significant plastic strain values if the parts experience large von mises stresses above the yield strength. In Table 4.1, each component is listed with their assigned material and their respective failure limits.

Table 4.1: Failure Criteria per Each Part/Material

Part	**Material**	**Yield Strength (MPa)**	**Plastic Strain Limit (%)**
Nose-cap	SST-304	340	40
Tantalum Cover	Tantalum	770	30
Polycarbonate Shield	Polycarbonate	80	30
Retaining Cover	SST-304	340	40

To determine if the parts are considered a passable design (and used for multiple experiments), the maximum stress developed through the thickness must have a factor of safety of at least 1.5. Parts can be categorized as one-time use even if they yield through the thickness, as long as the plastic strain limit is not exceeded. Parts with high surface stress and low plastic strain may be categorized as one-time parts, due to risk of failure through repeated loading. These parts could be considered as multi-use but would need to be examined after each experiment.

4.2 Debris Wind Analysis Results

In the following sections, 4 different simulations are analyzed to assess the feasibility and need for the supporting hardware for CBI. The first two simulations were ran at 1 MJ and 1.5 MJ energy levels, which are currently used for CBI experiments. The current housing uses 1 mm thick polycarbonate to protect the internal components from the debris wind. A target mass of 1 gram was used for each simulation which is the maximum target mass used at the NIF. The remaining 2 simulations were at the highest laser energy level of 2.1 MJ. CBI has not yet been deployed for this energy level, but stakeholders at the NIF were curious if the supporting hardware could survive this loading condition. In a few previous experiments the 1 mm polycarbonate failed at 1.5 MJ therefore, at the 2.1 MJ energy level only 5 mm and 3 mm thick polycarbonate were analyzed.

Before the simulations were ran, there were areas of interest where high stress regions were expected to occur. For the nose-cap, there were three regions of interest where the component had thin members. The first was highlighted previously, as the center bar separating the two windows. The remaining regions are close to the chamfered surfaces on the nose-cap as shown in Figure 4.10. The von-mises stress results were analyzed in these regions to determine if the material yielded through the thickness.

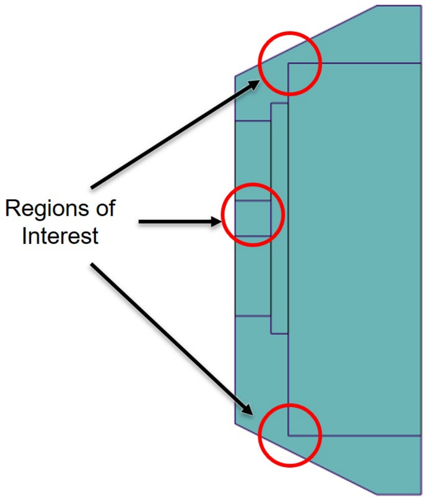

Figure 4.10: Cross Section of Nose-cap, Regions Analyzed for Yielding through the Thickness

For the first two simulations (the 1.0 and 1.5 MJ energy levels) the parts investigated were the nose-cap and the retaining cover. Since CBI has been deployed at these energy levels and has used the same hardware with regards to the polycarbonate and tantalum, it was expected that these parts would be passable. As such, the newly designed hardware would be the primary focus for the low laser energy (1.0 and 1.5 MJ) simulations. For the final two simulations, the primary focus would be analyzing the polycarbonate thickness and the nose-cap. To accommodate for different polycarbonate thicknesses, the nose-cap was modified by reducing the main cutout. By doing this, the thickness in the upper and lower sections of the nose cap had increased as shown in Figure 4.11.

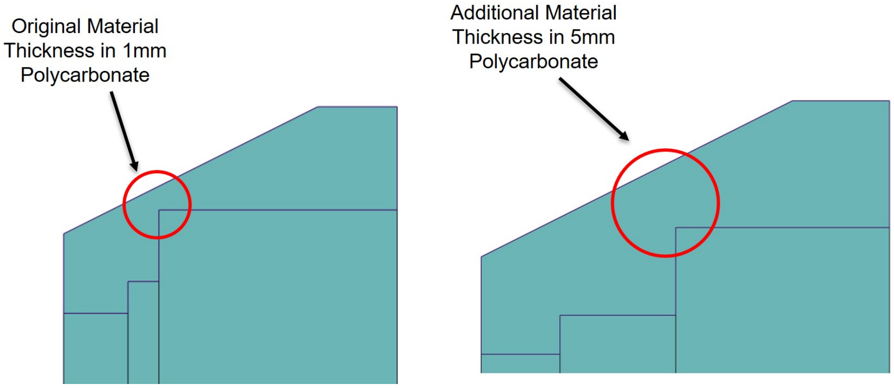

Figure 4.11: Nose-cap Changes for Thicker Polycarbonate Shields

Any parts not shown or discussed in the following sections can be found in Appendix B.

4.2.1 Laser Energy: 1.0 MJ and Target Mass 1.0 g

Starting with the nose-cap the max surface stress was found to be approximately 400 MPa near the bottom window of the housing shown in Figure 4.12. This exceeds the yield strength of the material and would be considered as a surface failure. This was expected to be a region of high stress due to the sharp corner producing a stress concentration. For the thin upper section of the nose-cap as well as the center bar, both had high stresses above or at the yield strength of 340 MPa. However, the stress did not develop completely through the thickness of the component at this energy level as shown in Figure 4.13.

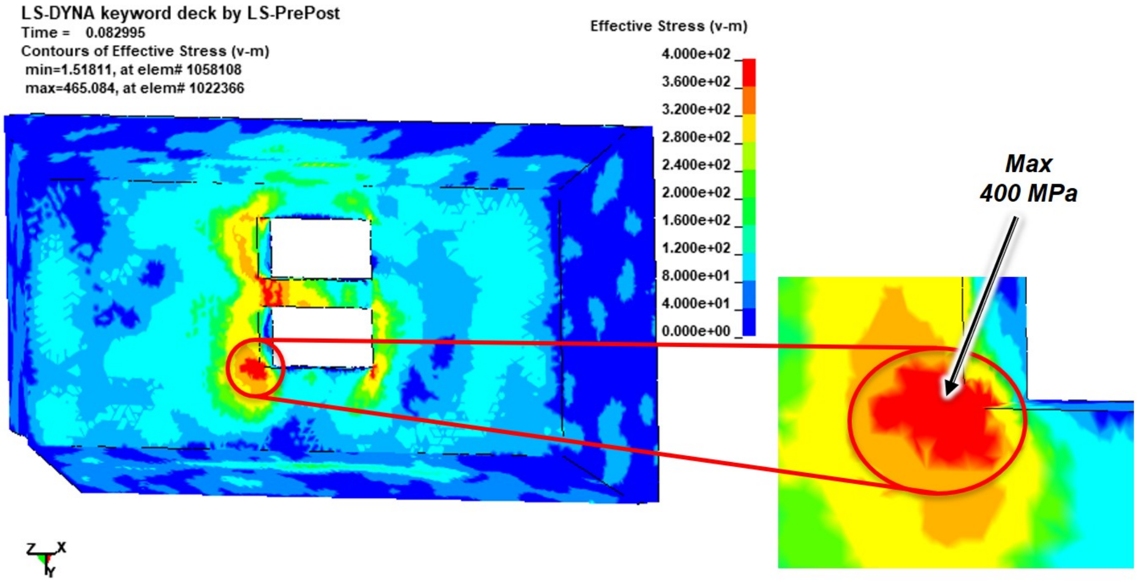

Figure 4.12: 1 MJ Nose-Cap Max Surface Stress

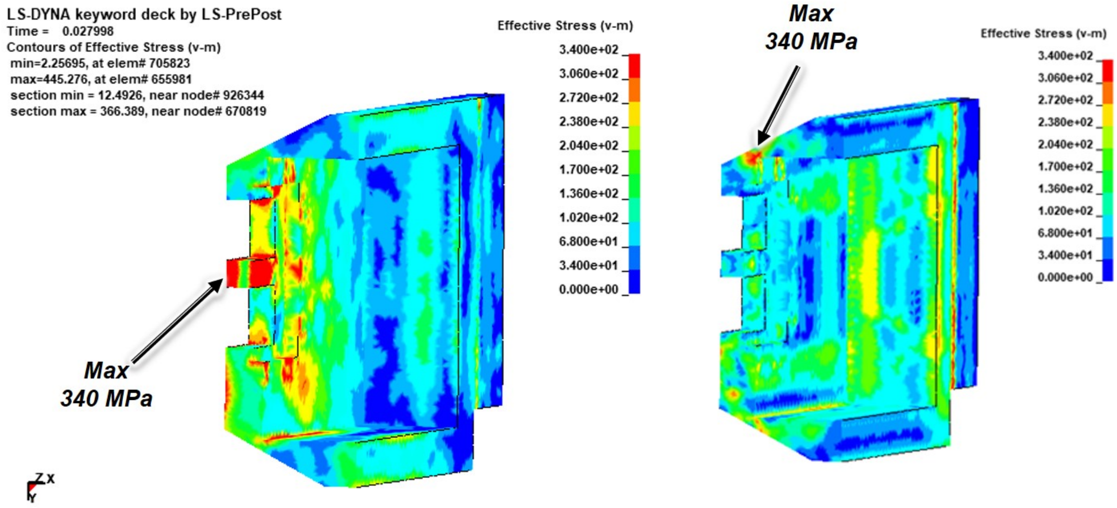

Figure 4.13: 1 MJ Nose-Cap Max Through Thickness Stress

Since most of the von-mises stress developed was near the yield strength, the plastic strain values were expected to be low. Minimal regions of plastic strain values were reported on the surface with the maximum plastic strain values found to be close to 2%. There was minimal plastic strain through the thickness of the material for the center bar or thinner sections of the nose-cap.

The tantalum covers experienced high surface stresses at the contact surface between the front face of the tantalum and the back surface of the nose-cap window. However, the material did not yield through the thickness but failed on the front surface of the cover exceeding the 770 MPa limit as shown in Figure 4.14. Even with the large surface stress developed, the tantalum covers could be used as a single use part due to not yielding through the thickness.

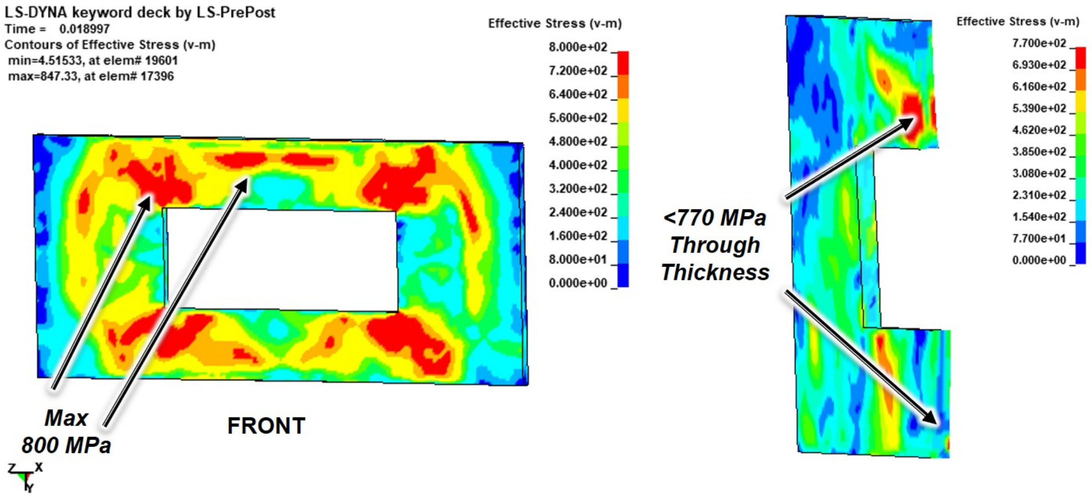

Figure 4.14: 1 MJ Tantalum Cover Max Surface and Through Thickness Stress

Due to the surface stresses, it was expected that non-zero plastic strain values would be reported on the front surface of the tantalum. In Figure 4.15, this was confirmed by the max plastic strain of 4% on the front surface of the tantalum. This is less than the 30% plastic strain limit for the material. The plastic strain did not propagate through the material as the through thickness plastic strain was less than 2%.

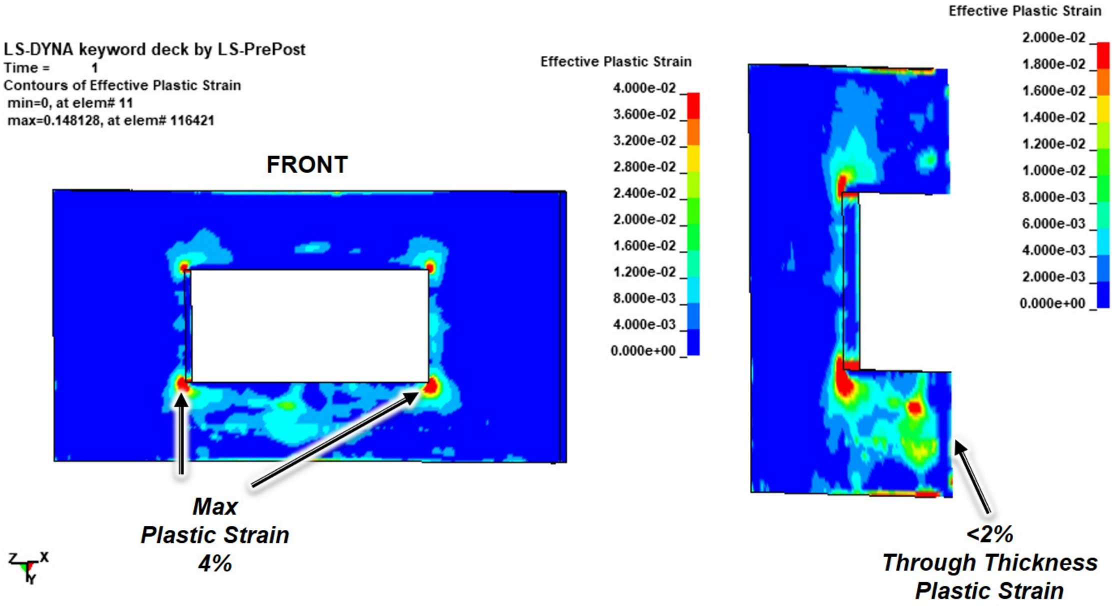

Figure 4.15: 1 MJ Tantalum Cover Max Surface and Through Thickness Plastic Strain

The polycarbonate shields experienced high stresses on the front and rear surfaces of the part. Surface stresses of 100 MPa were reported which exceed the 80 MPa yield strength for the polycarbonate. At later points during the shot, the polycarbonate shields yielded through the thickness with an average value of approximately 90 MPa as shown in Figure 4.16. The shields did not catastrophically fail, because the reported plastic strain values did not exceed the limits for the material.

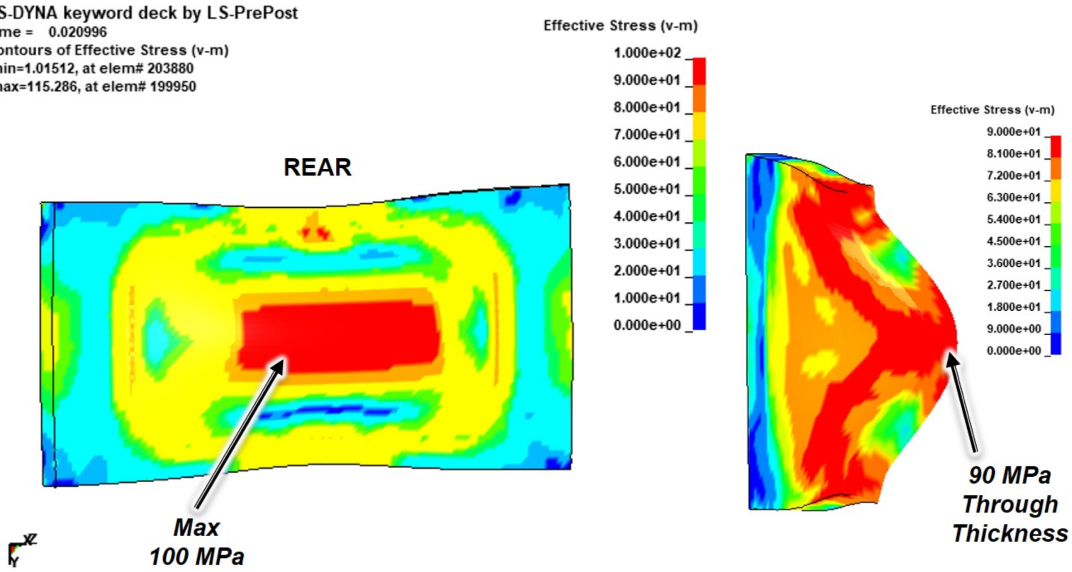

Figure 4.16: 1 MJ Polycarbonate Shield Max Surface and Through Thickness Stress

Due to the high stresses developed on the surface and through the thickness, the polycarbonate shields came close to exceeding the 30% plastic strain limit on the rear surface with surface strain values close to 25%. The large plastic strain regions occur on the rear surface of the polycarbonate shields, where the center of the shield has the greatest deflection. The polycarbonate did not fail through the thickness as an average value of close to 15% plastic strain had propagated through the material as shown in Figure 4.17.

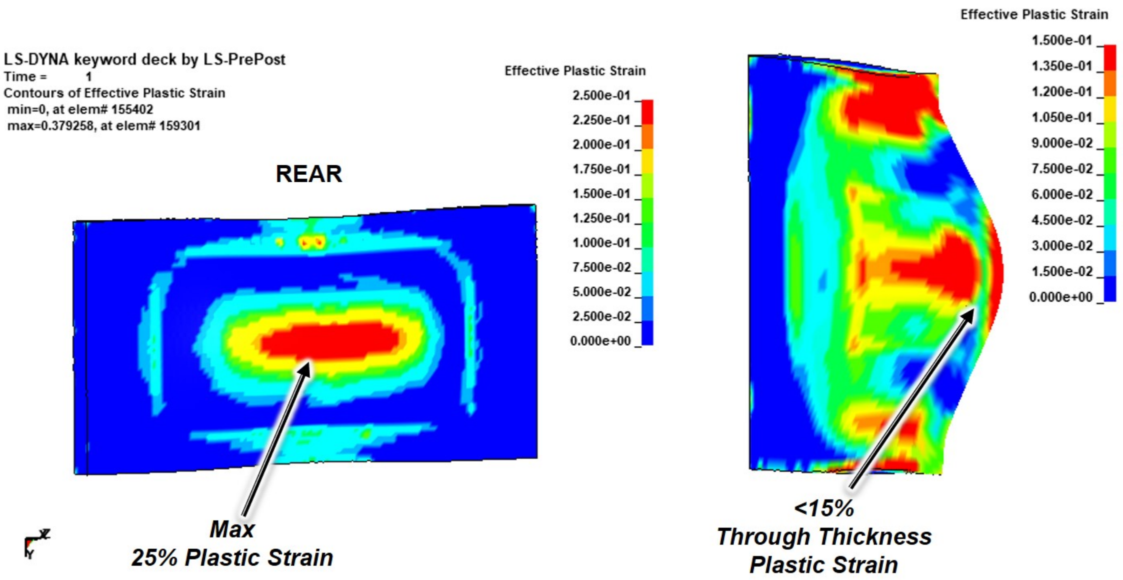

Figure 4.17: 1 MJ Polycarbonate Shield Max Surface and Through Thickness Plastic Strain

At later stages of the simulation, it was observed that the polycarbonate shields translate from their initial position as shown in Figure 4.18. This translation occurs after the primary loading from the pressure wave. The observed translation occurs close to 0.5 ms in the simulation, in comparison the load curve is only applied for the first 9 μs in the simulation. As a result, the stresses and strains produced from the load curve were representative of the expected results, since the timescale of the load applied occurs much earlier than the translations of the polycarbonate.

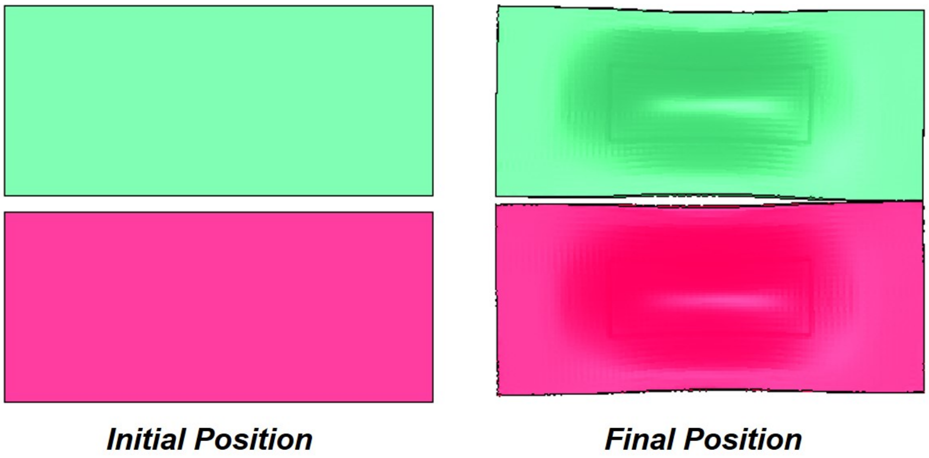

Figure 4.18: Polycarbonate Shield Translation at Later Stages of the Simulation

The retaining cover experienced high surface stresses near the windows. A maximum of 400 MPa was found near the edges of the windows of the retaining cover as shown in Figure 4.19. In addition, the back surface on the retaining cover also experienced high surface stresses, reporting a value of 420 MPa.

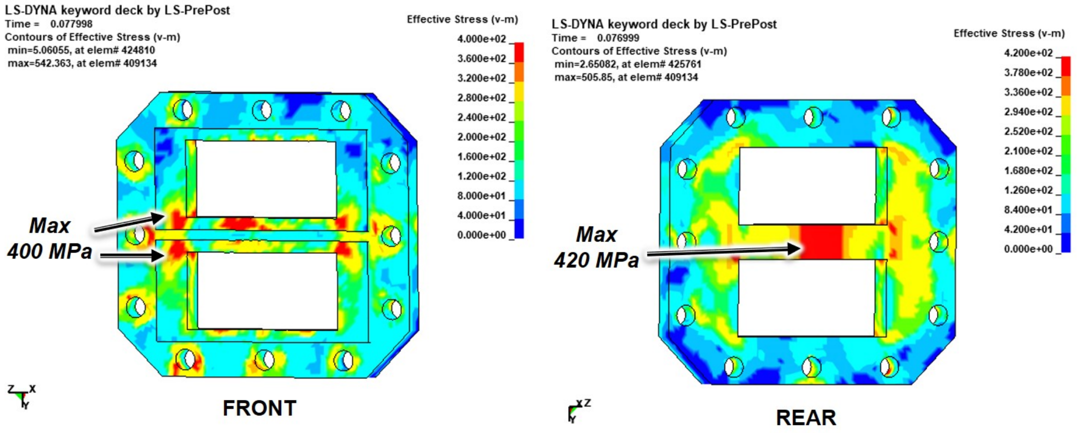

Figure 4.19: 1 MJ Retaining Cover Max Surface Stress

The part did marginally fail through the thickness of the center bar separating the two windows as shown in Figure 4.20. The stress developed matched the yield strength of the stainless steel, with a value of 340 MPa.

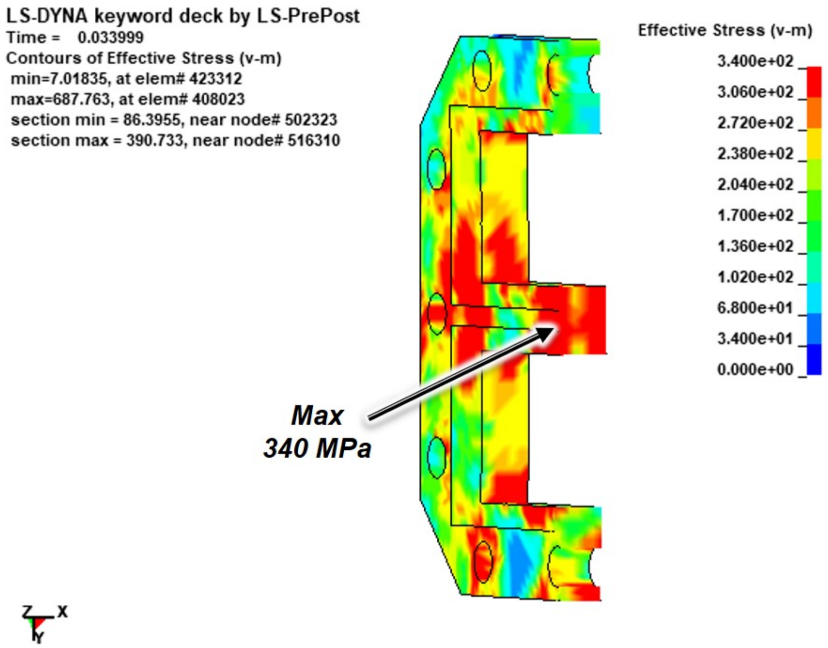

Figure 4.20: 1 MJ Retaining Cover Max Through Thickness Stress on Center Bar

Due to the stresses developed being close to the yield strength of the material, the plastic strain on the surface of the part was small with a reported max value of 10%. Through the thickness of the part, the plastic strain was less than 3%.

This set of parts would be usable for a one time use per experiment, as none of the parts failed catastrophically through the thickness for the plastic strain. A summary of the analysis results is outlined in Table 4.2.

Table 4.2: Results Summary for 1.0 MJ Load Case

Part	Surface Von Mises Stress	Surface Plastic Strain	Thickness Von Mises Stress	Thickness Plastic Strain
Nose-Cap	400 MPa	2%	<340 MPa	<1%
Tantalum	800 MPa	4%	<770 MPa	<2%
Polycarbonate	100 MPa	25%	90 MPa	<15%
Retaining Cover	420 MPa	10%	340 MPa	<3%

In the following simulations, parts are highlighted that showed significantly different results from the 1.0 MJ case. This includes parts that failed in specific regions that passed in the previous simulation. It was expected that higher stresses and therefore higher plastic strains would be developed in each of the parts.

4.2.2 Laser Energy: 1.5 MJ and Target Mass 1.0 g

For the higher energy case, similar results were produced for the nose-cap. Higher stresses were developed on the surface and through the thickness of the nose-cap. Both the center bar and the thin upper section of the nose-cap did yield through the thickness, matching the yield strength of 340 MPa and is shown in Figures 4.21 and 4.22.

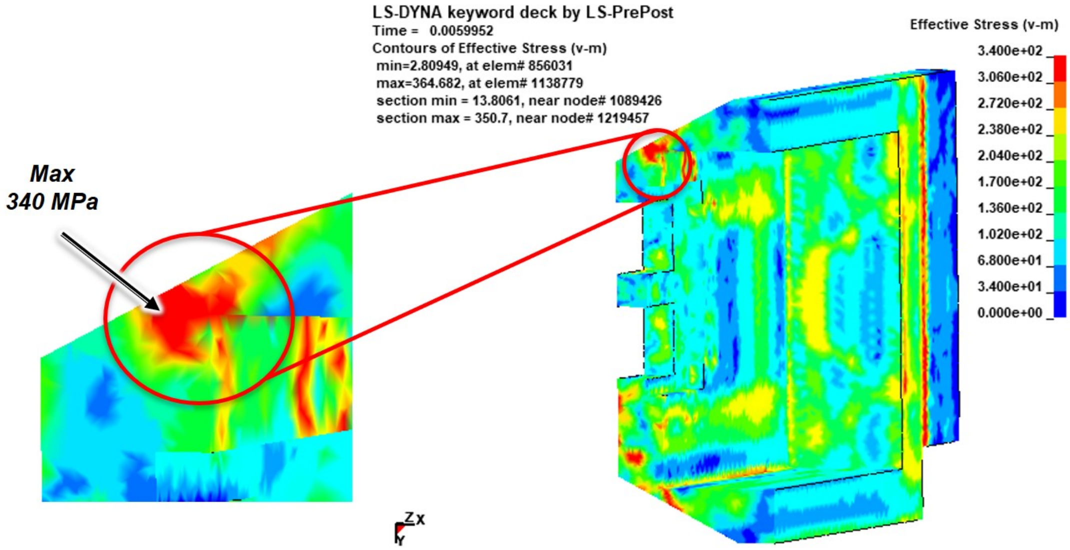

Figure 4.21: 1.5 MJ Nose-Cap Max Through Thickness Stress Through Thin Upper Section

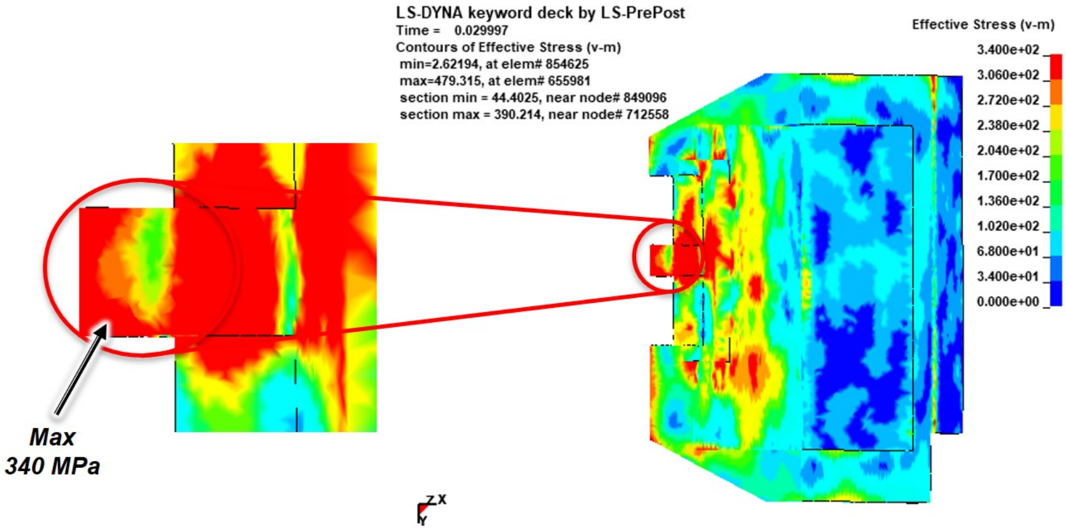

Figure 4.22: 1.5 MJ Nose-Cap Max Through Thickness Stress Through Center Bar

The max plastic strain still appeared at the bottom corner of the window on the nose-cap. This increased from the previous model but was still well below the plastic strain limit reporting a value of 3%.

Similar to the nose-cap, the tantalum covers, polycarbonate shields, and the retaining cover developed increased stresses and plastic strains. The stresses and strains scaled appropriately for the higher load case.

All of the parts failed the primary stress criterions for their maximum surface values. The nose-cap, polycarbonate shields and retaining cover all yielded through the thickness at certain locations for each part. These parts would still be used as one-time use parts based on these results. Table 4.3 contains the collected stress and strain values for the 1.5 MJ case.

Table 4.3: Results Summary for 1.5 MJ Load Case

Part	Surface Von Mises Stress	Surface Plastic Strain	Thickness Von Mises Stress	Thickness Plastic Strain
Nose-Cap	420 MPa	3%	340 MPa	<2%
Tantalum	820 MPa	6%	<770 MPa	<2%
Polycarbonate	110 MPa	35%	100 MPa	<20%
Retaining Cover	440 MPa	15%	340 MPa	<3%

For the remaining 2.1 MJ cases, the nose-cap and polycarbonate results were primarily highlighted. Due to the higher load case, it was expected for the retaining and tantalum covers to fail in the similar regions outlined previously.

4.2.3 Laser Energy: 2.1 MJ, Target Mass 1.0 g, 5 mm Thick Polycarbonate

As a first conservative model, a 5 mm polycarbonate shield model was created to monitor the stresses developed in the polycarbonate and nose-cap. Similar surface stresses were found as the 1.5 MJ case, with surface stresses close to 460 MPa for the nose-cap.

Similar to the lower energy levels, the center bar of the nose-cap failed through the thickness, with a reported stress at the material limit of 340 MPa. With the increased amount of material at the upper section of the nose-cap, the nose-cap did not fail through the thickness at this section as shown in Figure 4.23.

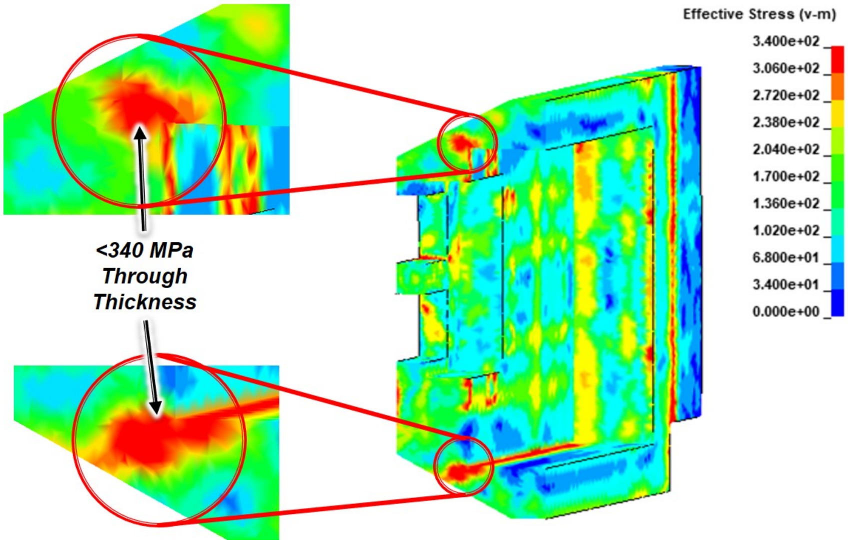

Figure 4.23: 5 mm Polycarbonate Model, Nose-Cap Max Through Thickness Stress on Upper and Lower Regions

In comparison to the other energy levels, the polycarbonate shields did not fail through the thickness. In Figure 4.24, max surface stress values at the limit of 80 MPa are found on the front surface of the polycarbonate. Conversely, through the thickness of the part an average value of 60 MPa was reported.

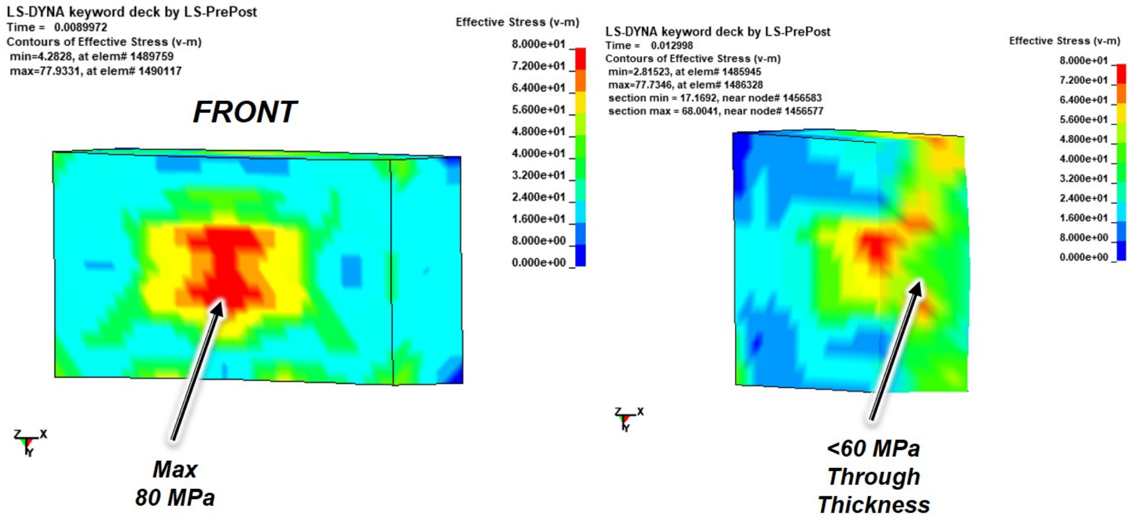

Figure 4.24: 5 mm Polycarbonate Shield Max Surface and Through Thickness Stresses

Finally, the plastic strain values for the polycarbonate were extremely low, with only a 2% reported value on the front surface, and an average value close to 1% through the thickness of the part as shown in Figure 4.25.

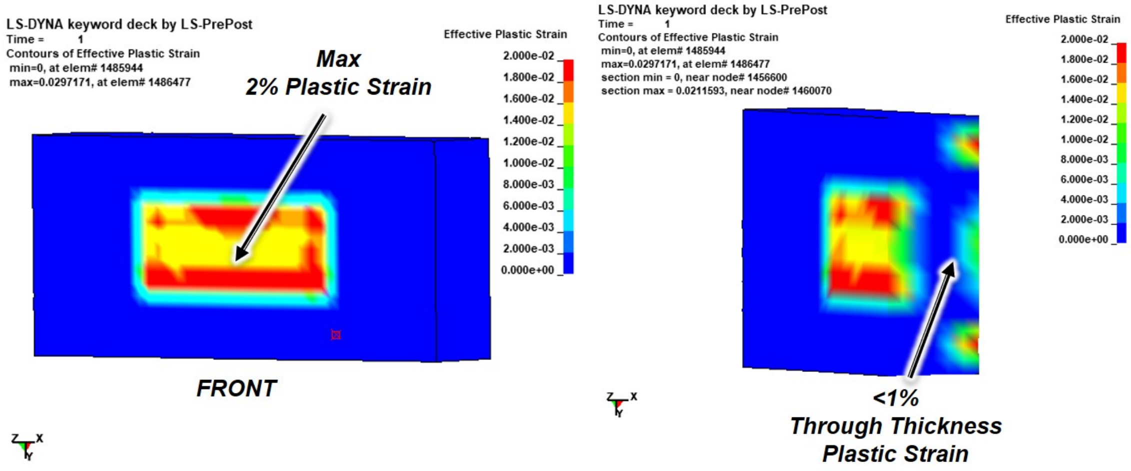

Figure 4.25: 5 mm Polycarbonate Shield Max Surface and Through Thickness Plastic Strains

Compared to the lower energy level simulations, the center bar of the retaining cover has completely yielded through the thickness. Depicted in Figure 4.26, the entire center bar has yielded through the thickness with a value of 380 MPa.

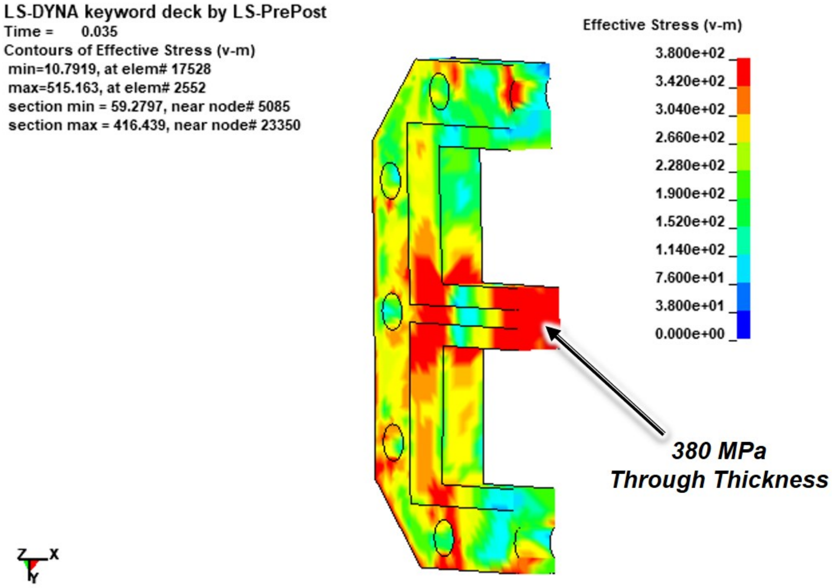

380 MPa
Through Thickness

Figure 4.26: 5 mm Polycarbonate Model, Retaining Cover Through Thickness Stress

While the polycarbonate shields and nose-cap performed better for this case, the potential energy loss with having extremely thick polycarbonate may be too large of a detriment to use. In addition, for lower Bragg angle crystals, potential interference can occur with the 5 mm polycarbonate shields. However, this model served as a baseline to determine the maximum polycarbonate thickness necessary to prevent major failure. A summary of the stress and strain results for each of the components are outlined in Table 4.4.

Table 4.4: Results Summary for 2.1 MJ, 5 mm Polycarbonate Load Case

Part	Surface Von Mises Stress	Surface Plastic Strain	Thickness Von Mises Stress	Thickness Plastic Strain
Nose-Cap	460 MPa	4%	340 MPa	<2%
Tantalum	820 MPa	3%	<770 MPa	<2%
Polycarbonate	80 MPa	2%	<60 MPa	<1%
Retaining Cover	480 MPa	3%	380 MPa	<3%

For the final simulation, the notable changes in the nose-cap and polycarbonate results are outlined.

4.2.4 Laser Energy: 2.1 MJ, Target Mass 1.0 g, 3 mm Thick Polycarbonate

For the nose-cap the center bar still yielded through the thickness. Illustrated in Figure 4.27, the upper and lower thin regions of the nose-cap had yielded through the thickness.

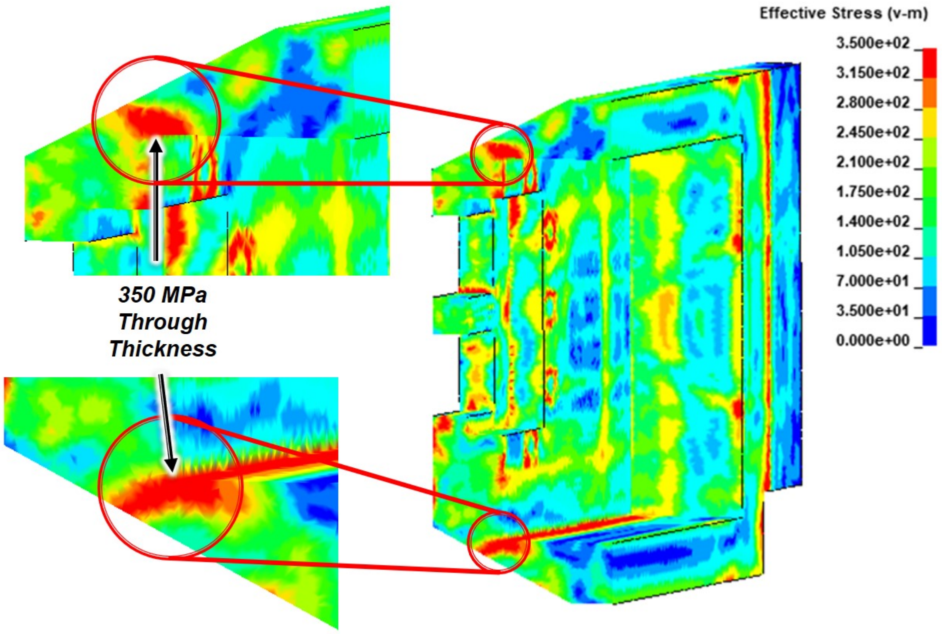

Figure 4.27: 3 mm Polycarbonate Model, Nose-cap Upper and Lower Regions Through Thickness Stress

The polycarbonate shields did experience higher surface and through thickness stresses. The surface stresses did exceed the yield strength for the material, but did not yield through the thickness. These results are shown in Figure 4.28.

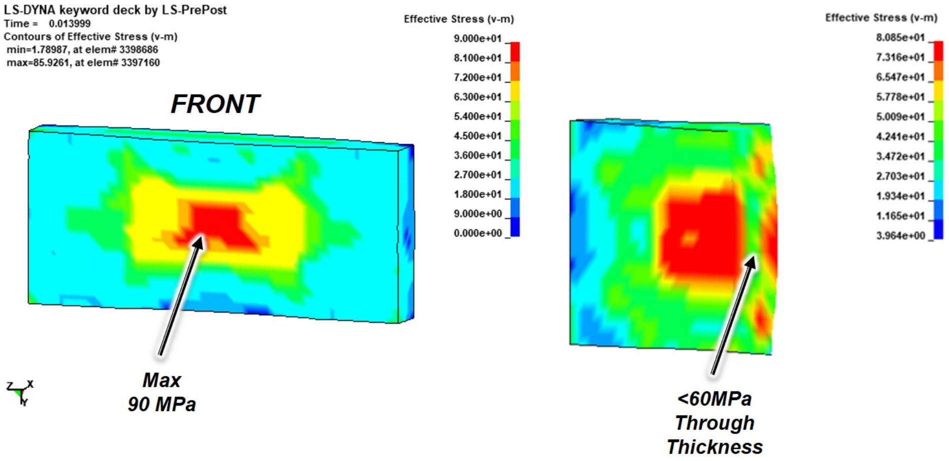

Figure 4.28: 3 mm Polycarbonate Shield Max Surface and Through Thickness Stress

Due to the higher stresses developed, larger plastic strain results were expected in comparison to the 5 mm polycarbonate case. For the surface plastic strain, the polycarbonate did not exceed the limit reporting a value of 10%. In addition, the through thickness plastic strain was reported to be less than 3% as shown in Figure 4.29.

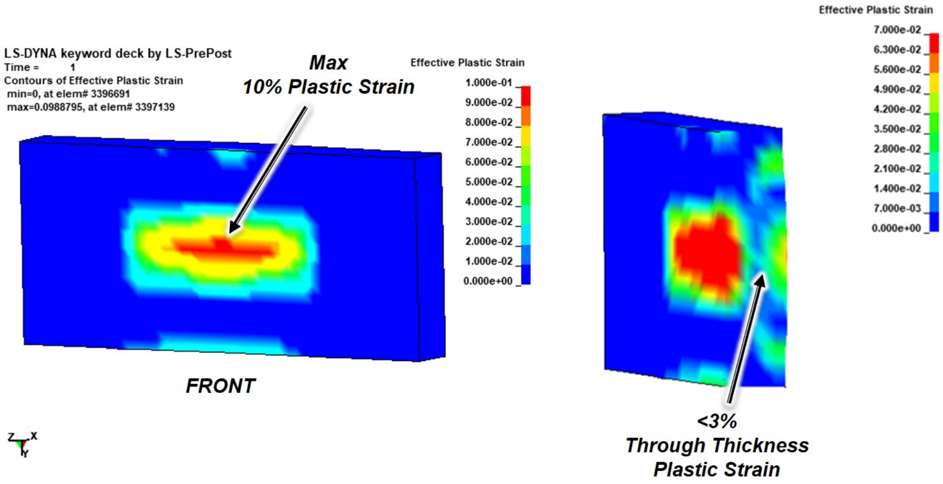

Figure 4.29: 3 mm Polycarbonate Shield Max Surface and Through Thickness Plastic Strain

The retaining cover results were similar to the 5 mm polycarbonate case, as the same failure region, the center bar, yielded through the thickness. In addition, due to the less stiff polycarbonate, the tantalum covers reported a marginally higher plastic strain value on the front surface. The collection of results for the 2.1 MJ, 3 mm polycarbonate case is outlined in Table 4.5.

Table 4.5: Results Summary for 2.1 MJ, 3 mm Polycarbonate Load Case

Part	Surface Von Mises Stress	Surface Plastic Strain	Thickness Von Mises Stress	Thickness Plastic Strain
Nose-Cap	460 MPa	3%	350 MPa	<2%
Tantalum	820 MPa	5%	<770 MPa	<3%
Polycarbonate	90 MPa	10%	<60 MPa	<3%
Retaining Cover	470 MPa	2.5%	360 MPa	<2%

Based on these results it is clear that both the retaining cover and the nose-cap would require a thorough redesign. Increasing the thickness for the center bar and upper/lower regions of the nose-cap should be the first priority. Considerations do have to be made to ensure that the protective components do not interfere with any of the potential crystal positions. In addition, for the retaining cover, larger bolt holes or increasing the overall thickness of the part would enable the part to survive at the higher energy levels.

Chapter 5

STAGE RESEARCH

Before design development began, thorough research was performed to learn more about optomechanical stages. Most companies and manufacturers typically use similar methods to achieve precise and repeatable motion for their stages. The purpose of this research was to investigate different methods used in industry to eventually develop a unique solution specific to the NIF's needs. This research focused on methods that could be used for both translational and rotational motion.

5.1 Linear Bearings and Dovetail Rails

One of the primary elements in linear translational stages is the use of linear bearings. Linear bearings can have either fixed or recirculating ball bearings, both of which are depicted in Figure 5.1. In a fixed configuration, the ball bearings are constrained to their housing and limited in their motion by the length of the linear bearing. In the recirculating configuration, the ball bearings within the linear bearing will cycle continuously through the bearing. This allows for a greater range of motion that is only limited by the length of the guide rail the bearing is mounted to.

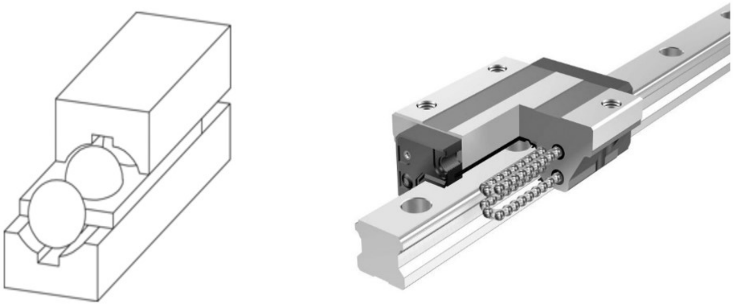

Figure 5.1: Example of Linear Bearings, Fixed (Left) and Recirculating (Right) Configurations [17]

Linear bearings are often used for low friction applications. The types of bearings used (standard ball bearings versus crossed) can greatly affect the load capacity and precision. For most small-scale stages, fixed linear bearings are often used since range of travel is not a limiting factor. Fixed linear bearings would be a preferred option for CBI, since the travel ranges are not large enough to require a recirculating scheme.

Another method commonly used for linear translation of optomechanical stages are dovetail railings. Dovetail railings are designed with mating sliding components, a stationary base and a moveable stage, as depicted in Figure 5.2. Dovetail railings are typically more cost effective in comparison to linear bearings. In addition, dovetail railings can be designed for any volume, as the length of the rails is the only limiting factor. One of the main drawbacks of dovetail railing stages is that stiction is a common issue due to sliding between mating components. However, this issue could potentially be circumvented by applying grease to the stages. In terms of precision, dovetail railings can match the precision of linear bearing stages, since this is primarily driven by how they are actuated. However, due to the low friction nature of linear bearings, linear bearing stages are capable of achieving more consistent, repeatable motion.

Figure 5.2: A dovetail translation stage sold by Thorlabs [18]

5.1.1 Actuation Methods and Common Applications of Linear Stages

The resolution of these linear translational mechanisms is determined by the actuator driving them. Fine pitch screws or linear actuators are typically used to manipulate linear stages. For high resolution stages, high thread per inch screws are typically used in the range of either 80 to 100 threads per inch. If electronic components can be used, linear actuators available on the market are capable of minimum translations of close to 0.1 μm. Linear actuators are generally an appealing option to use for stage alignment. However, an electromagnetic pulse (EMP) can be produced through the interaction of high intensity laser light with the target during an experiment. This can cause the actuators to be permanently damaged. As such, pure mechanical actuators would be preferred to manipulate the stages for CBI.

For stages to maintain their position, springs are often used to implement a restoring force if the stage is forcibly displaced. Set screws are also often used to help lock the stages in place once the stage is aligned. For most stages available in industry to achieve multiple degrees of freedom, several one directional stages are stacked together. An example of this is shown in Figure 5.3, several one directional stages are stacked together to achieve 3 independent directions of motion. This is often done to mitigate possible sources of cross coupled movements where packaging is not a major constraint.

Figure 5.3: Example of Stacked 1-D stages to Achieve 3 Degrees of Freedom sold by Siskiyou [19]

5.2 Gimbals and Goniometers

To achieve accurate rotations about an axis, there are several methods used in industry. One common method is the use of gimbals. Gimbals are often used in the aerospace industry for navigation as well as imaging applications to accurately track moving objects. Gimbals allow for 3 degrees of freedom, allowing rotations about a singular point typically about its center. One drawback with gimbals is their size, leading to potential issues with packaging. In smaller applications, it may be difficult to fit a gimbal system that is closely packaged around the optic itself. In these cases, goniometers can be used which operate under similar principles as gimbals.

Goniometers are similar to gimbals by virtue of having a fixed rotation point. However, this rotation point is projected out at a fixed point in space rather than about the center of the mechanism itself as depicted in Figure 5.4. The major advantage to goniometers is their relatively small size. For CBI, goniometers could be placed behind the crystal itself to allow for pure rotations about the crystal surface. Most goniometers have a curved radius base and moveable stage. The fixed curved base will have a matching radius to the point projected in space. The sliding interface between the base and stage is commonly a curved linear bearing but dovetail rails are used as well for cost-friendly applications.

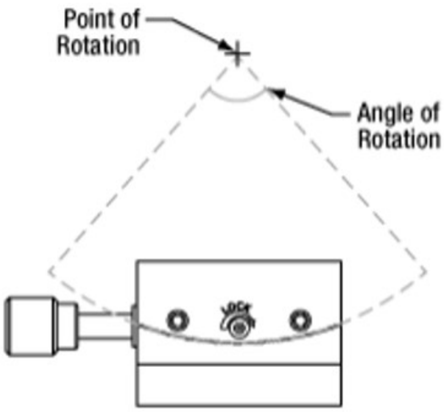

Figure 5.4: Schematic of a Goniometer with a Fixed Point of Rotation [20]

Goniometers on the market can have a travel range of ± 10° and a precision close to 0.15° (which is worse in comparison to the current CBI stage). Most standard goniometers on the market do not allow variable or adjustable radius of curvature. As such, one of the main drawbacks of a goniometer is the lack of versatility, as mounting hardware may need to be varied for the same goniometer to be used in different applications. However, if the goniometer is to be used for only one application this drawback is easily circumvented.

5.3 Flexures

Flexures can be defined as elements that allow movement in specific degrees of freedom but maintain rigidity in all other directions of motion. Flexures are used in several day to day items, such as nail clippers and living hinges as shown in Figure 5.5. For optomechanical applications, flexures are commonly used to achieve precise motion for alignment stages by purposely deflecting flexible elements. Flexures can be difficult to design to isolate translations or rotations about any of the three principle axes, while also maintaining rigidity in all other directions. Maintaining rigidity in the other degrees of freedom is important in reducing the amount of parasitic motion. Parasitic motions or errors are deviations from a stage's intended direction of travel [21]. Parasitic motion can be difficult to predict when designing flexures. With the appropriate actuator locations, the amount of parasitic motion can be minimized. However, knowing where to properly place actuators or creating a stiff flexure in the appropriate directions can be difficult for an inexperienced flexure designer. Luckily, a methodology has been developed to help engineers build a foundation for flexure design. By employing the FACT methodology, constraints and actuation directions can be defined to ensure isolated motion in the desired degrees of freedom [21].

Figure 5.5: Examples of Flexures in Common Items, Living Hinges (Left) [22], **Nail Clippers (Right)** [23]

5.3.1 FACT Methodology

FACT stands for Freedom, Actuation and Constraint Topologies and is used for creating flexure designs [21]. FACT is a powerful tool, allowing the user to visualize the necessary constraints for desired ranges of motion when designing a flexure system. There are a few specific terms that need to be defined before using the FACT methodology: twists, wrenches, freedom and constraint spaces. Twists describe lines of action that are allowable degrees of freedom. These lines can describe pure rotations (shown in red) and translations (shown in black) or a combination of both as represented in Figure 5.6. Wrenches describe lines of constraint and can be representative of pure forces (shown in blue) or moments (shown in black) to prevent deflection in unwanted directions. A freedom space is the 2 or 3-dimensional representation of allowable motion for a flexure. Conversely, the constraint space is the culmination of wrenches that constrain a flexure in the remaining degrees of freedom. An example of a freedom space and its corresponding constraint space is shown in Figure 5.6.

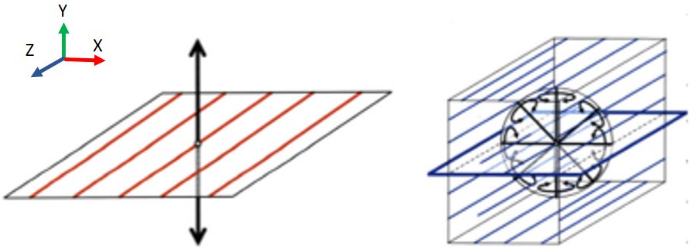

Figure 5.6: Example of a 2-DOF, Freedom and Constraint Space [21]

In Figure 5.6 the parallel red lines represent the plane of allowable rotations along the Z-axis, in addition to allowable translation in the Y-direction. This system would be a 2 DOF system that would allow for translation in one direction and rotation about a single axis. To prevent movements in other directions, four independent wrenches would need to be implemented. These wrenches could be applied parallel to the rotation axis as pure forces (indicated by the blue lines). The system can also be constrained by any of the pure torques that is perpendicular to the plane of the freedom space. Any combination of 4 independent wrenches out of these options would constrain the flexure entirely.

A designer must be careful to implement enough independent constraints to prevent unwanted motions in other degrees of freedom. Independent constraints can be difficult to visualize, but usually if all lines of constraint do not meet at the same point in space or are parallel to one another they can be considered independent. The number of independent wrenches necessary is found by the simple relationship:

$$6 = m + n \tag{5.1}$$

Where n is the degrees of freedom and m is the number of independent wrenches. Redundant wrenches can be implemented in a system to increase the rigidity of the system but will affect the dynamics and load capacity of the system [21].

With the FACT methodology, Figure 5.7 can be used to quickly determine the constraint spaces required for the desired range of motion. The chart contains the freedom and constraint spaces to achieve any type of motion desired for a flexure system.

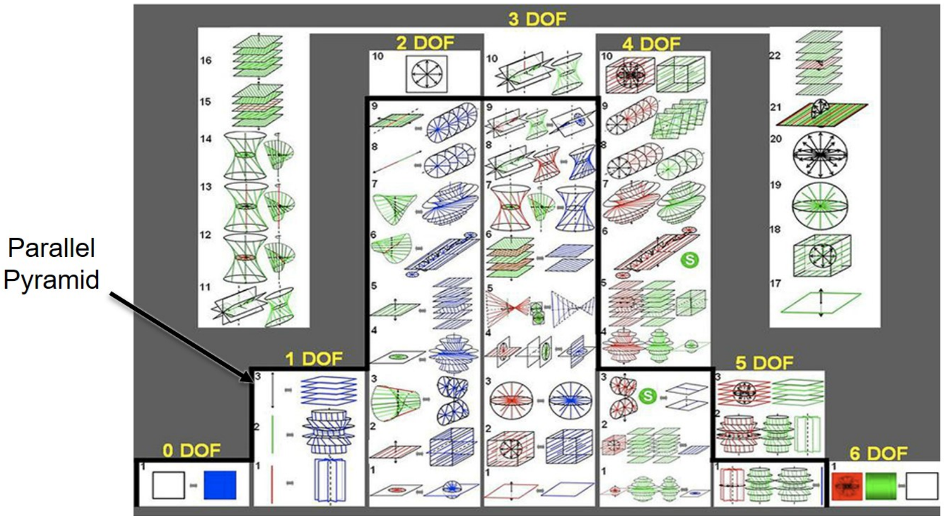

Figure 5.7: FACT Chart for Flexure Design Synthesis [21]

The FACT chart contains a bolded line boundary, which is referred to as the "parallel pyramid". Within this pyramid, it is possible to design a parallel configuration flexure to achieve the desired range of motion. However, if the desired flexure design lies outside the pyramid, this would require a combination of parallel flexures stacked serially to achieve the range of motion. The concept of parallel and serial configurations for flexures are shown in Figure 5.8.

Parallel Serial

Figure 5.8: Examples of Parallel and Serial Configurations for Flexures [21]

In flexure stages, parallel and serial configurations are commonly used to describe a stage. In a parallel configuration, multiple actuators can push against the same stage, and allow for the desired degrees of freedom. However, with a serial configuration multiple parallel stages are nested together, and through the combined motion are able to achieve the desired motion. The nested stage is often referred to as an intermediate stage, which connects from the ground, or nonmoving component, to the desired motion stage.

As an example, utilizing the FACT chart shown previously in Figure 5.7, consider the flexure design at the top of the 2 degrees of freedom column. This flexure design allows for planar translation. Since the design lies outside of the parallel pyramid, two parallel designs must be selected from a lower degree of freedom. To achieve this range of motion, 2 parallel flexure designs in the 1 DOF column will be combined to allow for planar translation as shown in Figure 5.9. This would require the necessity of an intermediate stage with ends connecting to ground and the main stage.

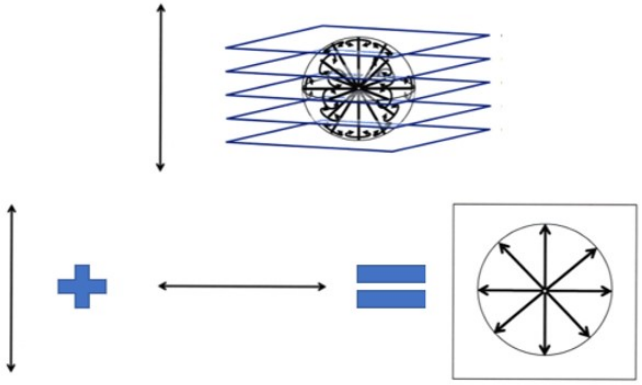

Figure 5.9: Combination of 1-DOF Freedom Spaces to Produce a Planar 2-DOF Translation Freedom Space [21]

Flexure stages have been used for several applications at the NIF. This is primarily due to their high versatility and capabilities of achieving any desired degrees of freedom. After overcoming the initial learning curve, flexures can be a powerful design tool when designing high precision stages.

5.4 Piezoelectrics

The methods above utilize mechanical elements to translate and secure stages in place. Another method used for optics alignment is piezoelectrics. Piezoelectrics are materials that change in size in the presence of an electric field. The reverse applies as well, with electric fields being produced when the material is deflected. These changes in size can vary from microns to nanometers.

A standard method used to translate piezoelectric stages is colloquially known as the inchworm method. Figure 5.10 provides an example schematic of the inchworm method.

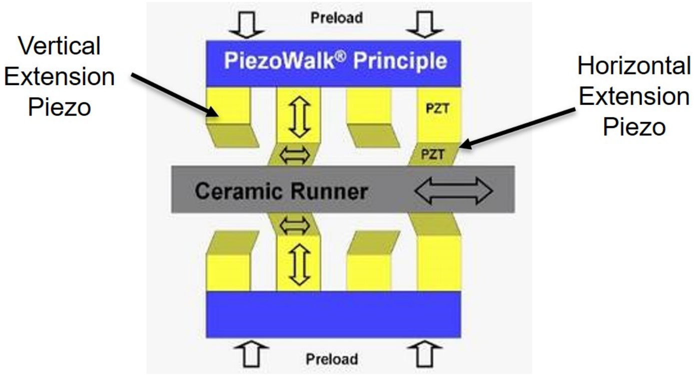

Figure 5.10: Example of Piezoelectric Inchworm Technique [24]

This method works by two plates with piezoelectrics stacked in series that surround the moveable stage. The piezo stack that connects to the plate is able to expand and contract vertically. Another piezo stack is connected to the previous stages that is capable of displacing horizontally. The vertical piezo stack is first actuated to make contact with the moveable stage. Once contact is established, the second stack can then be displaced to translate the stage side to side. The stage can be moved at a maximum distance based on the horizontal travel of the second piezo stack. If further travel is required, the vertical piezos are relaxed to release contact with the moveable stage. The horizontal piezos are then actuated back to their original position. The process can then be repeated, by establishing contact with the vertical piezos and actuating the horizontal piezos, the moveable stage can be continuously translated horizontally.

Piezo-stages are often paired with either flexures or linear bearings, to allow for precise straight motion. With clever positioning, flexure stages can be designed with integrated piezo actuators to allow for extremely compact designs as shown in Figure 5.11.

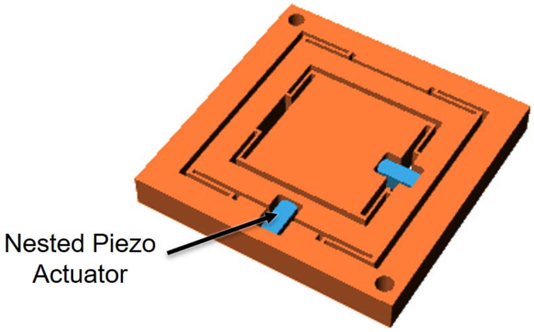

Figure 5.11: Example of Nested Piezoelectric Actuators in Flexure Stages [25]

Using piezoelectrics in the target chamber poses some risk. Similar to the linear actuators, an EMP produced from an experiment could permanently damage the stages. While piezoelectrics can boast precise and accurate motion, they are very expensive and can be costly if they would need to be replaced often. Piezoelectrics could still be considered if they were mounted in a diagnostic for several experiments. If the stages are still capable of precise movement after being exposed to several experiments, they could be considered for use as a design solution.

Using the methods in this chapter it is possible to design a system that would outperform the current CBI stage.

Chapter 6

DESIGN DEVELOPMENT

During the design development, the procedure for developing a workable design progressed by researching multiple translation methods in parallel. The philosophy for designing the translation methods for the system was to examine each of the degrees of freedom individually. Once a translation method for one degree of freedom was selected or “locked in” the remaining degrees of freedom would be designed to interface with it. Naturally, this necessitated an iterative process since each degree of freedom was coupled with the rest through the system’s packaging. This process required balancing the performance of each mechanism and ensuring each component could be packaged in the housing together.

6.1 Initial Modifications to the Housing

The original housing was meant to accommodate for a one crystal system. From the constraints outlined in the ray tracing model, both crystals were to be separated vertically from the equatorial plane by 7 mm. With this spacing, the upper crystal becomes at risk with colliding to the ceiling of the housing. The overall separation from the ceiling to the crystal was less than 0.5 mm as shown in Figure 6.1.

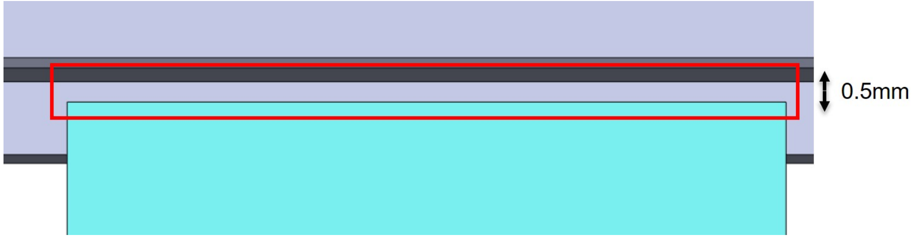

Figure 6.1: Clearance Between Top Crystal and Housing

In the original system, cutouts were created in both the housing and the nose-cap. These cutouts allow for the alignment cameras to still have line of sight to the ”snout” of the diagnostic when the CBI arm is lowered and then inserted into the target chamber. However after further review, the arm was lowered by a large enough amount that the cutouts on the housing were not visible on the alignment cameras. As such, the cutouts could be removed from both the nose-cap and housing. This allowed for a slight modification to the housing. The ceiling was raised by a couple millimeters that would previously interfere with the cutouts. In Figure 6.2, the first housing modification is shown with the increased height dimension.

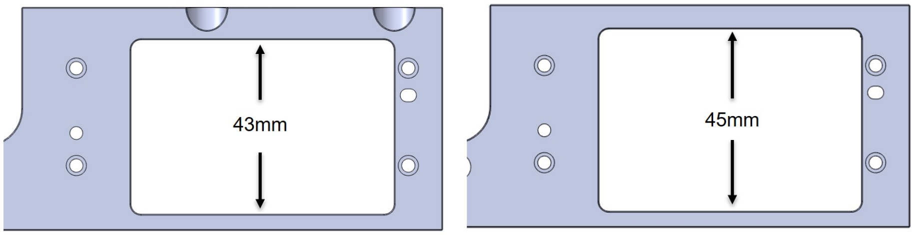

Figure 6.2: Original Housing (Left), Modified Housing with Increased Height (Right)

By raising the ceiling of the housing by 2 mm, the original housing had a new overall height of 45 mm. This was a minimal change that was required to minimize the risk of damaging the crystals during alignment.

6.2 Early Development

From the ray tracing analysis, it was apparent that the alignment system would need to be split into two different adjustment mechanisms. A coarse alignment paired with a precision adjustment system would be the most space efficient option. Most fine precision stages with long stroke (10-20 mm range) are large in terms of footprint and height. An optimal solution would be a compact coarse alignment stage that could be adjusted to set positions. These set positions would align the crystal close to the desired location. The precision stage would then tune the crystal position the remaining few millimeters with high precision.

Concepts for a few coarse adjustment mechanisms were considered early in the design process. In most optical bench settings, large dovetail railings are used to translate optics quickly and smoothly. Most dovetail systems include a locking mechanism that is native to the moveable part (see left of Figure 6.3). Another consideration was to include a pinboard set. A plate could be installed in the original housing with varying sets of pin locations that the precision stage could be inserted into as depicted by the right of Figure 6.3.

Figure 6.3: Thorlabs Dovetail Rail Carrier (Left) [26] **and Pinboard Concept for Coarse Adjustment (Right)**

These coarse adjustment mechanisms could be implemented if the precision stage was small enough in size. In terms of design focus, the precision stage had a higher priority, and an interfacing coarse adjustment stage would be considered after a precision system was proposed.

Due to the height of the housing being the primary constraint for packaging the 5 DOF stages, low profile options were considered first. For most commercial applications, to achieve multiple directions of principle translations, linear stages must be stacked on top of one another. Besides piezoelectrics, most commercial options are relatively tall in comparison to the available height in the housing as shown in Figure 6.4.

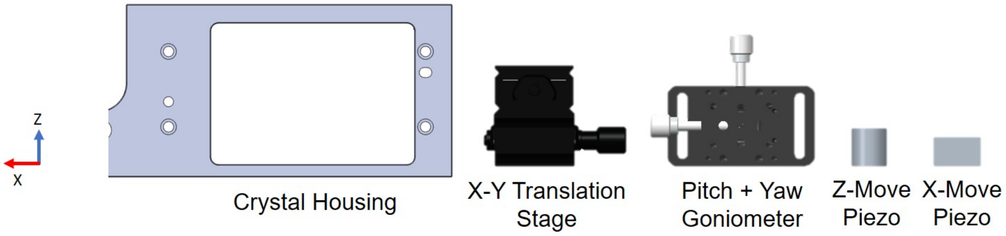

Figure 6.4: Comparison of Commercial Stages Relative to the Crystal Housing

While these stages would fit within the packaging, they would require unique mounting schemes in cases where the crystals were positioned over one another. For precision travel stages, vertical stages were attacked first to determine possible packaging constraints. The primary concern was due to the height of the housing.

6.2.1 Vertical Travel

One of the early challenges identified would be achieving precise vertical travel, since the primary housing constraint was the height. Most stages designed for precision vertical translation use linear bearings to control the motion. However, most of these are extremely tall with some commercial stages having a height of 45 mm and above [27]. This is primarily due to the height of the stage being determined by the length of the linear bearings.

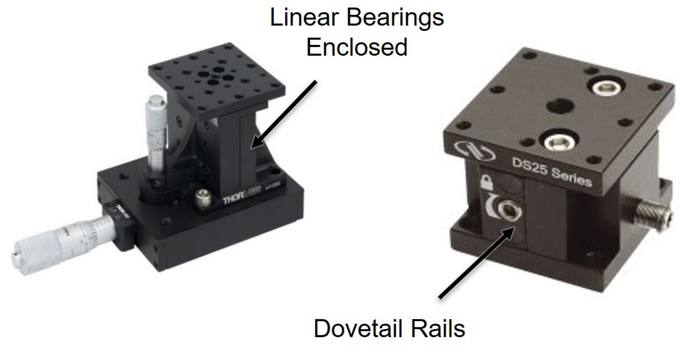

Figure 6.5: Commercial Vertical Stages, Linear Bearing Style from Thorlabs (Left) [27]**, Dovetail Railing Stage from Newport (Right)** [28]

After discussions with a linear bearing manufacturer, the smallest linear bearing they could produce was 12 mm in length. Considering the surrounding hardware for the fixed and moveable stages, a custom solution could be created that was close to 20 mm in height (allowing for a stage and base thickness of 4 mm). However, concerns arose with the capable range of travel, since most of the rolling elements in the bearing would be removed, reducing the possible displacement. Compact dovetail designs are available on the market as well, that are close to 23 mm in height as seen in Figure 6.5. These components would be able to fit in the housing but would require a side by side configuration. While this could potentially serve as a design solution, this would greatly impede on the available space for the remaining degrees of freedom. A low-profile vertical stage would be required to allow for more freedom with designing the remaining stages.

A vertical travel stage that would easily interface with other stages was not apparent from initial designs. Rather than coming to a solution that would greatly hinder the possibilities of other translation stages, vertical translation stages would be re-evaluated once other design solutions were proposed. Since it was clear that low-profile components would be required to package the other stages, initial concepts turned to flexures due to their flexibility in design.

6.3 Flexure Design

With flexures being so common in industry there has been plenty of research and development performed on the design of planar X-Y flexure stages. A common application for X-Y flexure stages are micro-electronic-mechanical systems (MEMS), for precision table translations notably in silicon wafer manufacturing [29]. For planar X-Y flexure design, the main focus of development is to maximize the range of travel for a given footprint. For perspective, a planar X-Y stage developed by Qingsong Xu was capable of covering an 11 by 11 mm workspace with a footprint close to 120 by 120 mm (a workspace to footprint ratio of less than 1%) [30]. A primary goal of the flexure design was to attempt to miniaturize several designs from literature while still maintaining an adequate workspace to footprint ratio.

One design that was generated was inspired by a design proposed by Shorya Awtar [31]. In his thesis, he proposed several X-Y flexure stages for large travel applications. One variant of his proposed Biflex design was a more compact version at the cost of additional intermediate stages to support the motion stage as shown in Figure 6.6. The design utilizes a series of double parallelogram flexures and two intermediate stages to allow for theoretically pure translations in the X and Y directions.

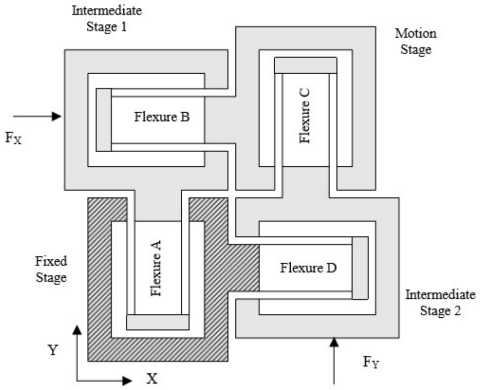

Figure 6.6: Compact Biflex Design [31]

One of the fundamental cruxes of the Biflex design is the implementation of two separate intermediate stages. The purpose of these intermediate stages is to allow for independent motion and actuation that does not affect one another [31]. Depicted in Figure 6.7 is a simplified model of Awtar's Biflex flexure design.

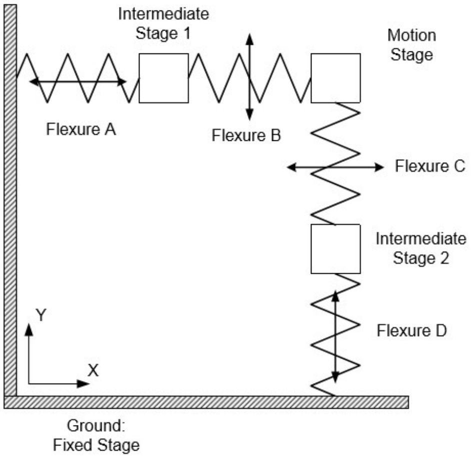

Figure 6.7: Simplified X-Y Flexure Topology [31]

Flexure units B and D will only allow for translations applied in the Y direction. Conversely, flexure units A and C will only allow for translations applied in the X direction. Regardless of the position of the motion stage, the actuation points on the intermediate stages 1 and 2 will remain the same to allow for predictable planar motion.

Common flexural elements used to achieve precise motion include the single and double parallelogram flexures. A single parallelogram flexure is capable of translating in one direction, however some parasitic motion and rotation is developed when actuated. This can be predicted from beam-bending analysis, that with some actuation force the structure would translate in the direction of the force. However, there will be additional in-plane motion that is perpendicular to the applied force as shown in Figure 6.8. The parasitic rotation can be eliminated with the proper application of the force, but the perpendicular translation will occur regardless of actuation placement.

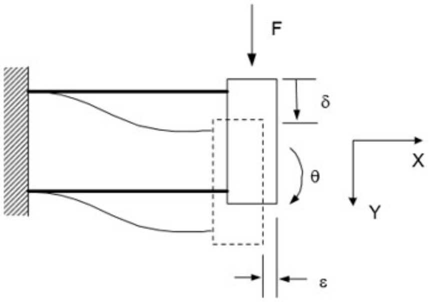

Figure 6.8: Parasitic Motion of a Single Parallelogram Flexure Unit [31]

A double parallelogram flexure is capable of minimizing the parasitic motion with the addition of a secondary stage. The double parallelogram flexure can be split up into three separate bodies. As noted in Figure 6.9, component B is the primary motion stage and is connected to a secondary motion stage. This secondary motion stage is connected to components A that are fixed relative to B. With the proper application force on B, the secondary stage takes on the translational parasitic motion, while the main stage translates in one direction relative to the flexural components.

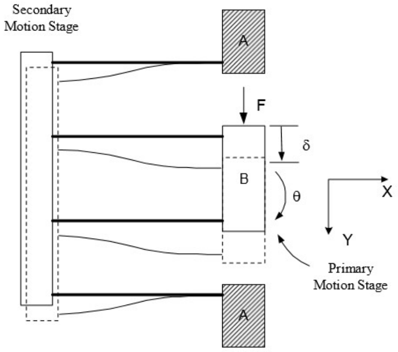

Figure 6.9: Double Parallelogram Flexure Unit [31]

This flexural unit is highly dependent on the location of the application force to minimize the amount of parasitic motion. The implementation of a secondary stage is leveraged to allow for nearly pure translations with flexural stages.

The Biflex flexure can also be analyzed with the FACT topology to ensure that the proper constraints are implemented to ensure degrees of freedom in the planar directions. Based on the FACT topology, since a X-Y planar translation flexure lies outside the parallel pyramid, two parallel flexure designs must be combined to create a serial flexure [21]. The parallel flexure designs chosen are the 1 degree of freedom spaces that allow for linear translation as shown in Figure 6.10.

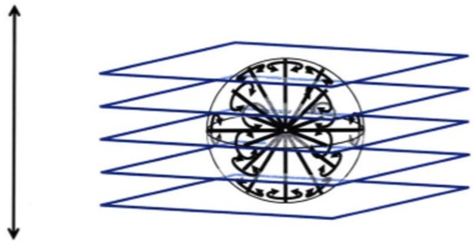

Figure 6.10: Freedom Space (Left) and Constraint Space for Pure Translation (Right) [21]

For a planar X-Y flexure, only one intermediate stage would be required to connect to ground and the intermediate stage.

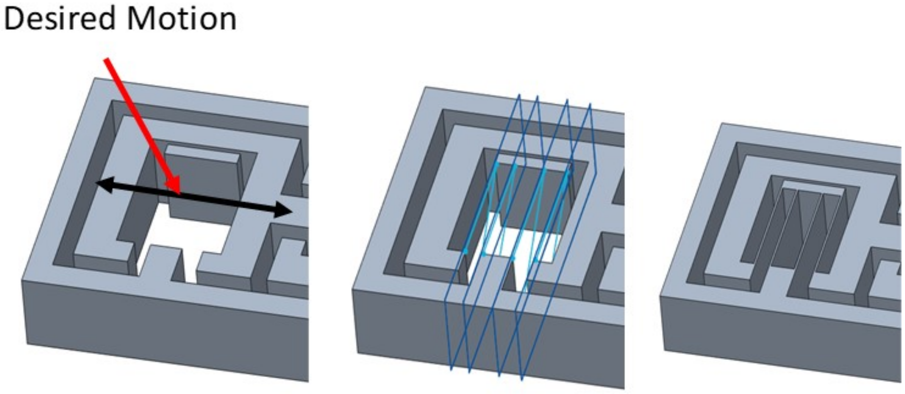

Figure 6.11: Intermediate Stage Constraints Connected to Ground

Recall for 1-directional travel, the constraint space consists of perpendicular planes to the direction of travel. Any line that exists on these perpendicular planes can serve as a flexible constraint. Depicted in Figure 6.11, the perpendicular planes can be visualized as the connections for the double parallelogram flexures. These constraints would connect the intermediate stage to ground. The same process can be repeated for the connection to the motion stage as shown in Figure 6.12.

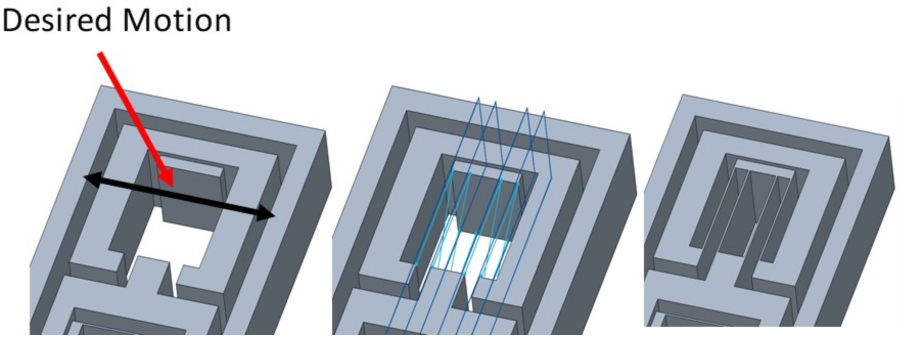

Figure 6.12: Motion Stage Constraints Connected to Intermediate Stage

This stage would be capable of 2 degrees of freedom travelling in the planar directions. This simple building block would suffer in performance due to the lack of actuator isolation. Actuator isolation is the decoupling of the actuator applied force and the position of the main stage. One actuator would act on the intermediate stage while a perpendicular actuator in-plane would act on the motion stage. Depending on the position of the motion stage, the intermediate actuator location would vary. This would result in unwanted parasitic motion preventing pure translations to occur. To circumvent this, the Biflex design merely mirrors and doubles the amount of flexural units to have each intermediate stage motion independent from one another. A variant of the Biflex design with hard stops is illustrated in Figure 6.13.

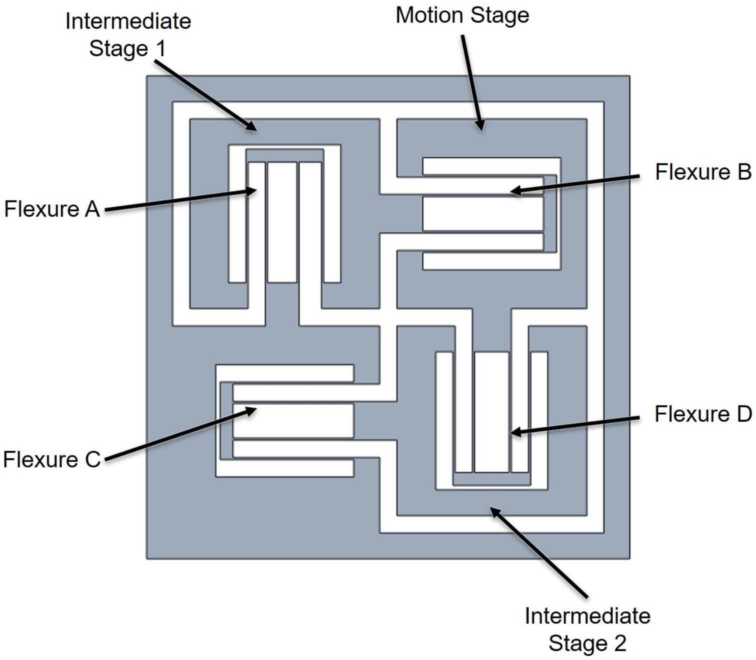

Figure 6.13: Compact Flexure Design with 2 Intermediate Stages

The relative motion between each flexural component can be difficult to visualize. Figure 6.14 provides a visual guide for the relative motion depending on each independent actuation force as well as the combined forces.

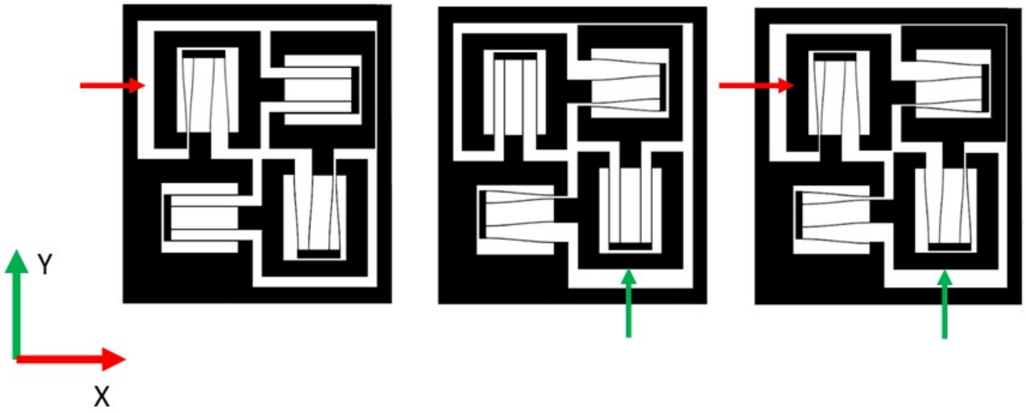

Figure 6.14: X Applied Force (Left), Y Applied Force (Middle), Combined Forces (Right)

In the combined forces case, it is apparent that the translation of the opposing intermediate stage has no bearing on the position of the other intermediate stage. This allows for the applied force to be at the same location repeatedly. In turn this allows for predictable and repeatable planar translations from the stage.

To size the length of the blade flexure, stiffness relations were used to determine the maximum range of travel [30]. Other parameters such as the Young's Modulus, blade flexure thickness and yield strength were necessary for the stiffness calculation. The Young's Modulus and length both play a key role in the total deflection of the flexure. In addition, the yield strength of the material contributes to determining the range of travel before the material yields. To maximize the range of travel, a material with a large ratio between yield strength and Young's Modulus is desired. For high performance, a common flexure material is Titanium 6AL-4V. Titanium is common due to possessing a higher yield strength than materials like aluminum but are less stiff than materials like stainless steel. These properties are advantageous to allow for larger deflections without yielding and would effectively increase the workspace to footprint ratio. The equations used to determine the appropriate blade flexure lengths can be found in Appendix C. Hand calculations to estimate the stresses developed for the blade flexures can also be found in Appendix C. The main constraints on the overall footprint of the design was dependent on the length of the blade flexures. In addition, the thickness for the motion stages and intermediate stages had to be large enough to allow for other stages to be mounted on. Both of these factors were the main contributors for determining the footprint of the X-Y flexure. Using the blade flexure relations, a maximum travel of 2 mm can be achieved for a 14 mm blade flexure. To be conservative, the travel range was reduced to 1.5 mm to prevent accidentally overdriving the flexure and causing the blade flexures to yield.

To translate the stages, two 100 thread per inch screws would push against each of the intermediate stages. With a direct drive system, this would match the desired resolution requirement. Issues with stiction would be eliminated due to the lack of sliding components present in flexures.

After struggling to find an appropriate vertical travel stage, implementing vertical travel capability was considered with the flexure. Rather than having the flexure secured to the housing, a kinematic mount was implemented with the flexure. Three points of contact were established, the classical form of a spherical, v-groove and flat contacts were implemented underneath the stage. This combination of contacts guarantees that a system will not be over-constrained and is common in optomechanical stage designs. Newport Corporation provides these contacts as pads that can be installed on any optomechanical stage [32]. At these points of contact, fine pitch screws can actuate underneath to raise and lower the stage. The modified Biflex stage that implements the kinematic mounts is illustrated in Figure 6.15.

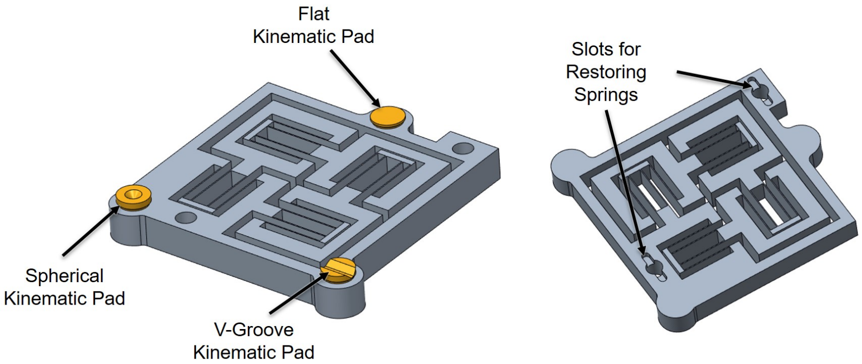

Figure 6.15: Kinematic Mount and Restoring Spring Element for the X-Y Flexure

To safely secure the mount, a restoring spring element was implemented as well. Slots were cut out where a pin would rest inside the flexure. A compression spring would be held between the pins to apply a pre-load force to secure the stage against the housing. One drawback with this implementation was the cross coupled motion between pitch, roll and vertical travel. While the use of spherical crystals negates issues with roll alignment, the pitch adjustment would be affected unless all three screws were actuated the same amount. While this was not an ideal solution, it was still considered due to struggles with finding an appropriate vertical travel stage at the time.

Currently, the compact Biflex was only capable of travelling in 1.5 mm in the positive X and Y directions. To maximize the space of the flexure, it was desired to have the stages be capable of traveling in the negative X and Y directions as well. However, to maintain actuator isolation, actuation points in contact with the motion stage was undesirable. Instead, a restoring spring was used once again to provide a preload force. Restoring spring elements were positioned inside each of the intermediate stages. From Figure 6.16, sets of pins were held against slots on the outer fixed sections of the flexure as well as inside each intermediate stage.

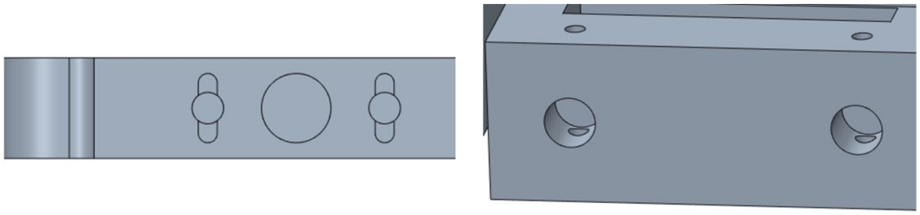

Figure 6.16: Slots for Restoring Springs and Pins in Intermediate Stages

With this implementation the flexure stage would be capable of translating ± 1.5 mm in either the X or Y direction. If necessary, the stage would also be capable of vertical travel of 2 mm with the kinematic mount implementation. Holes in the motion stage were implemented to allow for either a vertical travel or pitch-yaw stage to be attached to. The final iteration for the modified Biflex design is shown in Figure 6.17.

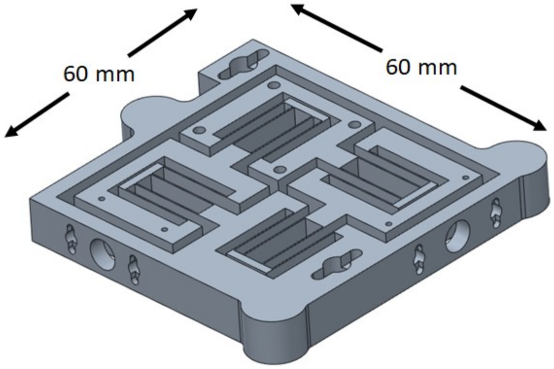

Figure 6.17: Final Iteration of the Compact Biflex Stage

6.3.1 Implementation into the Housing

The flexure design was implemented into the housing to check for any potential packaging issues. Rather than the typical setup with the motion stage in the upper-right corner, the stage was rotated to accommodate for manipulation from the back and side of the housing. The addition of the kinematic mount would require for adjustment underneath the housing. To be capable of adjusting the top crystal, the flexure would need to be mounted to the ceiling of the housing. This could be achieved easily, but a modification to the housing was considered to improve the user-friendliness of the system. A cutout was made on the roof of the housing, that a mating pallet could slide into. The pallet would have the slots and pins for the vertical travel elements but could serve as an offline mounting scheme. The remaining components for the 5 DOF stage could be safely mounted on the flexure and pallet assembly, then slid into the housing. The pallet would then be secured to the housing where the stages could be adjusted to align the crystals. The pallet assembly and implementation of both flexures in the housing are depicted in Figure 6.18.

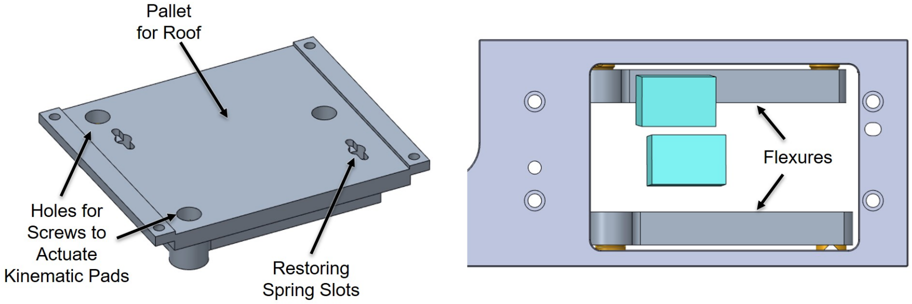

Figure 6.18: Pallet Assembly (Left) and Flexure Implementation in the Housing (Right)

At this point in the design, the precision motion for the X-Y flexure stage was locked in, and the remaining degrees of freedom were explored. The pitch and yaw mechanisms were explored next to determine their compatibility with the flexure stage.

6.4 Pitch and Yaw Mechanisms

Early on a few pitch-yaw mechanisms were considered. A possible solution was presented with the introduction of flexure bearings. Flexure bearings come in multiple forms, but the common element is the blade flexures within the bearing that allows for rotation [33]. One end of the bearing would remain fixed in a material, while the other would connect to a mating piece that would be free to rotate. Based on this principle, the flexure bearings could be positioned near the front surface of the crystal to allow for pure rotations.

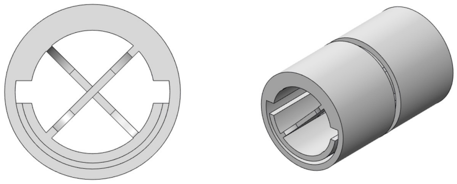

Figure 6.19: Common Cantilevered Flexure Bearing Design [33]

Most flexure bearings are fairly compact in size, with the smallest commercial sizes being close to 5 mm in height. The flexure bearings could be positioned surrounding the crystal in a cupped formation. However, due to constraints with the top crystal in the housing, a flexure bearing could not be positioned above the crystal to impart a yaw rotation. The interference of the flexure bearing and the top of the housing is illustrated in Figure 6.20.

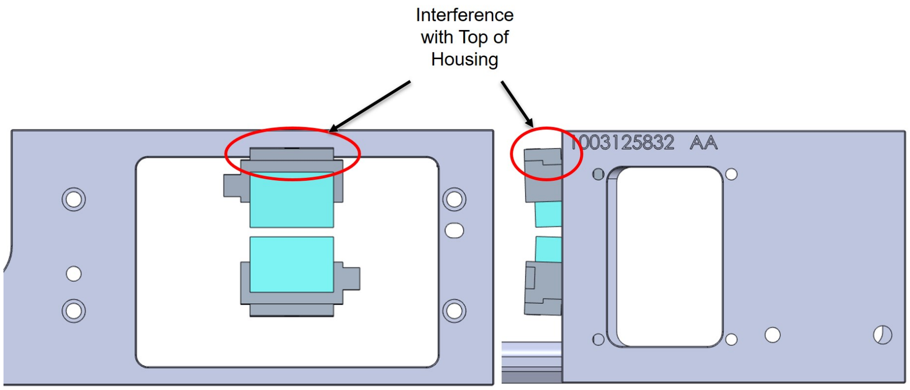

Figure 6.20: Potential Interference in the Housing for the Initial Flexure Bearing Concept

While the flexure bearings could be positioned to allow for pure pitch rotations, other options were investigated before revisiting the concept.

As an alternative to using flexure bearings to achieve pure rotations, an experimental design presented at SPIE was considered [34]. The novel design implemented the use of mating spherical and conical surfaces to allow for precise rotation of an optic about the center of the spherical surface. The moveable section of the mount has the spherical surface, which slides against the conical surface of the fixed base of the mount. As the moveable mount is actuated by fine pitch screws, the guided motion between the mating surfaces allow for precise control of the optic. The design also comes with a robust locking mechanism, that allows for the entire mount to be rigid, rather than most designs which just lock the actuation mechanism. A schematic of the design is depicted in Figure 6.21.

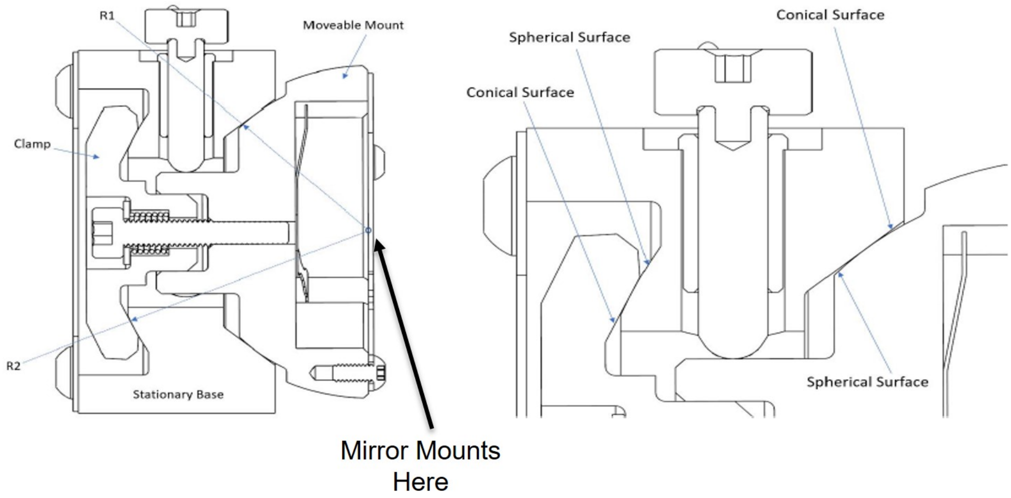

Figure 6.21: Mirror Mount Design for Pitch and Yaw Rotations [34]

In the original design, the optic was centered around the mount itself. An alternative method was proposed if the optic were to be mounted away from the center of the entire assembly as shown in Figure 6.22.

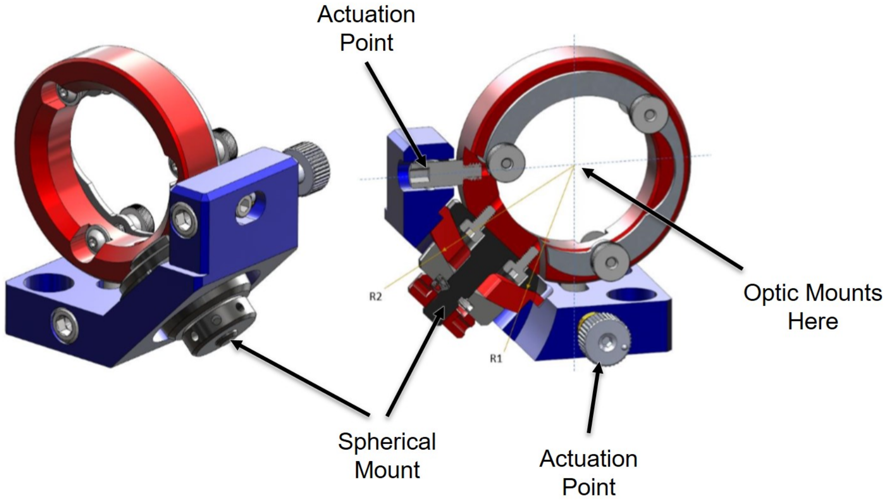

Figure 6.22: Derivative Mirror Mount Design for Offset Optic Mounting [34]

The derivative optic design would be preferred, as it serves as a more compact design in comparison to the original. In addition, the offset positioning of the optic would be more advantageous for CBI's scheme since the crystals are positioned closely together. A mock-up of the proposed solution was created to simulate a miniaturized version of the derivative design. Sizing of the components were liberally chosen, without consideration on the effects of the stiffness and dynamics of the system. However, the purpose was to merely determine if a smaller variant would be viable for the CBI system. By reducing the size and maintaining key elements, it was found that the design was unfeasible. Collisions with the ceiling of the housing or with the other crystal occurred regardless of the orientation of the design as shown in Figure 6.23.

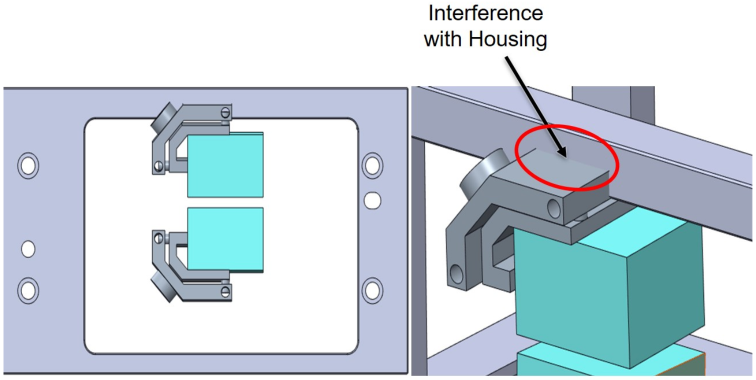

Figure 6.23: Front View of the SPIE Design in the Housing (Left), Interference with the Housing (Right)

Due to initial mockups of the design interfering with the housing, other systems were pursued instead.

6.5 Micro-goniometers and Piezoelectrics

Previously explored methods for pitch and yaw stages were unable to produce pure rotations due to interference with the housing. An optimal solution would be to use goniometers, with a fixed rotation point about the front surface of the crystal. Most commercial goniometers available are too large in volume or have a rotation point in space that is too far to reasonably position the goniometers in the housing. After a bit of investigating, an experimental product from Kohzu was found for a micro-goniometer stage. These micro-goniometers provided pitch and yaw rotations at a compact size, with a footprint of 10 by 10 mm and a height of 22 mm. These goniometers would be able to fit within the housing and be positioned behind the crystals. Figure 6.24 shows that these goniometers would interfere with the flexure mounted on the roof of the housing.

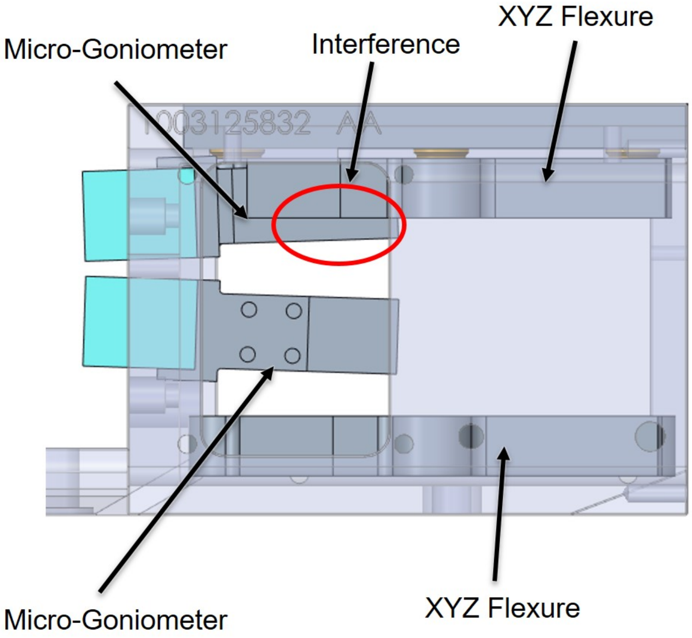

Figure 6.24: Goniometer and Flexure Interference

Since the goniometers were the first design to achieve pure pitch and yaw rotations for the system, other methods were considered for principle translations.

For a compact method that would allow for planar translations piezoelectrics were revisited. The small packaging volume common in piezoelectrics could be leveraged to allow for greater freedom in packaging a pitch and yaw stage. Initially, piezoelectrics posed too much of a risk due to being an expensive option and the possibility of being damaged per each experiment. However, the CBI team was willing to entertain the option if a more economic solution could be found. After further research, a cheap 1-D piezoelectric stage was found that is manufactured by NewScale Technologies [35]. The stage was capable of translating 6 mm with a resolution of 0.5 μm and maintained its position once power was removed. The stages had a built-in controller for each of the stages, which was both an advantage and disadvantage of the stage. In comparison to the large initial cost of purchasing an independent controller, the overall cost could quickly accumulate if the stages were prone to damage. While in terms of overall performance the stage fell short compared to the nanometer resolution other manufacturers can provide, the resolution and travel were more than sufficient for the stage requirements. These stages could be stacked and configured to allow for principle translations in 3 different directions as shown in Figure 6.25.

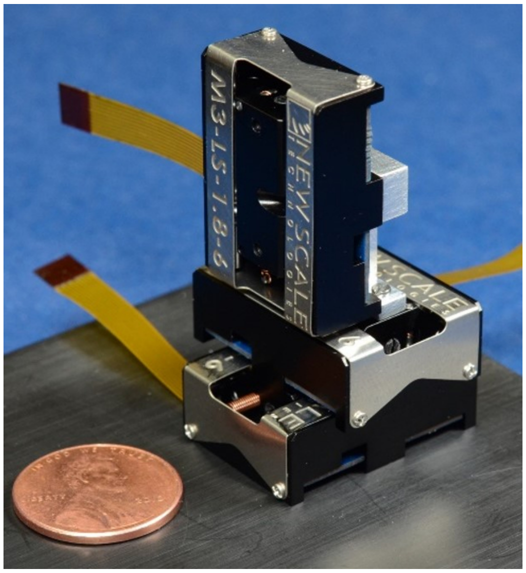

Figure 6.25: Stacked Piezoelectric Stages for 3 Principle Translations [35]

Due to the dimensions of the stage, adding vertical travel would be difficult because of the vertical housing constraint for the system. A similar method could be used as the flexure stages, by using a plate with a restoring element to raise and lower the piezoelectrics. Implementing the piezoelectric stages with the micro-goniometers, both components easily fit within the housing shown in Figure 6.26.

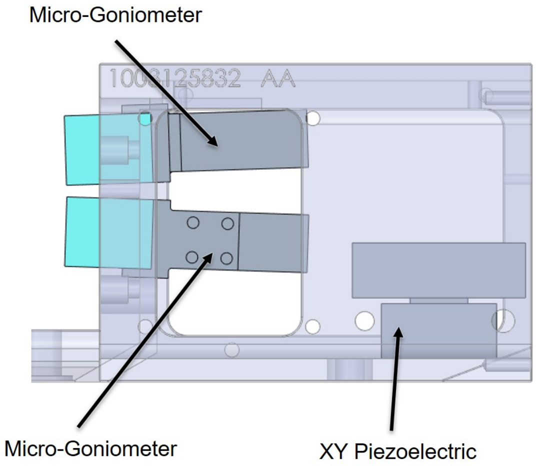

Figure 6.26: Piezoelectric Implementation in Housing

While the piezoelectrics and goniometers fit in the housing comfortably, modifications would be necessary with the goniometers. The rotation point for the goniometers was projected 15 mm in space, which matched the exact depth of the crystals. To allow for pure rotations, the rotation point would have to be increased by a few millimeters to allow for a mounting interface between the goniometer and the crystal. After some correspondence with the manufacturer, modifications could not be performed since the parts were produced at a low volume. In addition, after further discussion with the manufacturer the resolution of the product listed a repeatable accuracy of 0.1°, which was lower than the desired resolution for the rotation stages. Therefore, the team moved on from the micro-goniometers which have since been discontinued for purchase from Kohzu.

An area of concern was identified with the use of the piezoelectrics as well. In the provided datasheets, the stages have a moveable mass limit of 20 grams. Considering that the stage itself has a mass of 8.4 grams, this limits the remaining components to a mass of 11.6 grams before one of the piezoelectrics is unable to translate. Considering that the crystal itself has a mass of approximately 7.5 grams, a pitch-yaw stage and connecting components would be limited to less than 4.1 grams. While other piezoelectric manufacturers are capable of translating higher masses, they were found to be too expensive and risky to pursue. As a result, piezoelectrics were no longer considered a viable solution for crystal alignment.

At this point the total system had reverted back to the planar X-Y flexure stage with the vertical capabilities if needed. A solution for the pitch-yaw rotational motions continued to be investigated.

6.6 Requirement Changes

At this point the CBI team considered softening some of the requirements for the project. After several trials, it was clear that trying to implement pure rotations was difficult with the current housing scheme. As such, the volume of the housing was increased to be more accommodating for rotation elements for the top crystal. After checking some of the clearance tolerances for the diagnostics, it was found that the roof of the housing could be increased by 10 mm, and the floor of the housing lowered by 5 mm. This provides an overall addition of 15 mm to the overall housing, resulting in a roof to floor height of 60 mm and is documented in Figure 6.27.

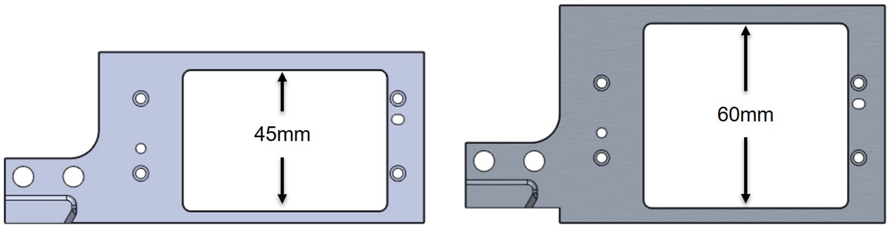

Figure 6.27: 2nd Iteration Housing (Left), 3rd Iteration Housing (Right)

With the increase in overall height for the housing, consideration was given to flexure bearings and goniometers again for the possibility of pure rotations. Some of the smaller goniometers commercially available, (25 by 25 mm stage size) would be able to fit within the housing. However, issues remained with packaging if similar crystal Bragg angles were utilized. To allow for pure rotations, the goniometers would need to be positioned above one another. Due to the crystals being separated at the closest edge by 2 mm, the goniometers would most likely interfere with one another. In addition, issues remained with accuracy as most mechanically driven goniometers on the market only have an accuracy of close to 0.2°, far larger than the requirements for crystal alignment. To test the feasibility of the flexure bearings, a hand calculation was performed to determine if the desired resolution could be met. It was assumed a moment arm could be extended from the flexure bearing to rotate the crystal. Setting the desired rotation to 0.01° and the assumed horizontal displacement to match a 1/16 turn of a 100 thread per inch screw (15.9 μm), the required moment arm was calculated.

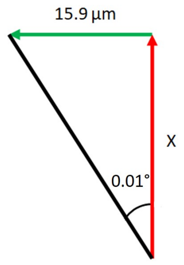

Figure 6.28: Trigonometric Relation to Determine Required Moment Arm

With these assumptions, the required moment arm would be a minimum of 90 mm in length. This length requirement was much larger than the adjusted volume constraints. Pure rotation flexure elements were considered as well. However, concerns arose with the overall stability and control of the proposed solutions. The CBI team believed that the overall development time would be too great to overcome and other solutions were pursued instead.

After further discussion with the CBI team, it was decided to remove the restriction of pure rotations for the crystals. The team felt that enough designs were considered and that a pure rotation scheme would not be easily achieved. While further design development may have revealed a solution capable of pure rotations with the desired resolution, a design with cross-coupled movements was pursued instead. This opened up more options for the pitch and yaw stage that may have been previously eliminated earlier.

After additional research, a pitch-yaw stage was found with precise travel. The concept was initially found in a patent search that was submitted through a company known as Siskiyou [36]. The company specialized in designing optomechanical stages and patented one of their technologies to allow for precise travel. For their pitch and yaw stages, they implemented flexure hinges that allow for rotations around the axis of the hinge. To achieve a fine resolution, a unique actuation system is used as seen in Figure 6.29. For the adjustment mechanism, a fine-pitch screw pushes against a rod with a spherical ball end. The ball end is guided between a set of rails that creates a prying action to move the hinge apart. Depending on the relative angle of the rails, higher resolution could be achieved at the cost of a larger rotation range.

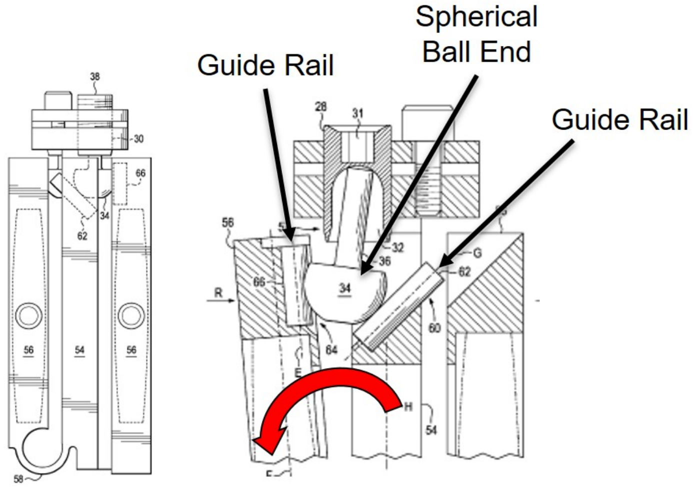

Figure 6.29: Siskiyou Block Adjustment Mechanisms [36]

After investigating further, it was found that Siskiyou sells many optomechanical stages besides their pitch-yaw flexures. This includes an extremely compact one directional translation stage. After contacting the manufacturer, it was found that the stage could be repurposed to serve as a vertical stage as well. The stages have a compact footprint of 15.75 by 15.75 mm and an overall height of less than 10 mm. The stage was implemented in the housing along with the flexure stage to assess its packaging viability.

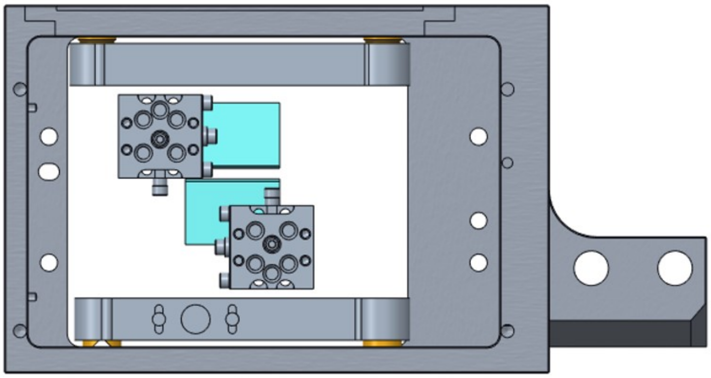

Figure 6.30: Vertical Travel Stages Implemented with Flexure Design

The flexure stage combined with the Siskiyou vertical stage would allow for the three principle translations. This would eliminate the need for the kinematic mounts and restoring spring elements for the flexures. This would also circumvent the cross-coupled motion between the vertical travel, pitch and roll. Along with the pitch-yaw flexure stage, all five degrees of freedom would be achieved. However, after a bit of deliberation it was decided to move forward without the flexure stages. The time required to verify that they were consistent enough for the travel requirements and the overall cost for a custom flexure was too much to overcome. At a cost of overall height but a gain in smaller footprint, the one-directional Siskiyou stages could be stacked together to provide X-Y translation. This leads to the current design proposed for the alignment of the two crystals in the CBI diagnostic.

6.7 Final Design

The final design borrowed the pallet concept from the initial flexure design. It was chosen to allow for easy mounting of all components before being placed in the housing. The pallet has a raised platform for the X-Y translation stages to mount to. To locate the X-Y stages, raised L-bracket segments were implemented for consistent mounting as shown in Figure 6.31.

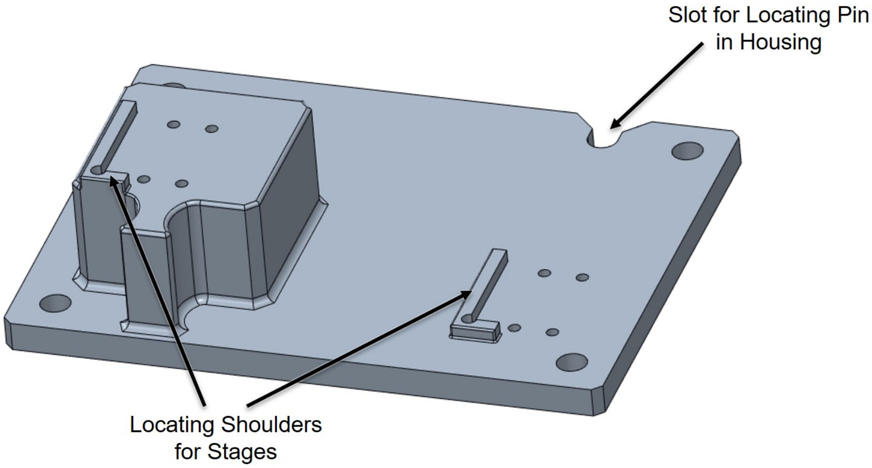

Figure 6.31: Pallet Design for Stages and Housing

To ensure consistent placement within the housing, locating pins were installed to protrude from the floor. A slot with a rounded groove is implemented in the pallet to prevent side to side translation. The pallet is butted up against another pin to fully locate the pallet assembly. The pallet can then be secured into the housing as illustrated in Figure 6.32.

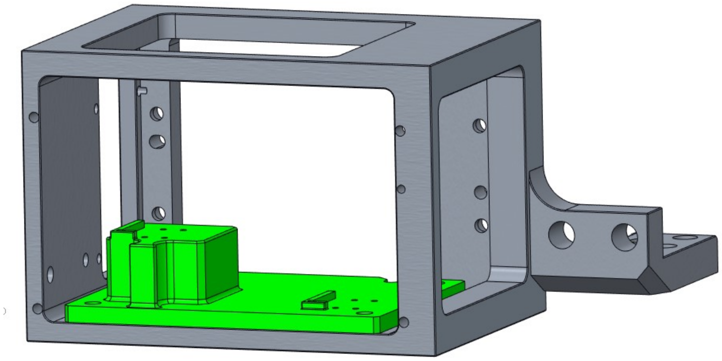

Figure 6.32: Pallet Implementation Within the Housing

For control of the X-Y translations, stages from Siskiyou corporation were selected. These stages allow for ± 1.5 mm of controllable motion by using a dovetail mechanism and are driven by 100 thread per inch screws [37]. The stage comes with a locking set screw to prevent any undesired motion. While these stages only meet the minimum precision requirements, the stages are extremely compact. This allowed for more options to be considered for the other translation stages. These stages are stacked on top of each other to allow for planar translations as shown in Figure 6.33.

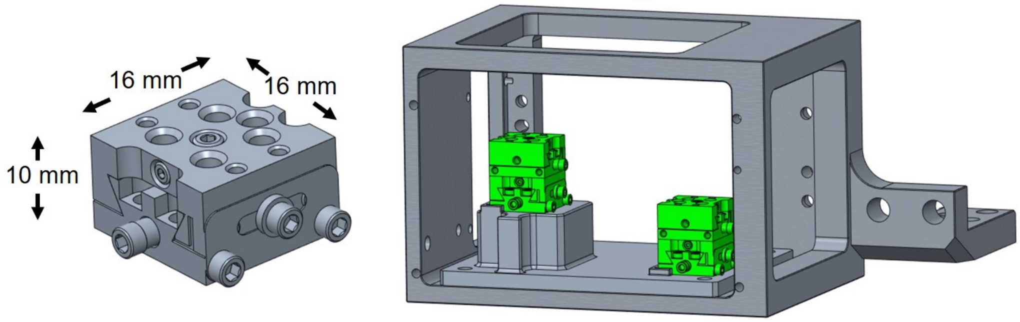

Figure 6.33: Siskiyou X-Y Stages (Left) [37]**, Stages Implemented in the Housing (Right)**

To connect to the vertical travel stage, custom brackets were required. These are simple L-brackets to position the vertical stages to approximately the midway point between the considered crystal Bragg angles (85.5°-88°). The positions were slightly offset from the midpoint for both brackets to prevent vertical overlap between the stages. The implementation into the housing is shown in Figure 6.34.

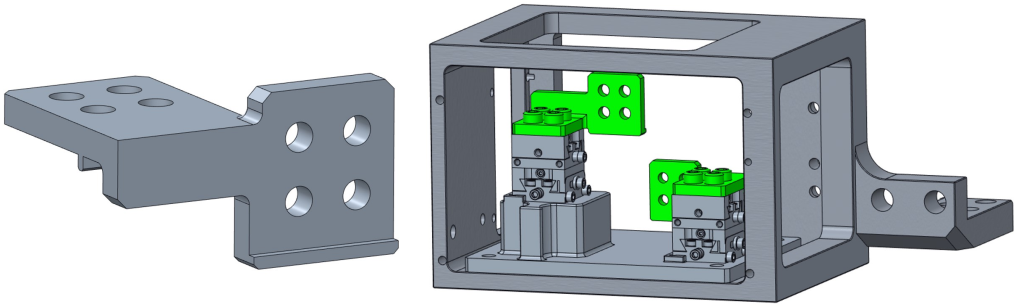

Figure 6.34: Custom Brackets to Attach to Vertical Stage (Left), Brackets Implemented in the Housing (Right)

For the vertical travel, the same Siskiyou stages were implemented as illustrated in Figure 6.35. Due to being loaded vertically, the stages were positioned “backwards”, with the standard moveable stage being attached to the custom bracket. This was recommended from the manufacturer, as this would enable a more stable configuration to support the remaining components.

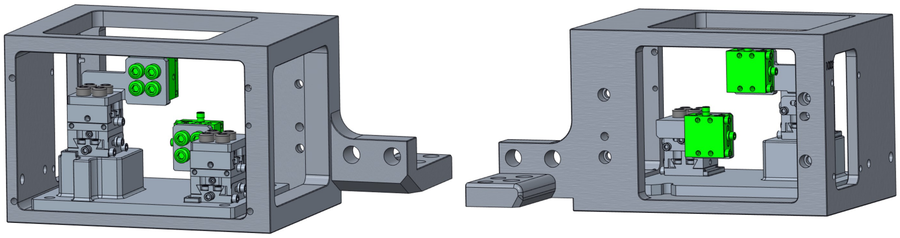

Figure 6.35: Vertical Stages Implemented in the Housing, Back View (Left), Front View (Right)

To handle the coarse adjustment of the system, it was decided to use custom brackets to connect to the pitch-yaw mechanism. While this method would not be as robust as other proposed coarse adjustment mechanisms, it was chosen deliberately by the team. This method would be more user friendly, as the same brackets could be used for repeated Bragg angle crystals. In Figure 6.36, examples of the described coarse adjustment brackets are shown.

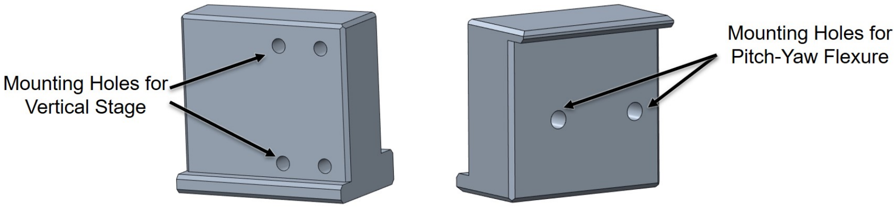

Figure 6.36: Top and Bottom Pitch-Yaw Connecting Brackets

For the pitch-yaw mechanism, a commercial flexure product from Siskiyou was initially selected. The flexure hinge mechanism with their adjustment block technology allows for highly precise and controllable motion. There was some concern from stakeholders at the NIF with regards to potential collisions, if the typical commercial solution was used. Siskiyou was contacted directly to determine if a miniaturized version existed. From a previous custom design, a smaller pitch-yaw flexure was available that was more compact in size. These stages connect to the bracket that each crystal is adhered to and is shown on the right of Figure 6.37. With this implementation, all 5 degrees of freedom can be adjusted for the system.

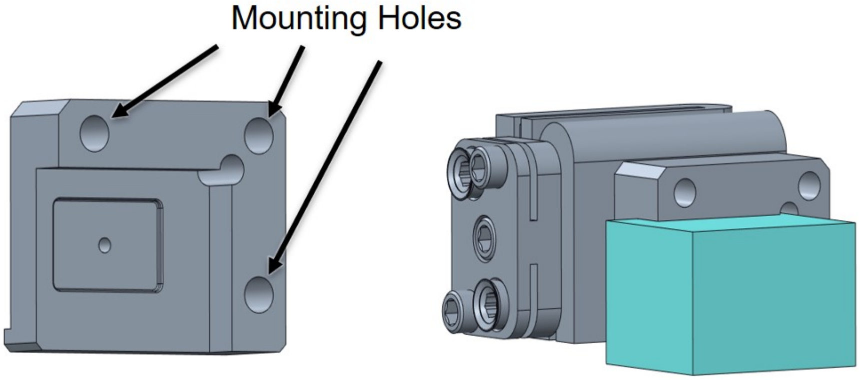

Figure 6.37: Crystal Bracket (Left), Implemented with Siskiyou Pitch-Yaw Mechanism (Right)

For future experiments, potential configurations were considered to determine the packaging of the system. The Bragg angles for each configuration were collected in Table 6.1.

Table 6.1: Crystal Configurations Considered for Design

Configuration	Top Crystal Bragg Angle	Bottom Crystal Bragg Angle
A	85.49°	85.49°
B	87.53°	85.49°

The crystal positions for each configuration in the housing is illustrated in Figure 6.38. Depending on the crystals that are used for an experiment, the only changed element would be the mounting brackets that connect to the pitch-yaw flexure. Under ideal conditions, the mounting brackets would locate the crystal exactly. With machining tolerance stack-up, the crystal location would vary slightly. Without actuating any of the stages, the crystals are predicted to be located only a few hundred microns from their correct location.

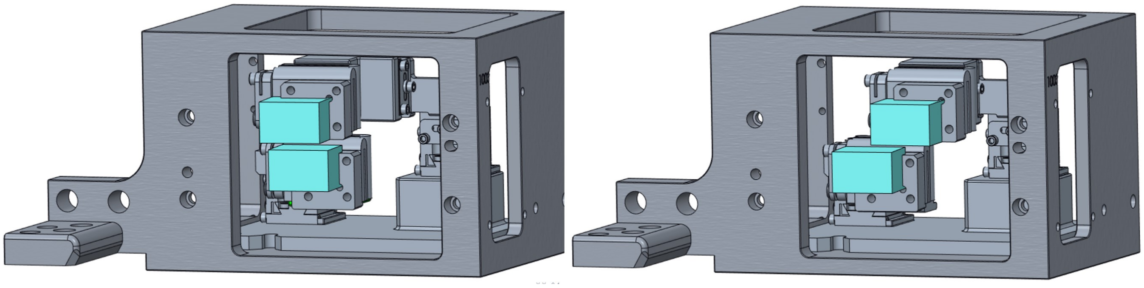

Figure 6.38: Configuration A (Left), Configuration B (Right)

6.7.1 Adjustment Points

Consistent with the requirements set at the beginning of the project, the design ensured that all stages could be actuated from the left side, top and back of the housing. The flexure stages and the X-translation stage could be actuated from the side of the housing as shown in Figure 6.39.

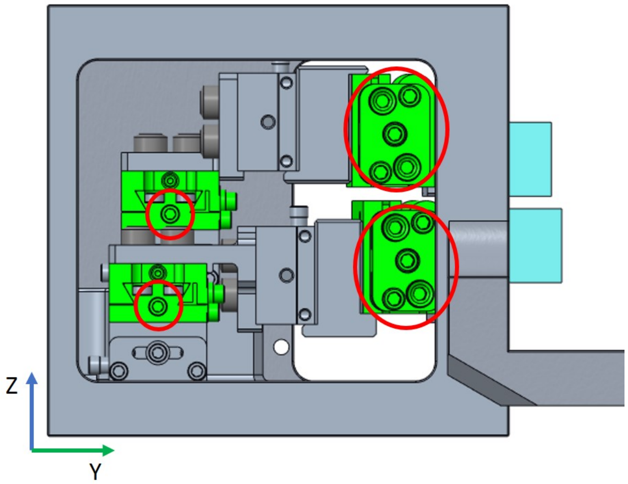

Figure 6.39: Side Access Point for Stages

The vertical stages would be adjusted from the top. It was ensured that even with the maximum considered horizontal (X) travel there would be enough clearance to adjust both vertical stages. Figure 6.40 shows the adjustable region for the vertical stages enclosed by the red ovals.

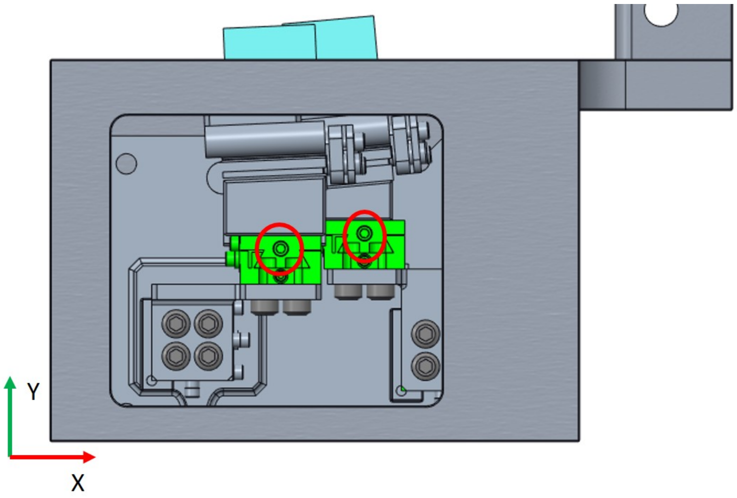

Figure 6.40: Top Access Point for Stages

Finally, the last planar translation stage (Y) could be actuated from the back of the housing as depicted in Figure 6.41.

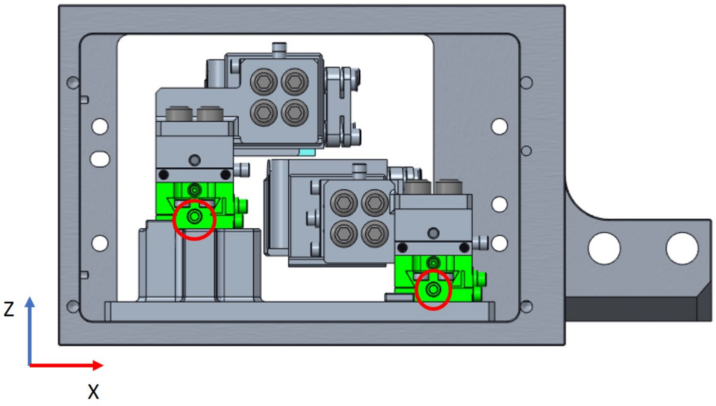

Figure 6.41: Back Access Point for Stages

The locking mechanisms for each of the planar stages could be reached from the accessible parts of the housing as well.

6.7.2 Design Overview

A collection of the relevant attributes of the proposed design are found in Table 6.2.

Table 6.2: Stage Precision and Travel Capabilities

Item	Mode of Travel	Travel Range	Precision
Siskiyou 37.12dt Stage	X-Y-Z Translation	± 1.5 mm	254 μm/rev
Custom Siskiyou Pitch-Yaw Flexure	X + Z Rotation (Pitch + Yaw)	± 3°	0.003°

Based on the requirements set at the beginning of this project, the proposed design was capable of meeting each of the hard requirements set. The combination of stages allows for complete 5 degrees of freedom control over the crystals. Based on the given configurations, the design was capable of accommodating two different crystal location sets. The resolution for the principle translations met the same direct drive resolution as the previously used Thorlabs stage. In terms of the rotation, the proposed design improves upon the resolution greatly, allowing for a more precise motion when aligning the crystals. The desired access points to the stage were maintained, with adjustment mechanisms easily accessible from the back, side and top of the housing. Finally, both the translation and rotation stages come with a locking mechanism to be insensitive to errant acceleration loads. In terms of the soft requirements set, the proposed design was incapable of meeting a few of these. The height of the housing needed to be increased to accommodate for systems to manipulate the top crystal. In addition, cross-coupled movements carried over from the previous stage to the proposed design. However, the goal of having both crystals capable of movements independent of one another was achieved. Both stages also have grease applied on mated sliding surfaces to minimize potential issues with stiction. Testing and prolonged used would be required to determine if the issues with stiction were truly minimized. Overall, the newly proposed design was able to meet a majority of the requirements set for the project, but further iterations and review may allow for all requirements to be met in the future.

Chapter 7

CONCLUSIONS AND FUTURE WORK

The primary goal of this project was to develop a design solution that would upgrade the current capabilities of the CBI diagnostic. This goal was achieved by proposing a solution that would allow for independent control in 5 degrees of freedom of two crystals. However, further improvements could be made with modified requirements or design choices for a future system. This chapter outlines potential avenues that the current system can evolve into as well as recommendations to improve the current design.

7.1 Testing of Proposed Design

One of the original outcomes for this thesis was to test the proposed design solution. A series of tests could be performed on the stock linear translation stages, before the custom pitch-yaw flexures are ordered. Due to the visual feedback that the PSM provides during alignment, the stability of the stages would be the most important aspect to test. This is to ensure that once the crystals have been aligned, the stages would be capable of maintaining their position. Two different testing methods can be used to determine the angular and positional stability of the stages. For the angular stability, a mirror can be mounted to the stages set up in a three principle translation scheme. An autocollimator (an optical device used for measuring angles), can be used to determine if the series of stages will rotate while being adjusted. For the positional stability, a similar setup can be utilized with the stages setup to allow for the three principle translations. A tooling ball would be mounted to the vertical travel stage and aligned at a set location. A coordinate measuring machine (CMM) would then measure the location of the tooling ball. The stages and tooling ball can then be perturbed, and the position of the tooling ball can be remeasured. Based on the difference in measurements, this can report on the positional stability of the stages. Furthermore, tests could be performed to see if the stages drift over time, by aligning the stages and leaving them for a few days before remeasuring their position.

Overall responsiveness of the stages would be tested as well. Characterizing the motion of the stages to allow for the actuation of the stages to be predictable and known before an experiment is desired. This would allow the overall alignment period to be more efficient to avoid wasting time aligning the stages. These aspects would also contribute to the ease of use for an operator and could be tested along with the methods outlined previously.

Once a complete set of stages are available, a thorough test can be performed in aligning the crystals with the new offline alignment process. Testing would simulate the entire procedure of installing each of the stages and aligning them relative to the PSM. Ideally, interviews with the operators would be performed to receive feedback on the design for future improvements on user responsiveness and comfort.

7.2 Positioning and Alignment Analysis

An additional analysis that could be performed would be the creation of a simulation to predict and cancel the cross-coupled motion. Since the linear translation stages theoretically do not produce any rotational movement, it would be possible to determine the translations necessary to cancel out the cross-coupled movements produced from the pitch-yaw flexure. The program would use reference coordinate frames to determine how the center of the crystal translates and rotates when the pitch-yaw flexure is actuated. Based on this movement, the required translations from the other stages could be found to essentially generate a pure rotation. With this simulation, it can assist operators to develop intuition on how the translation stages should be actuated to cancel the cross-coupled movements.

7.3 Debris Wind Analysis Improvements

After the completed analyses, it was clear that a redesign would be necessary for both the nose-cap and the retaining cover. Both components failed through the thickness consistently at their thinner regions. To mitigate this risk, future redesigns could implement more material on the center bar and at the bolt hole connections for the retaining cover. In addition, if the upper and lower chamfers on the nose-cap were less steep, this would add more material on the thinner sections while also reducing the “view factor” of these surfaces. This would lead to a reduction in the anticipated stresses and may allow for the nose-cap to be used on multiple shots. From the analysis performed, the depth of the cutout in the back of the housing was varied to accommodate for different polycarbonate thicknesses. Future analysis could be performed to determine the required depth of cut for the part to not yield through the thickness on the upper and lower sections of the nose-cap. Future modifications to the nose-cap will need to accommodate for the height change of the housing as well.

With the current model, it was observed that the polycarbonate shields would translate at late stages in time. This translation would be undesirable in the physical assembly, so the components would need to be redesigned. The polycarbonate, tantalum and retaining cover assembly could implement pins to secure the assembly in place. In addition, rather than using separate polycarbonate shields for both windows, a singular, continuous piece of polycarbonate and tantalum could be used. This would improve the overall stiffness of the assembly, and would prevent large translations since the components would be seated in the cutout of the nose-cap.

The model could be further refined by modeling the preload applied at each of the bolt-hole locations. With this change, the results for the connected surfaces between the retaining cover and nose-cap may be more representative of the actual system.

7.4 Custom Flexure for Pure Rotations

One aspect of the design that could be improved upon would be to design a custom flexure for pure rotations about the crystal surface. With the relaxation on the volume constraints on the crystal housing, it may be possible to design a custom flexure to allow for pure rotations. With clever enough design, flexures can be implemented in tight packaging scenarios that common optomechanical systems are unable to operate in. Due to time-constraints, limited resources and inexperience in flexure design, a flexure to address this need was unable to be generated by the author. A custom flexure could be contracted to a manufacturer with more experience or the CBI team could invest more development time designing a custom flexure. Both options can be considered if a need for pure rotations arises in the future.

7.5 3-Crystal CBI

One of the natural progressions from this project would be the addition of another crystal. Currently, the newly designed system is close to the maximum limits in terms of packaging with the current housing. As a result, much of the hardware used in this system would have to be redesigned. Realistically, smaller crystals would need to be ordered to reasonably fit within the new CBI housing. This would allow for the packaging of a 3rd crystal into the housing. Piezoelectrics may be an attractive solution for a 3-crystal system due to their small packaging. Before the piezoelectrics are deployed, several tests would have to be performed to ensure the stages could be used for multiple experiments. A 3-crystal system may be achievable by softening some of the requirements used to develop the current stage. An example of this would be to eliminate the need for all 3 crystals to be actuated independently. Instead, if a robust aligning system were created, all 3 crystals could be mounted on one bracket at fixed locations relative to one another. As such, one 5 DOF stage would be required to align all three crystals.

The design proposed in this thesis is one of many possible solutions to the design challenge presented. After further testing is performed, specific areas of the design will be modified and improved upon to create a robust system that can be used for any experiment the dual crystal CBI diagnostic is needed for.

BIBLIOGRAPHY

[1] “History of fusion energy research.” Encyclopedia Britannica. https://www.britannica.com/science/nuclear-fusion, 2019. (Accessed April 29, 2020).

[2] “Fusion and Ignition.” Lasers.LLNL. https://lasers.llnl.gov/science/ignition. (Accessed April 29, 2020).

[3] “Operators inside the NIF Target Chamber.” Boston. http://archive.boston.com/bigpicture/2010/10/the_national_ignition_facility.html. (Accessed April 29, 2020).

[4] “How NIF Works.” Lasers.LLNL. https://lasers.llnl.gov/about/how-nif-works. (Accessed April 29, 2020).

[5] “Gold Rugby Hohlraum.” Lasers.LLNL. https://lasers.llnl.gov/news/rugby-hohlraum-kicks-up-nif-energy-efficiency, 2019. (Accessed April 30, 2020).

[6] “Manufactured Hohlraum.” Photonics Media. https://www.photonics.com/Articles/NIF_Achieves_Historic_Laser_Shot/a40883, 2010. (Accessed April 30, 2020).

[7] “ICF Process.” University of York. https://www.york.ac.uk/physics/ypi/research/laser/icf/inertialconfinementfusionresearch/. (Accessed May 1, 2020).

[8] “About OMEGA EP.” Laboratory for Laser Energetics. http://www.lle.rochester.edu/omega_facility/omega_ep/, 2019. (Accessed May 1, 2020).

[9] A. Bullock, O. Landen, and D. Bradley, "10 (micro) m and 5 (micro) m pinhole-assisted point-projection backlit imaging for nif," tech. rep., Lawrence Livermore National Lab., 2001.

[10] G. Hall, "The Crystal Backlighter Imager: A Spherically-Bent Crystal Imager for Radiography on the NIF," 2017. [Powerpoint Presentation], (Accessed May 4, 2020).

[11] G. Hall, C. Krauland, M. Schollmeier, G. Kemp, J. Buscho, R. Hibbard, N. Thompson, E. Casco, M. Ayers, S. Ayers, *et al.*, "The crystal backlighter imager: A spherically bent crystal imager for radiography on the national ignition facility," *Review of Scientific Instruments*, vol. 90, no. 1, p. 013702, 2019.

[12] "Bragg's Law." HyperPhysics. http://hyperphysics.phy-astr.gsu.edu/hbase/quantum/bragg.html. (Accessed May 1, 2020).

[13] "Compact 5-Axis Pitch, Yaw, and Translation Stage." Thorlabs. https://www.thorlabs.com/newgrouppage9.cfm?objectgroup_id=7850. (Accessed May 2, 2020).

[14] A. Jiang and B. Guo, "Analysis of stray light reflected from multi-beam laser focusing surface," in *Pacific Rim Laser Damage 2019: Optical Materials for High-Power Lasers*, vol. 11063, p. 110630M, International Society for Optics and Photonics, 2019.

[15] N. Masters, A. Fisher, D. Kalantar, R. Prasad, J. Stölken, and C. Wlodarczyk, "Evaluation of observed blast loading effects on nif x-ray diagnostic collimators," *Review of Scientific Instruments*, vol. 85, no. 11, p. 11D628, 2014.

[16] “Metrics for Tetrahedral Elements.” Sandia Laboratory. https://cubit.sandia.gov/public/13.2/help_manual/WebHelp/mesh_generation/mesh_quality_assessment/tetrahedral_metrics.htm. (Accessed May 6, 2020).

[17] D. Collins, “What are recirculating linear bearings?.” Linear Motion Tips. https://www.linearmotiontips.com/faq-what-are-recirculating-linear-bearings/, 2017. (Accessed May 4, 2020).

[18] “Single-Axis Miniature Dovetail Translation Stage.” Thorlabs. https://www.thorlabs.com/newgrouppage9.cfm?objectgroup_id=2952. (Accessed May 4, 2020).

[19] “DT-100 Series Stages.” Siskiyou. https://www.siskiyou.com/dt-100-series.html. (Accessed May 4, 2020).

[20] “Goniometer Stages.” Thorlabs. https://www.thorlabs.com/newgrouppage9.cfm?objectgroup_ID=860. (Accessed May 4, 2020).

[21] J. B. Hopkins, *Design of flexure-based motion stages for mechatronic systems via freedom, actuation and constraint topologies (FACT)*. PhD thesis, Massachusetts Institute of Technology, 2010.

[22] “Laser cut living hinges for neater designs.” DesignSpark. https://www.rs-online.com/designspark/laser-cut-living-hinges-for-neater-designs, 2016. (Accessed May 5, 2020).

[23] “Dynarex Nail Clippers.” Quickmedical. https://www.quickmedical.com/dynarex-nail-clippers.html. (Accessed May 5, 2020).

[24] J. McMahon, “Basic piezo technologies for motion control applications.” Control Engineering. https://www.controleng.com/articles/basic-piezo-technologies-for-motion-control-applications/, 2010. (Accessed May 5, 2020).

[25] “Single-module parallel-kinematics X and Y (with crosstalk compensation).” Physikinstrumente. http://www.piezostage.net/. (Accessed May 5, 2020).

[26] “Perpendicular Dovetail Rail Carrier.” Thorlabs. https://www.thorlabs.com/newgrouppage9.cfm?objectgroup_id=8295. (Accessed May 8, 2020).

[27] “1/2” (13 mm) Travel Vertical Translation Stage.” Thorlabs. https://www.thorlabs.com/newgrouppage9.cfm?objectgroup_id=5088. (Accessed May 8, 2020).

[28] “Vertical Linear Stage, Dovetail, 0.12 in. Travel, 0.98 x 0.98 in. Platform.” Newport. https://www.newport.com/p/DS25-Z. (Accessed May 8, 2020).

[29] Y.-S. Kim, J.-M. Yoo, S. H. Yang, Y.-M. Choi, N. G. Dagalakis, and S. K. Gupta, “Design, fabrication and testing of a serial kinematic mems xy stage for multifinger manipulation,” *Journal of Micromechanics and Microengineering*, vol. 22, no. 8, p. 085029, 2012.

[30] Q. Xu, “Design and development of a compact flexure-based xy precision positioning system with centimeter range,” *IEEE Transactions on Industrial Electronics*, vol. 61, no. 2, pp. 893–903, 2013.

[31] S. Awtar, *Synthesis and analysis of parallel kinematic XY flexure mechanisms.* PhD thesis, Massachusetts Institute of Technology, 2003.

[32] "Standard and Precision Carbide Pads." Newport. https://www.newport.com/f/carbide-pads. (Accessed May 8, 2020).

[33] "Cantilevered Pivot Bearings Solid Model." Riverhawk Flex Pivots. http://flexpivots.com/flexural-pivot-custom-engineering/solid-model-downloads/. (Accessed May 8, 2020).

[34] F. A. DeWitt, "A novel mirror-mount design suitable for laboratory and oem applications," in *Optical System Alignment, Tolerancing, and Verification XII*, vol. 10747, p. 107470D, International Society for Optics and Photonics, 2018.

[35] "M3-LS-1.8-6 Linear Micro Stage." New Scale Technologies. https://www.newscaletech.com/micro-motion-modules/m3-ls-linear-smart-stages/#. (Accessed May 9, 2020).

[36] R. B. Hodge, "Positioning apparatus," 2015. United States Patent 8,925.409 B2, Jan. 6, 2015.

[37] "37.12dt Series Stage." Siskiyou. https://www.siskiyou.com/37-12dt-series-stage.html. (Accessed May 9, 2020).

[38] W. C. Young, R. G. Budynas, A. M. Sadegh, *et al.*, *Roark's formulas for stress and strain*, vol. 7. McGraw-Hill New York, 2002.

APPENDICES

Appendix A

RAY TRACING: TARGET WINDOW DIMENSIONS AND CLOSEST RAY TO TARGET

The following spreadsheet is the collection of measurements taken for the cases described in Chapter 2. The required target window size to maintain the 0.6 by 0.6 mm FOV requirement and the closest reflected ray distance to the target is documented below.

All measurements ± 0.01mm (+ 0.01mm to ensure 300 µm FOV)

🟩 **Area Reduction/Enough Clearance**

🟨 **Slight Area Increase/Slight Modification to Shield for Clearance**

🟥 **Major Area Increase/Interferes or Close Passing to Paddles**

	Top and Bottom Crystal Bragg Angle = 88					
	Target Window Dims				Closest Ray Measurements	
Sensor	Height (mm)	Width (mm)	Area (mm^2)	Percent Change (%)	Top Ray (mm)	Bottom Ray (mm)
HSLOS RIGHT	0.96	0.66	0.63	🟩 -1	🟥 6.52	🟥 6.52
HSLOS LEFT	0.96	0.66	0.63	🟩 -1	🟥 6.5	🟥 6.54
SLOS	0.96	0.66	0.63	🟩 -1	🟥 6.48	🟥 6.54
HGX RIGHT	0.96	0.66	0.63	🟩 -1	🟥 6.75	🟥 6.77
HGX LEFT	0.96	0.66	0.63	🟩 -1	🟥 6.75	🟥 6.77

	Top Crystal Bragg Angle = 88 , Bottom Crystal Bragg Angle = 87					
	Target Window Dims				Closest Ray Measurements	
Sensor	Height (mm)	Width (mm)	Area (mm^2)	Percent Change (%)	Top Ray (mm)	Bottom Ray (mm)
HSLOS RIGHT	0.96	0.8	0.77	🟨 20	🟥 6.5	🟩 11.72
HSLOS LEFT	0.96	0.79	0.76	🟨 18.5	🟥 6.5	🟩 11.74
SLOS	0.96	0.79	0.76	🟨 18.5	🟥 6.48	🟩 11.74
HGX RIGHT	0.96	0.79	0.76	🟨 18.5	🟥 6.75	🟩 11.87
HGX LEFT	0.96	0.79	0.76	🟨 18.5	🟥 6.75	🟩 11.86

	Top Crystal Bragg Angle = 88 , Bottom Crystal Bragg Angle = 86					
	Target Window Dims				Closest Ray Measurements	
Sensor	Height (mm)	Width (mm)	Area (mm^2)	Percent Change (%)	Top Ray (mm)	Bottom Ray (mm)
HSLOS RIGHT	0.96	0.9	0.86	🟥 35	🟥 6.72	🟩 17.05
HSLOS LEFT	0.96	0.91	0.87	🟥 36.5	🟥 6.49	🟩 16.8
SLOS	0.96	0.91	0.87	🟥 36.5	🟥 6.47	🟩 16.81
HGX RIGHT	0.96	0.9	0.86	🟥 35	🟥 6.75	🟩 16.92
HGX LEFT	0.96	0.9	0.86	🟥 35	🟥 6.75	🟩 16.92
SLOS ALIGNED	0.96	0.72	0.69	🟨 8	🟥 6	🟥 6.34

	Top and Bottom Crystal Bragg Angle = 87.53					
	Target Window Dims				Closest Ray Measurements	
Sensor	Height (mm)	Width (mm)	Area (mm^2)	Percent Change (%)	Top Ray (mm)	Bottom Ray (mm)
HSLOS RIGHT	0.96	0.66	0.63	-1	9.19	9.19
HSLOS LEFT	0.96	0.66	0.63	-1	9.19	9.19
SLOS	0.96	0.66	0.63	-1	9.19	9.19
HGX RIGHT	0.96	0.66	0.63	-1	9.37	9.38
HGX LEFT	0.96	0.66	0.63	-1	9.37	9.38

	Top Crystal Bragg Angle = 87.53 , Bottom Crystal Bragg Angle = 86.53					
	Target Window Dims				Closest Ray Measurements	
Sensor	Height (mm)	Width (mm)	Area (mm^2)	Percent Change (%)	Top Ray (mm)	Bottom Ray (mm)
HSLOS RIGHT	0.96	0.78	0.75	17	9.2	14.16
HSLOS LEFT	0.96	0.78	0.75	17	9.19	14.16
SLOS	0.96	0.78	0.75	17	9.19	14.16
HGX RIGHT	0.96	0.78	0.75	17	9.37	14.28
HGX LEFT	0.96	0.78	0.75	17	9.37	14.28

	Top Crystal Bragg Angle = 87.53 , Bottom Crystal Bragg Angle = 85.53					
	Target Window Dims				Closest Ray Measurements	
Sensor	Height (mm)	Width (mm)	Area (mm^2)	Percent Change (%)	Top Ray (mm)	Bottom Ray (mm)
HSLOS RIGHT	0.96	0.9	0.86	35	9.19	19.14
HSLOS LEFT	0.96	0.9	0.86	35	9.19	19.13
SLOS	0.96	0.9	0.86	35	9.19	19.14
HGX RIGHT	0.96	0.9	0.86	35	9.36	19.23
HGX LEFT	0.96	0.9	0.86	35	9.36	19.22

	SLOS Sensors, Staggered and Aligned Orientations, Bragg Angle = 88					
	Target Window Dims				Closest Ray Measurements	
Sensor	Height (mm)	Width (mm)	Area (mm^2)	Percent Change (%)	Top Ray (mm)	Bottom Ray (mm)
SLOS STAGGERED	0.96	0.71	0.68	6.5	6.34	6.54
SLOS ALIGNED	0.96	0.72	0.69	8	6	6.34

Appendix B

ADDITIONAL DEBRIS WIND RESULTS

The following appendix contains the debris wind results not shown in Chapter 4.

1.0 MJ Results

Nose-Cap, Plastic Strain Results

1.0 MJ Energy
1 g Mass

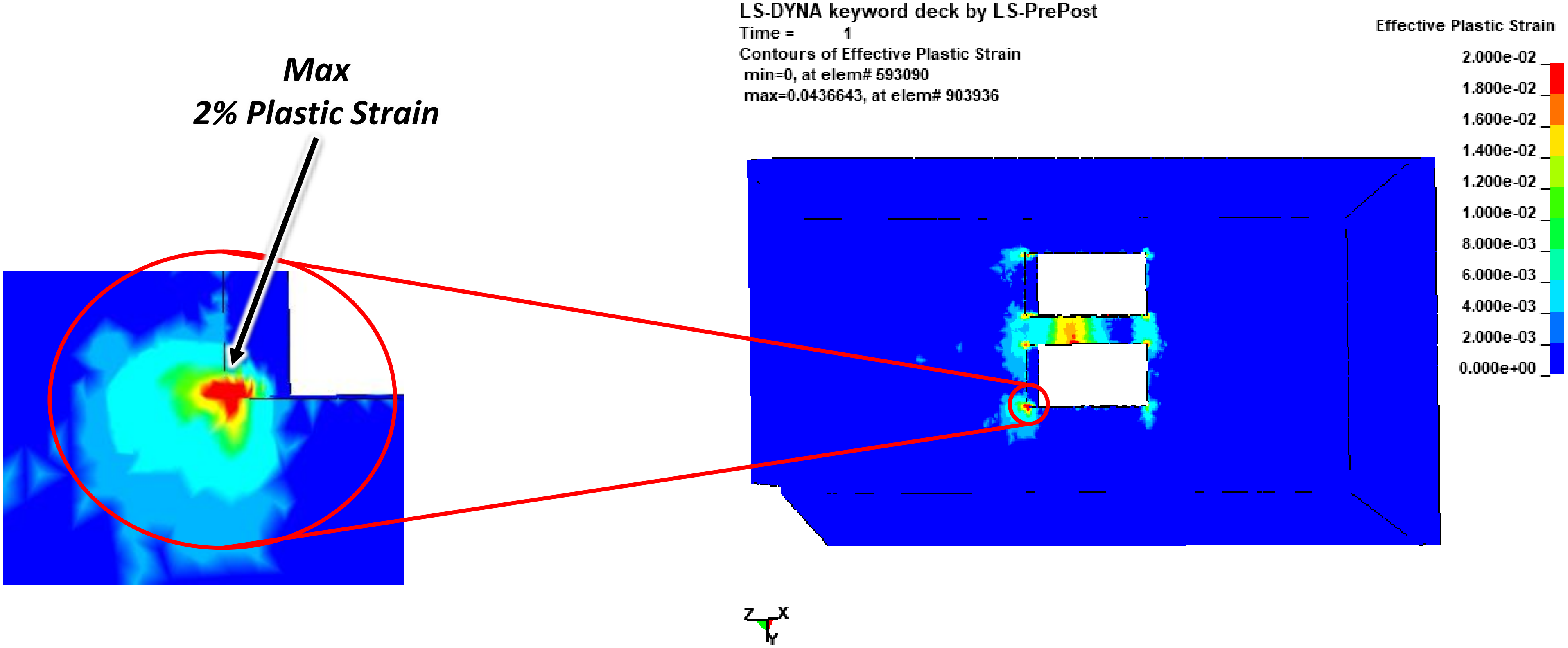

Max
2% Plastic Strain

Nose-Cap, Plastic Strain Results Cont.

1.0 MJ Energy
1 g Mass

<1%
Through Thickness
Plastic Strain

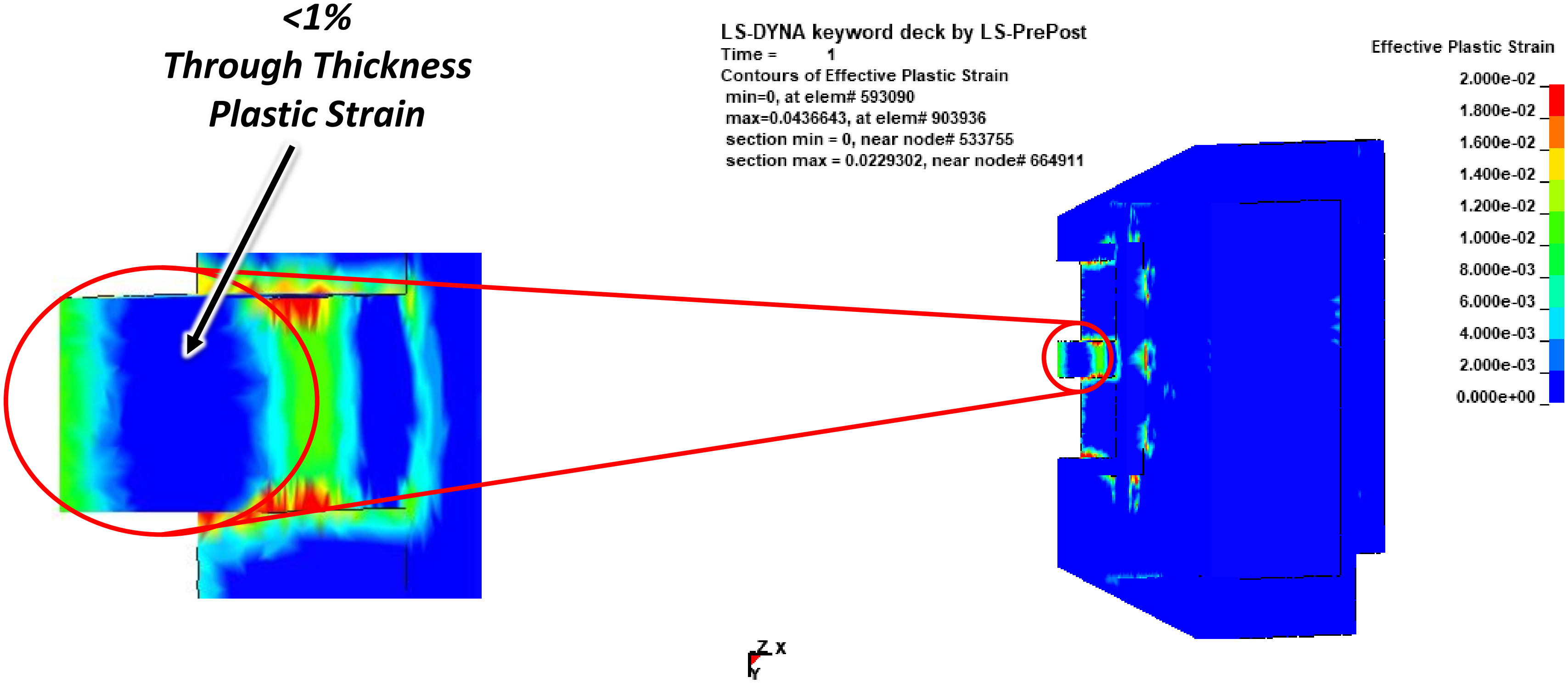

LS-DYNA keyword deck by LS-PrePost
Time = 1
Contours of Effective Plastic Strain
min=0, at elem# 593090
max=0.0436643, at elem# 903936
section min = 0, near node# 533755
section max = 0.0229302, near node# 664911

Retaining Cover, Plastic Strain Results

1.0 MJ Energy
1 g Mass

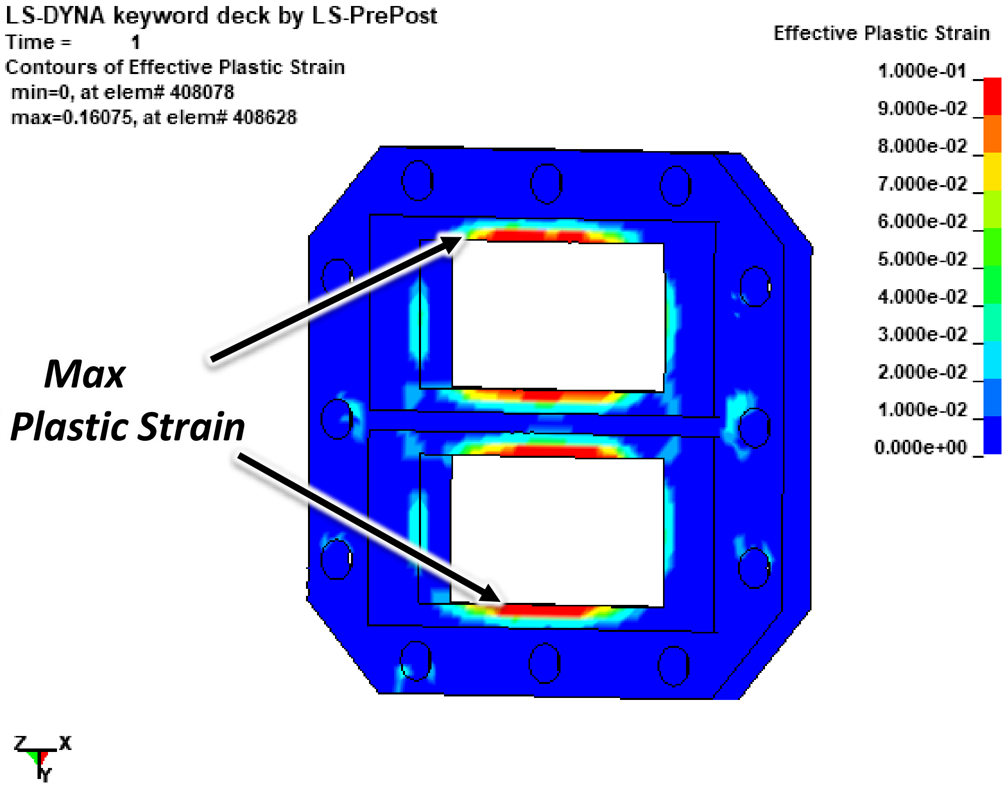

```
LS-DYNA keyword deck by LS-PrePost
Time =         1
Contours of Effective Plastic Strain
 min=0, at elem# 408078
 max=0.16075, at elem# 408628
```

Max
10% Plastic Strain

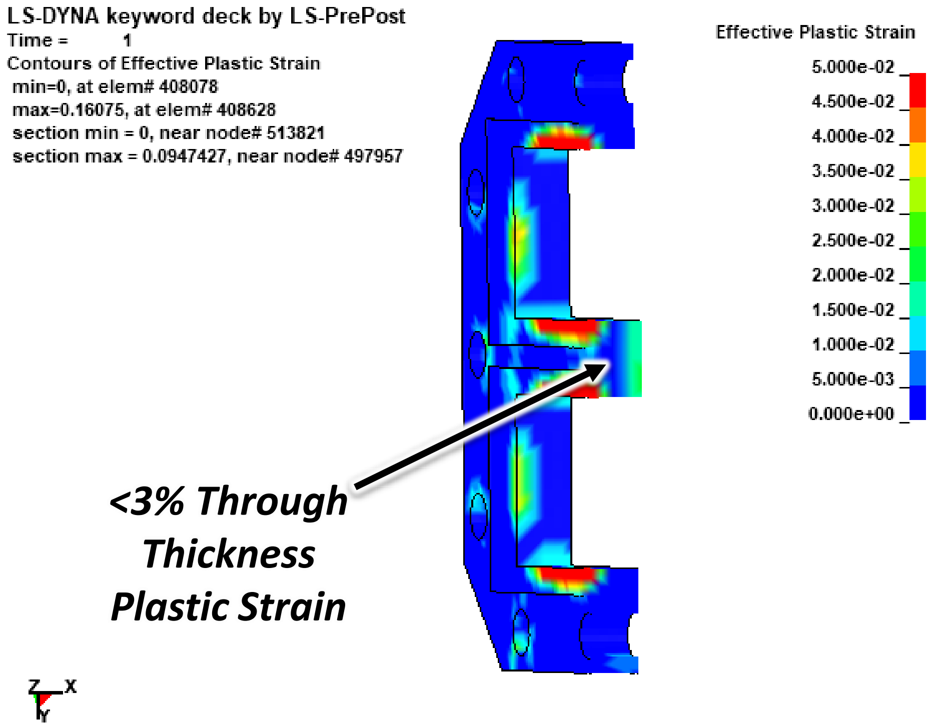

```
LS-DYNA keyword deck by LS-PrePost
Time =         1
Contours of Effective Plastic Strain
 min=0, at elem# 408078
 max=0.16075, at elem# 408628
 section min = 0, near node# 513821
 section max = 0.0947427, near node# 497957
```

<3% Through
Thickness
Plastic Strain

1.5 MJ Results

Nose-Cap, Von Mises Stress Results

1.5 MJ Energy
1 g Mass

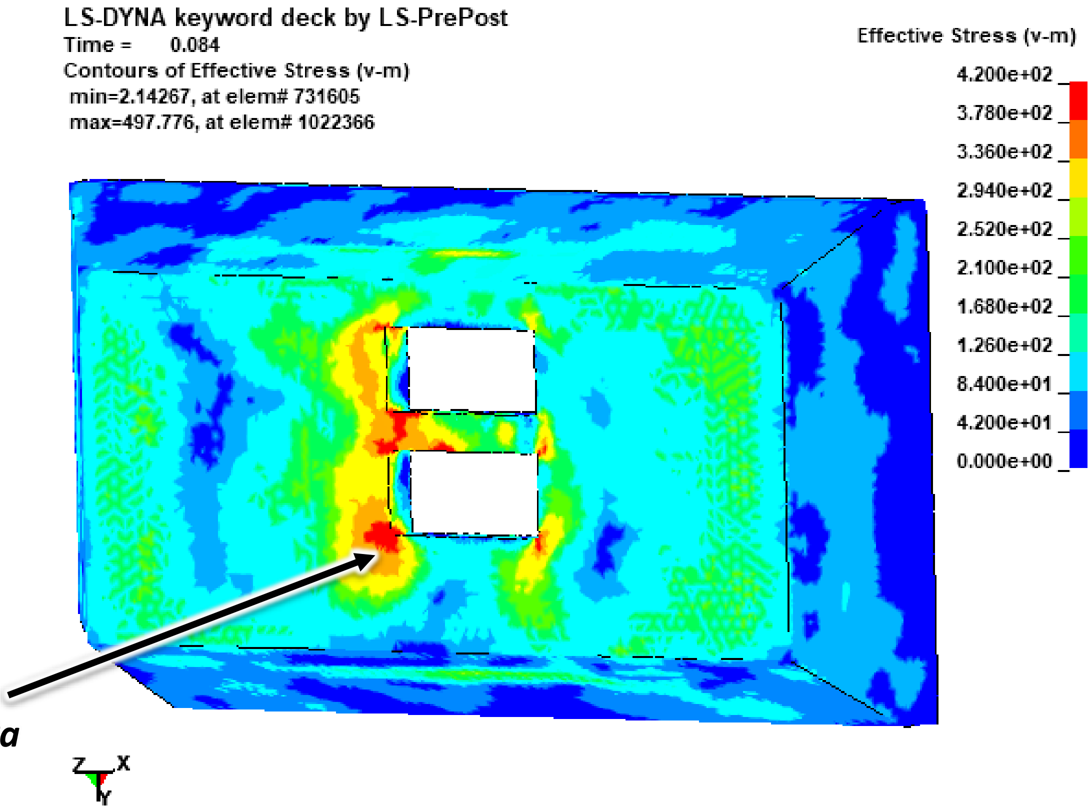

Max
420 MPa

Nose-Cap, Plastic Strain Results

1.5 MJ Energy
1 g Mass

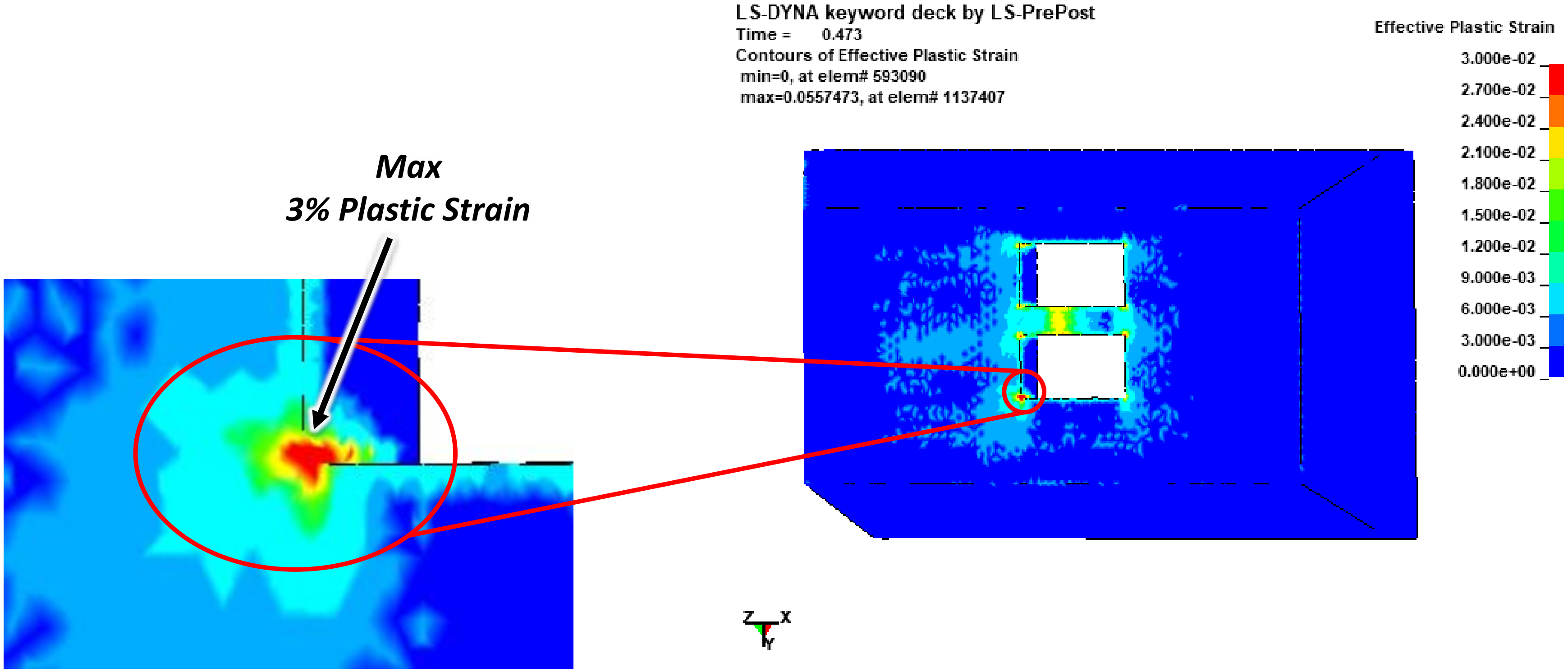

Max
3% Plastic Strain

```
LS-DYNA keyword deck by LS-PrePost
Time =      0.473
Contours of Effective Plastic Strain
 min=0, at elem# 593090
 max=0.0557473, at elem# 1137407
```

Nose-Cap, Plastic Strain Results Cont.

1.5 MJ Energy
1 g Mass

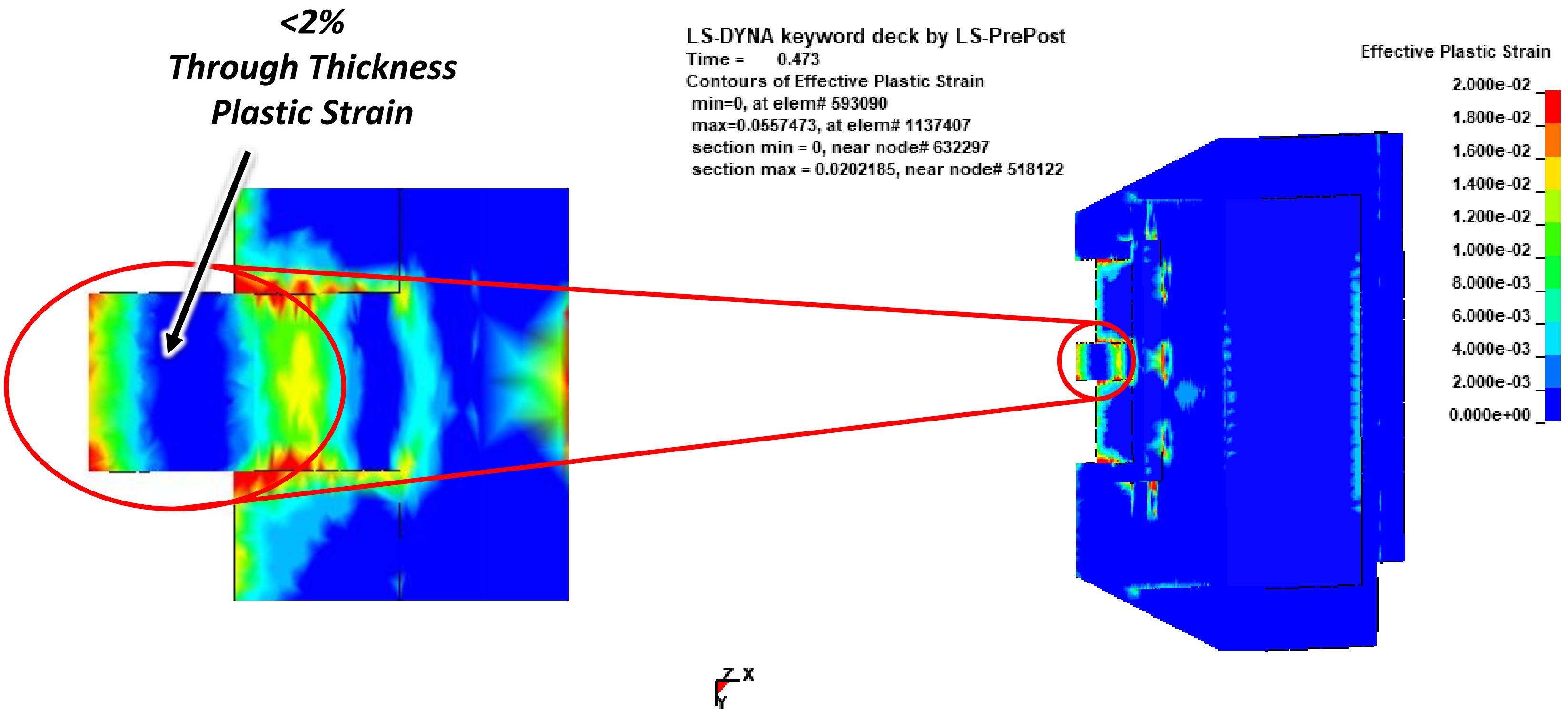

<2%
Through Thickness
Plastic Strain

```
LS-DYNA keyword deck by LS-PrePost
Time =       0.473
Contours of Effective Plastic Strain
 min=0, at elem# 593090
 max=0.0557473, at elem# 1137407
 section min = 0, near node# 632297
 section max = 0.0202185, near node# 518122
```

Tantalum, Von Mises Stress Results

1.5 MJ Energy
1 g Mass

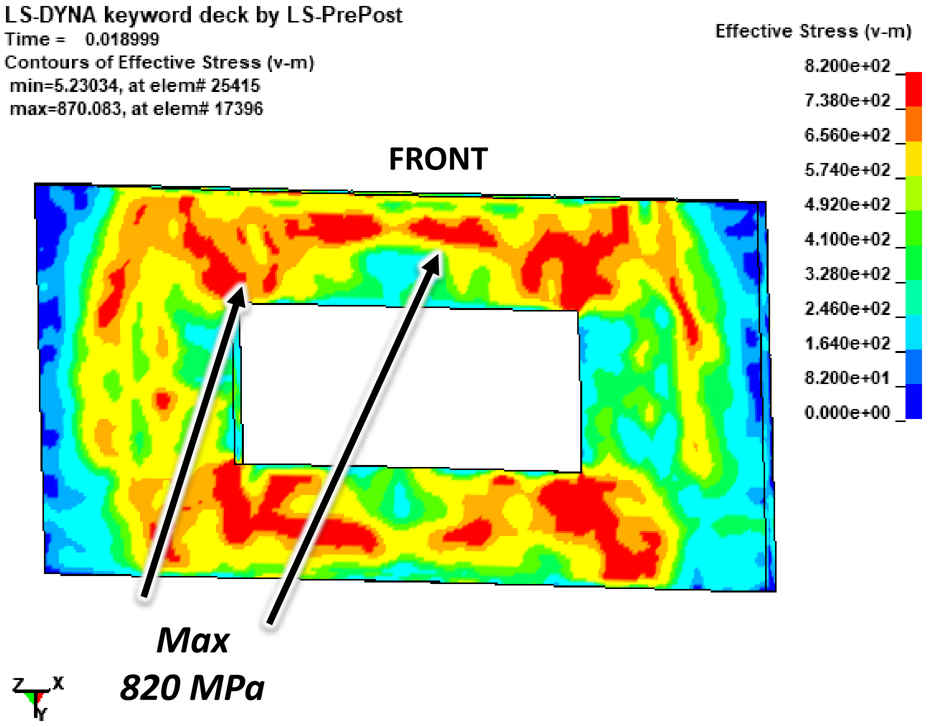

LS-DYNA keyword deck by LS-PrePost
Time = 0.018999
Contours of Effective Stress (v-m)
min=5.23034, at elem# 25415
max=870.083, at elem# 17396

Max 820 MPa

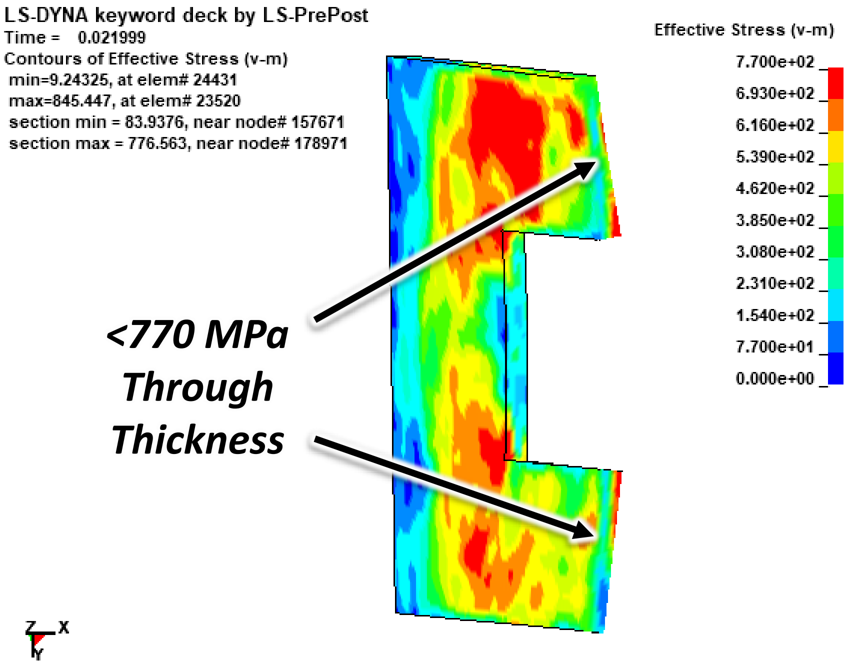

LS-DYNA keyword deck by LS-PrePost
Time = 0.021999
Contours of Effective Stress (v-m)
min=9.24325, at elem# 24431
max=845.447, at elem# 23520
section min = 83.9376, near node# 157671
section max = 776.563, near node# 178971

<770 MPa Through Thickness

Tantalum, Plastic Strain Results

1.5 MJ Energy
1 g Mass

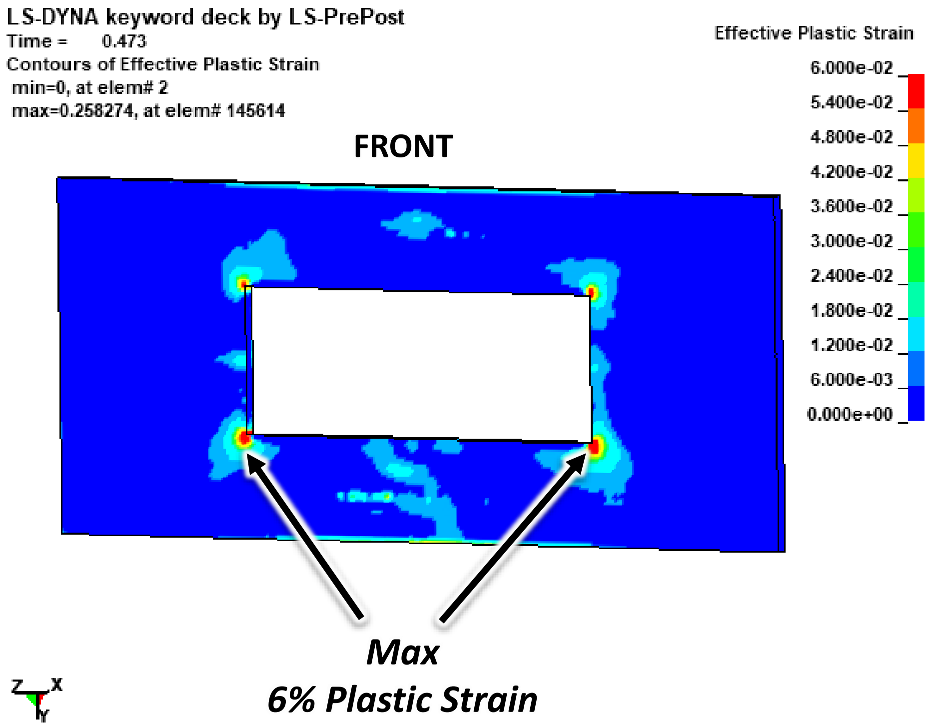

LS-DYNA keyword deck by LS-PrePost
Time = 0.473
Contours of Effective Plastic Strain
min=0, at elem# 2
max=0.258274, at elem# 145614

Max
6% Plastic Strain

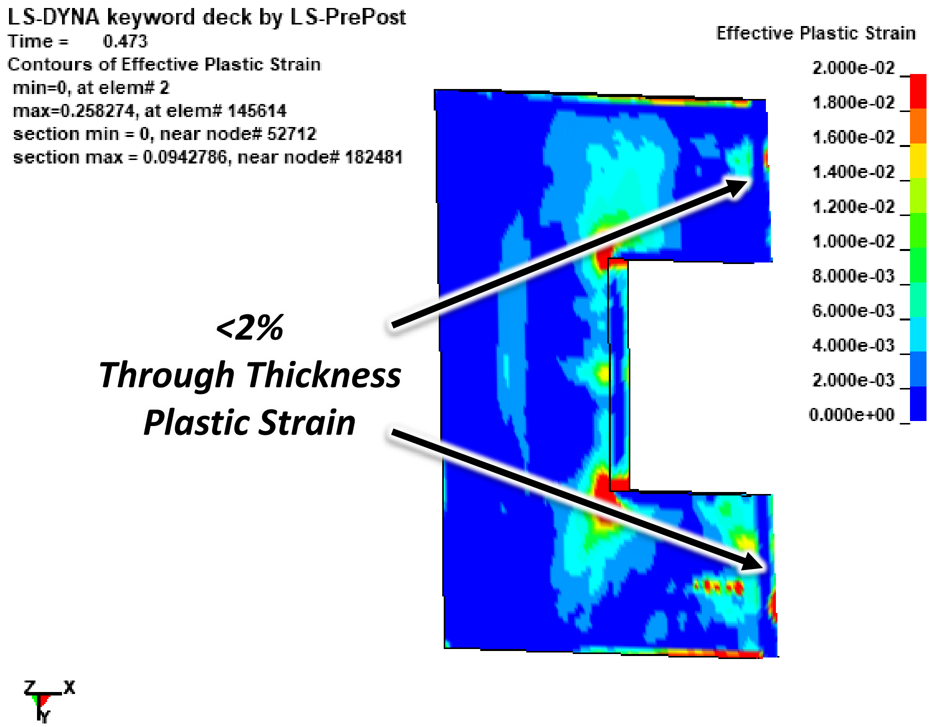

LS-DYNA keyword deck by LS-PrePost
Time = 0.473
Contours of Effective Plastic Strain
min=0, at elem# 2
max=0.258274, at elem# 145614
section min = 0, near node# 52712
section max = 0.0942786, near node# 182481

<2%
Through Thickness
Plastic Strain

Polycarbonate, Von Mises Stress Results

1.5 MJ Energy
1 g Mass

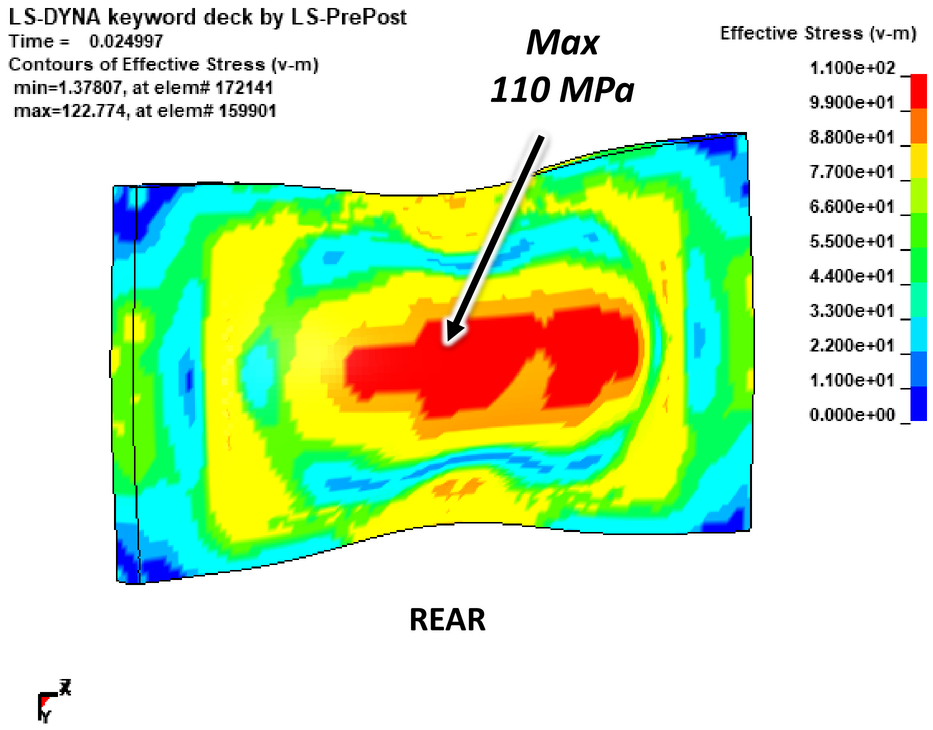

LS-DYNA keyword deck by LS-PrePost
Time = 0.024997
Contours of Effective Stress (v-m)
min=1.37807, at elem# 172141
max=122.774, at elem# 159901

Max
110 MPa

REAR

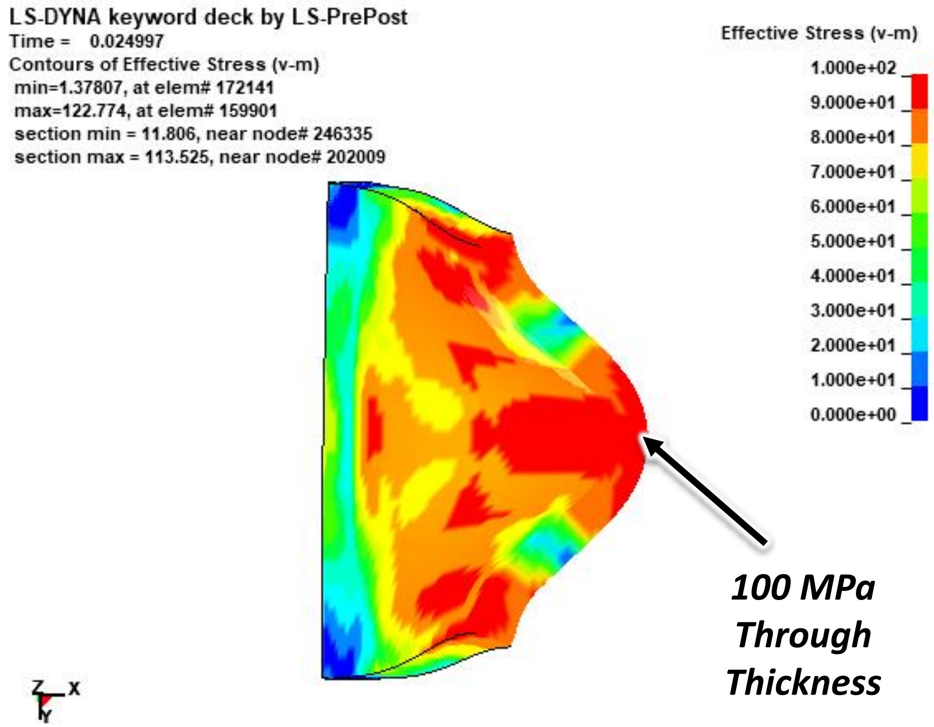

LS-DYNA keyword deck by LS-PrePost
Time = 0.024997
Contours of Effective Stress (v-m)
min=1.37807, at elem# 172141
max=122.774, at elem# 159901
section min = 11.806, near node# 246335
section max = 113.525, near node# 202009

100 MPa
Through
Thickness

Polycarbonate, Plastic Strain Results

1.5 MJ Energy
1 g Mass

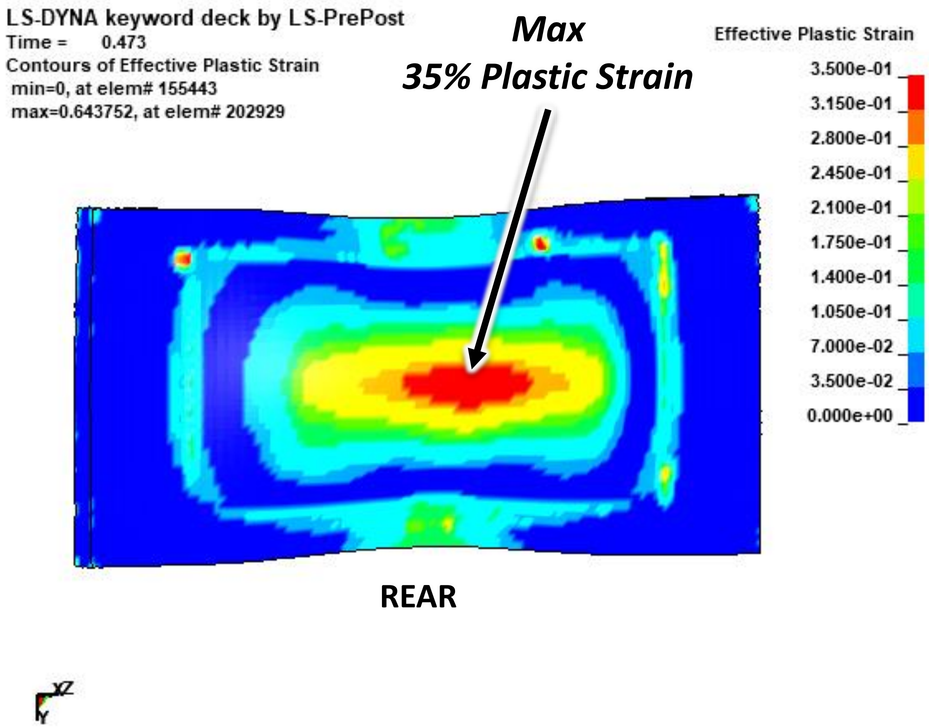

LS-DYNA keyword deck by LS-PrePost
Time = 0.473
Contours of Effective Plastic Strain
min=0, at elem# 155443
max=0.643752, at elem# 202929

Max
35% Plastic Strain

REAR

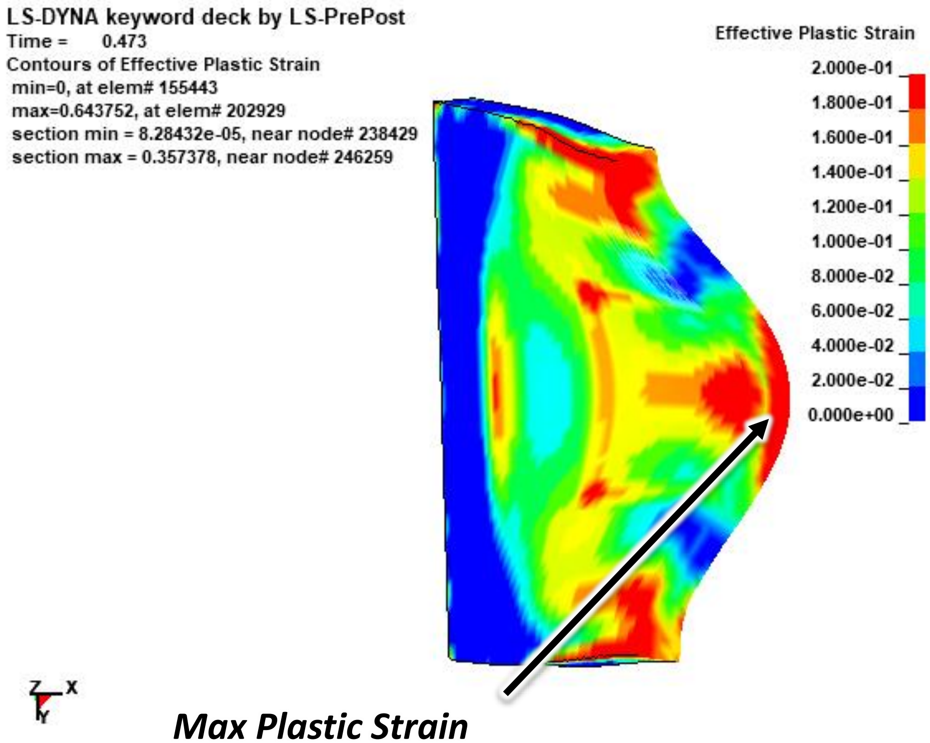

LS-DYNA keyword deck by LS-PrePost
Time = 0.473
Contours of Effective Plastic Strain
min=0, at elem# 155443
max=0.643752, at elem# 202929
section min = 8.28432e-05, near node# 238429
section max = 0.357378, near node# 246259

Max Plastic Strain
Through Thickness
20%

Retaining Cover, Von Mises Stress Results

1.5 MJ Energy
1 g Mass

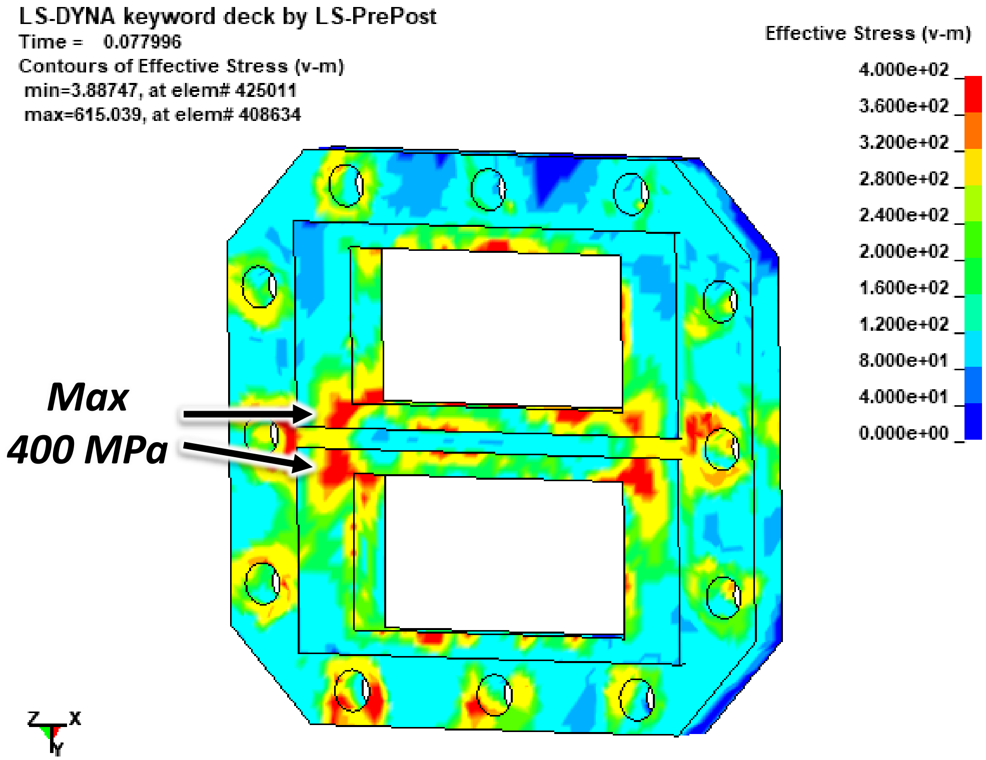
LS-DYNA keyword deck by LS-PrePost
Time = 0.077996
Contours of Effective Stress (v-m)
min=3.88747, at elem# 425011
max=615.039, at elem# 408634

Max 400 MPa

FRONT

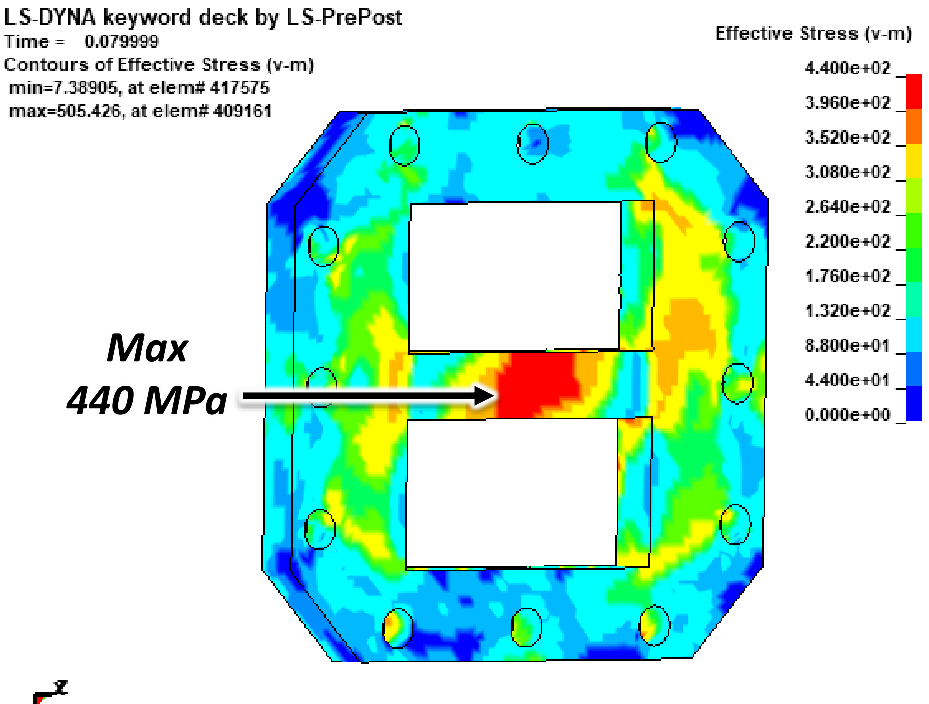
LS-DYNA keyword deck by LS-PrePost
Time = 0.079999
Contours of Effective Stress (v-m)
min=7.38905, at elem# 417575
max=505.426, at elem# 409161

Max 440 MPa

REAR

Retaining Cover, Von Mises Stress Cont.

1.5 MJ Energy
1 g Mass

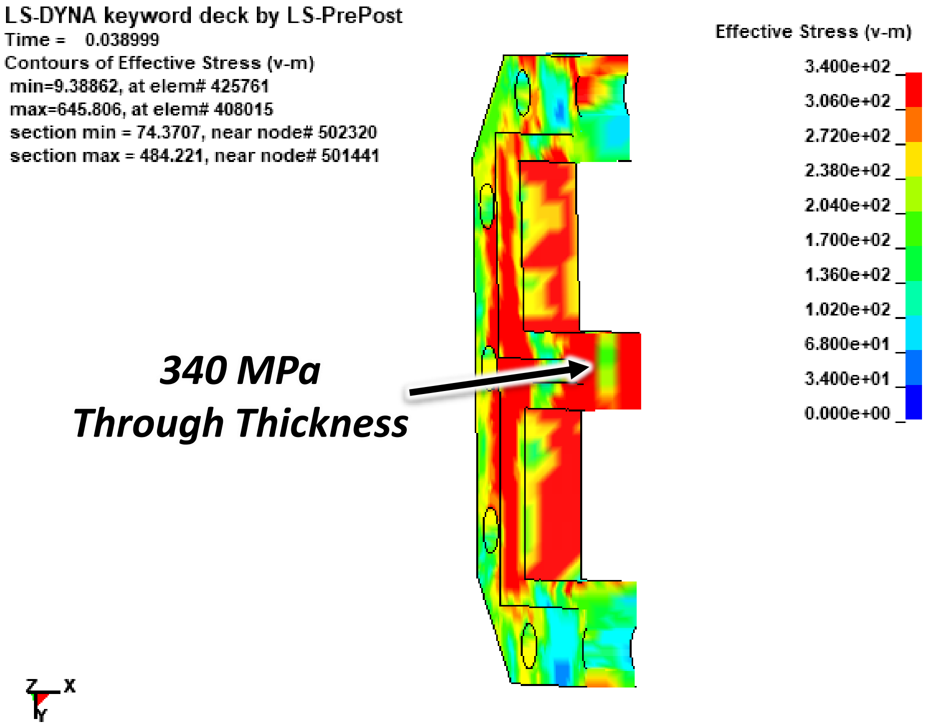

LS-DYNA keyword deck by LS-PrePost
Time = 0.038999
Contours of Effective Stress (v-m)
min=9.38862, at elem# 425761
max=645.806, at elem# 408015
section min = 74.3707, near node# 502320
section max = 484.221, near node# 501441

340 MPa
Through Thickness

Retaining Cover, Plastic Strain Results

1.5 MJ Energy
1 g Mass

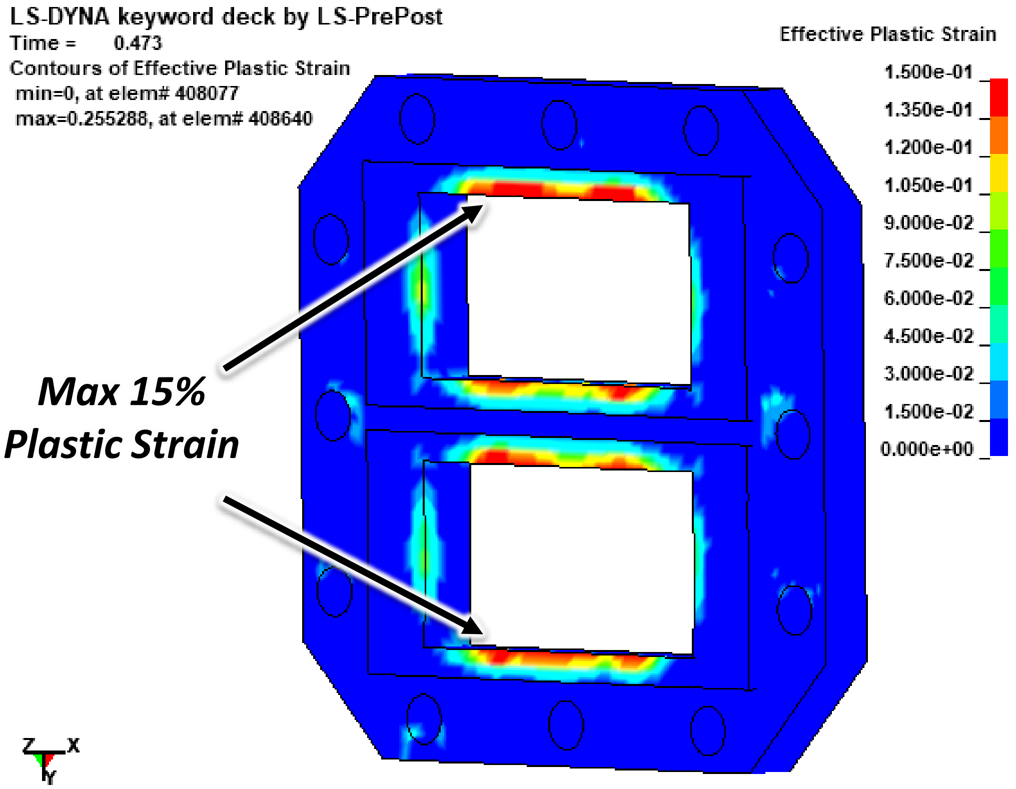

Max 15% Plastic Strain

Retaining Cover, Plastic Strain Results Cont.

1.5 MJ Energy
1 g Mass

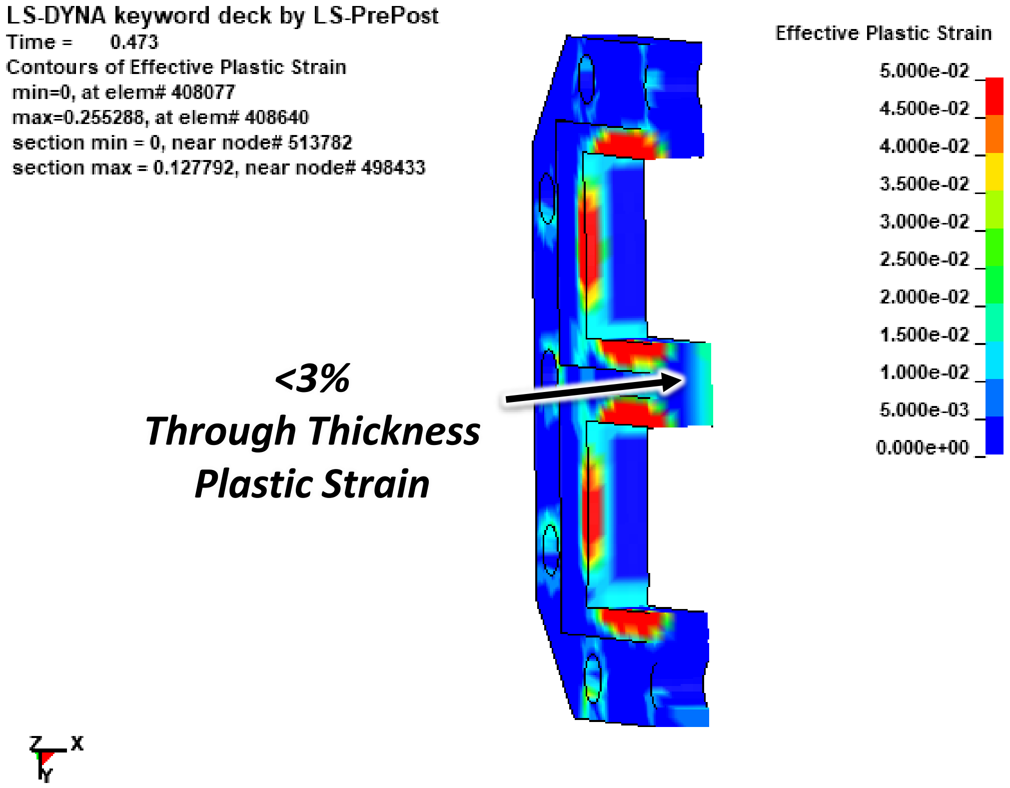

```
LS-DYNA keyword deck by LS-PrePost
Time =      0.473
Contours of Effective Plastic Strain
 min=0, at elem# 408077
 max=0.255288, at elem# 408640
 section min = 0, near node# 513782
 section max = 0.127792, near node# 498433
```

<3%
Through Thickness
Plastic Strain

2.1 MJ, 5 mm Polycarbonate Results

Nose-Cap, Von Mises Stress Results

2.1 MJ Energy
1 g Mass
5 mm Polycarbonate

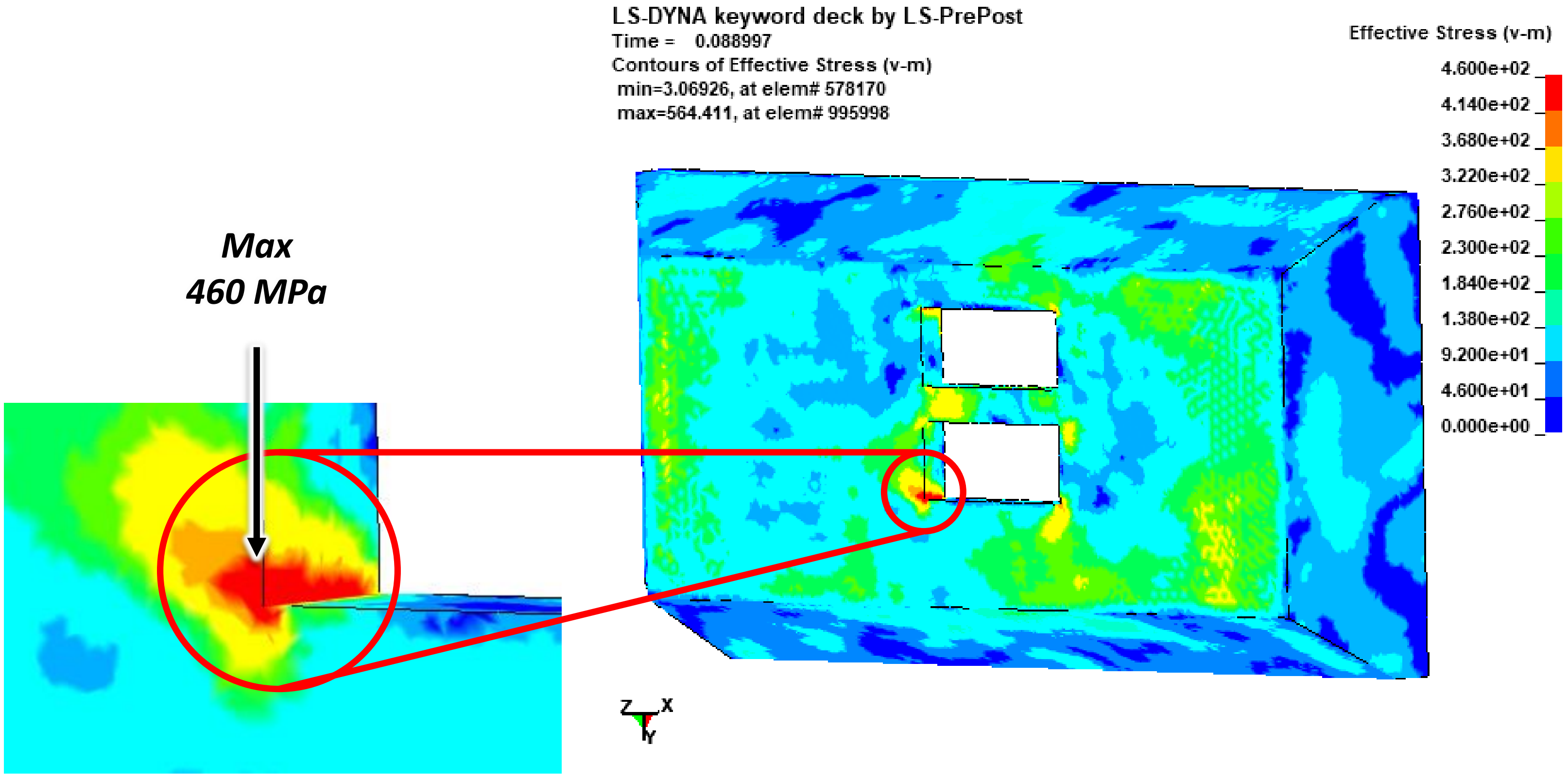

LS-DYNA keyword deck by LS-PrePost
Time = 0.088997
Contours of Effective Stress (v-m)
min=3.06926, at elem# 578170
max=564.411, at elem# 995998

Max
460 MPa

Nose-Cap, Von Mises Stress Cont.

2.1 MJ Energy
1 g Mass
5 mm Polycarbonate

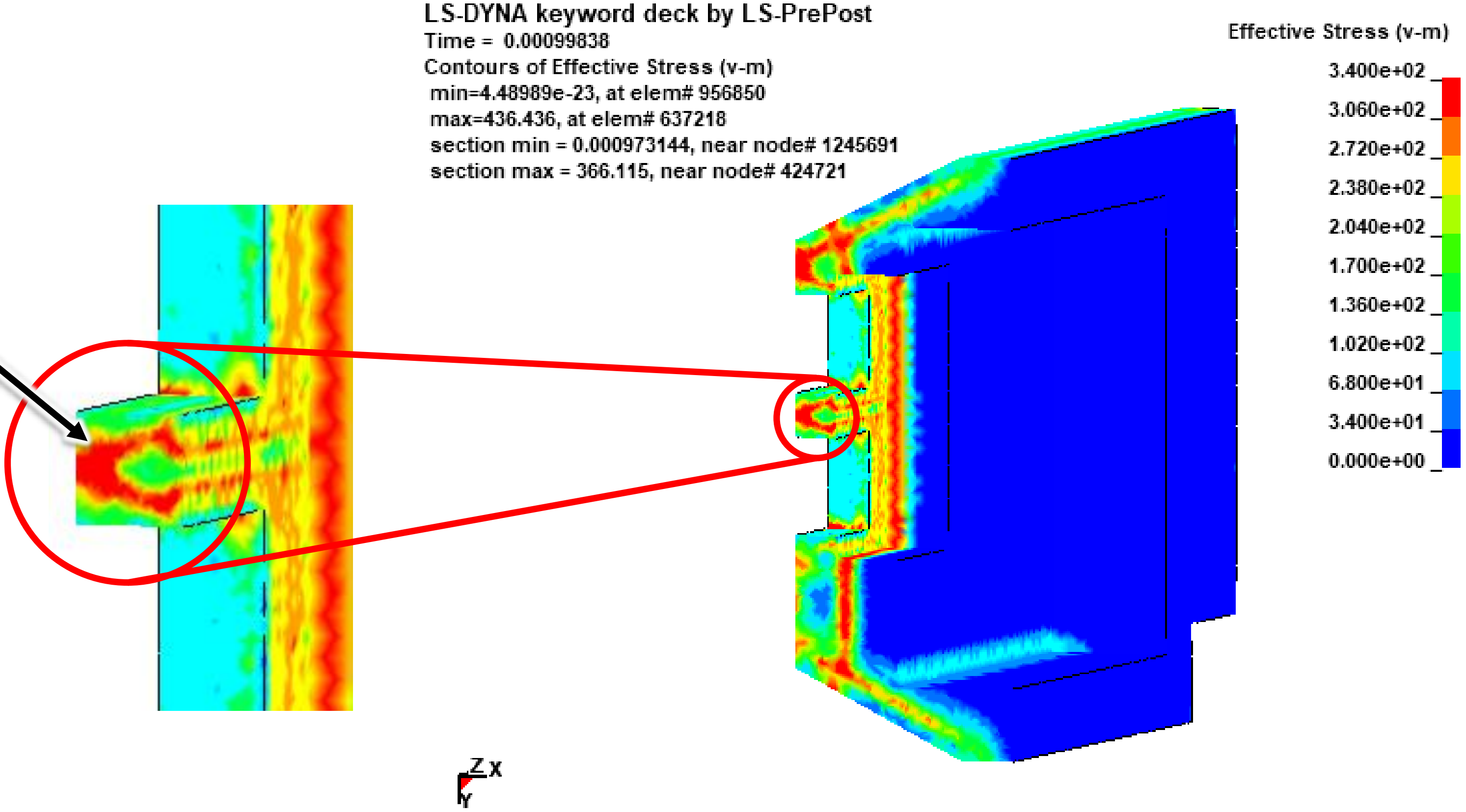

LS-DYNA keyword deck by LS-PrePost
Time = 0.00099838
Contours of Effective Stress (v-m)
min=4.48989e-23, at elem# 956850
max=436.436, at elem# 637218
section min = 0.000973144, near node# 1245691
section max = 366.115, near node# 424721

Max
340 MPa

Nose-Cap, Plastic Strain Results

2.1 MJ Energy
1 g Mass
5 mm Polycarbonate

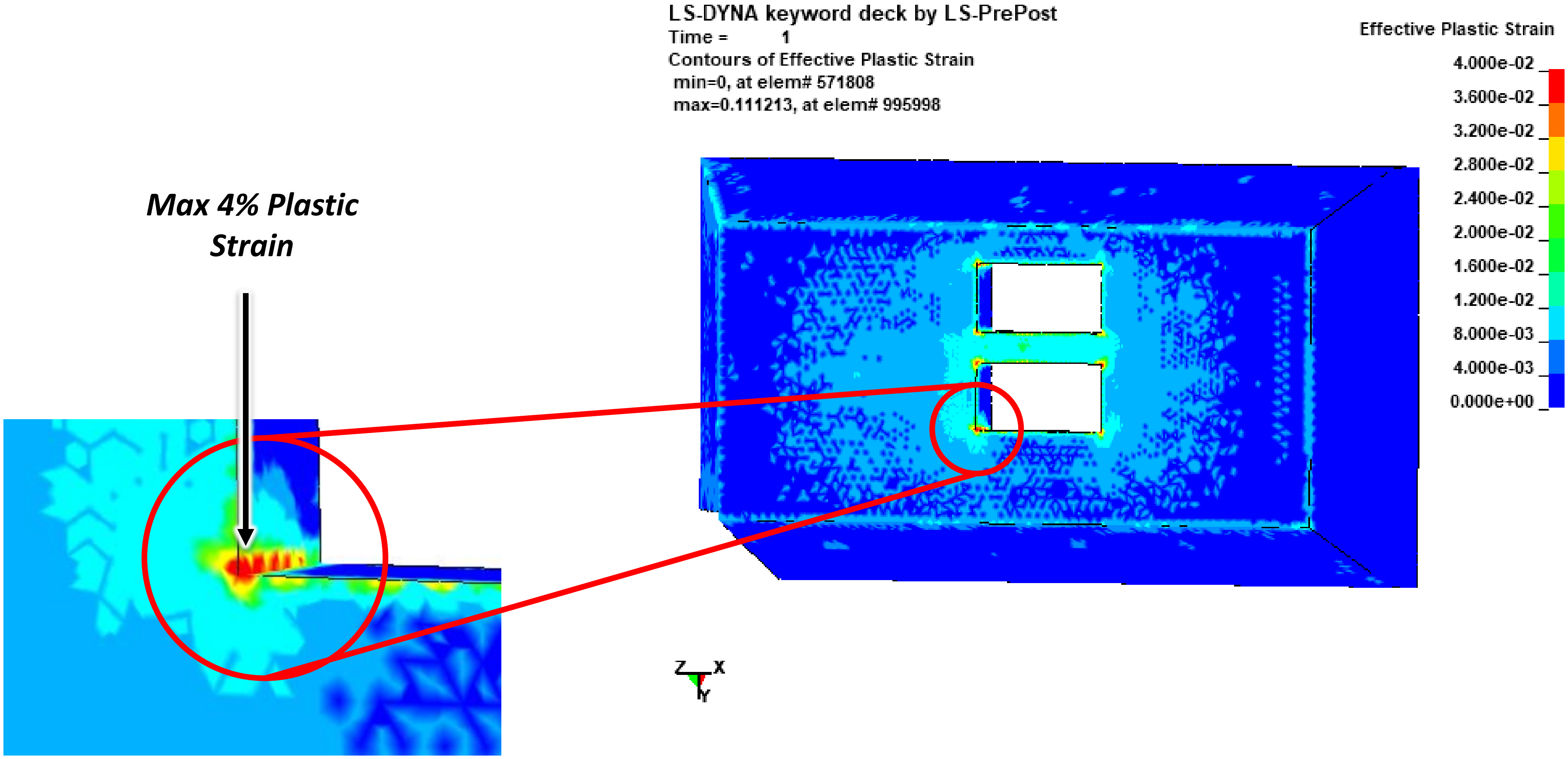

LS-DYNA keyword deck by LS-PrePost
Time = 1
Contours of Effective Plastic Strain
min=0, at elem# 571808
max=0.111213, at elem# 995998

Max 4% Plastic Strain

Nose-Cap, Plastic Strain Results Cont.

2.1 MJ Energy
1 g Mass
5 mm Polycarbonate

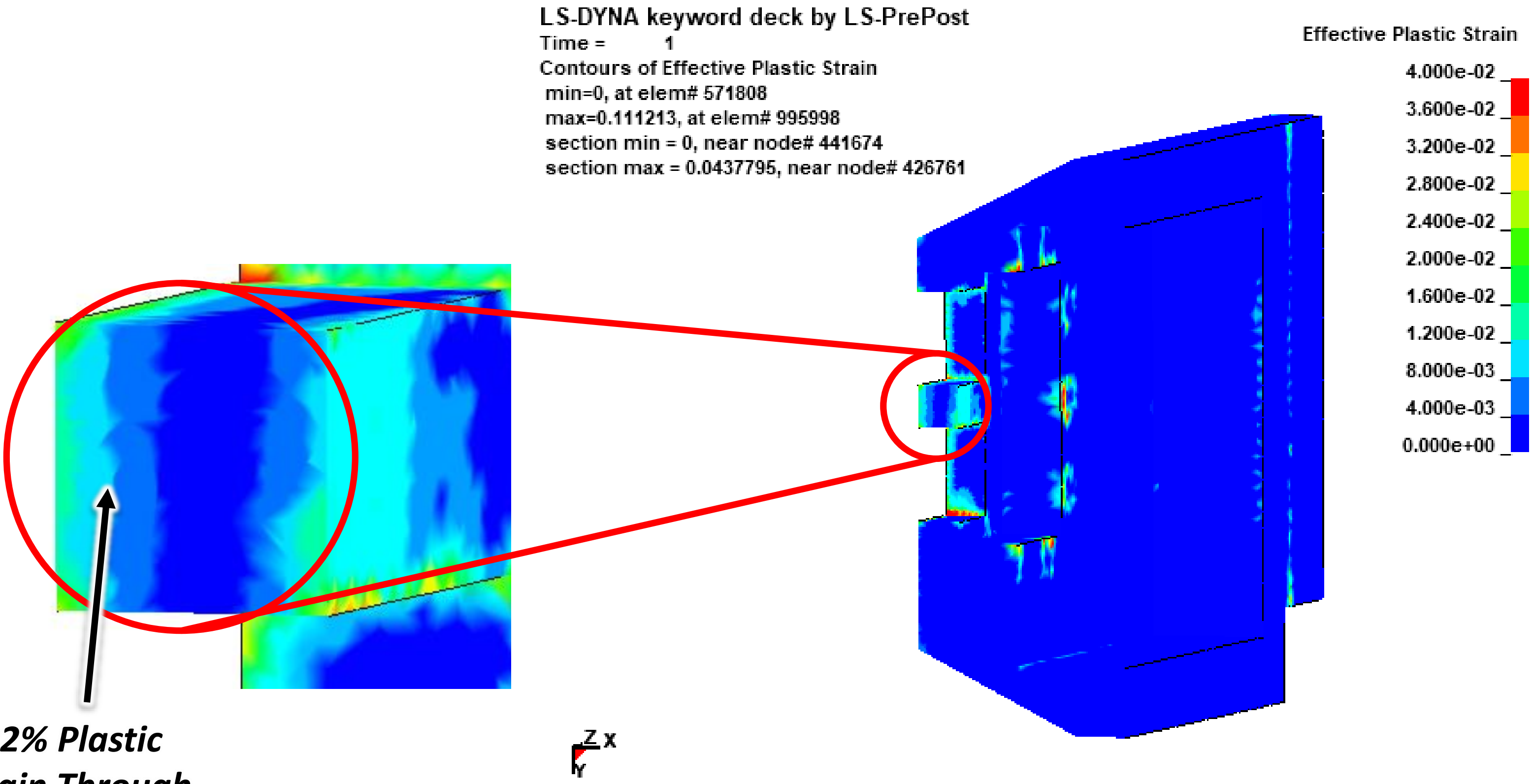

```
LS-DYNA keyword deck by LS-PrePost
Time =         1
Contours of Effective Plastic Strain
 min=0, at elem# 571808
 max=0.111213, at elem# 995998
 section min = 0, near node# 441674
 section max = 0.0437795, near node# 426761
```

<2% Plastic Strain Through Thickness

Tantalum, Von Mises Stress Results

2.1 MJ Energy
1 g Mass
5 mm Polycarbonate

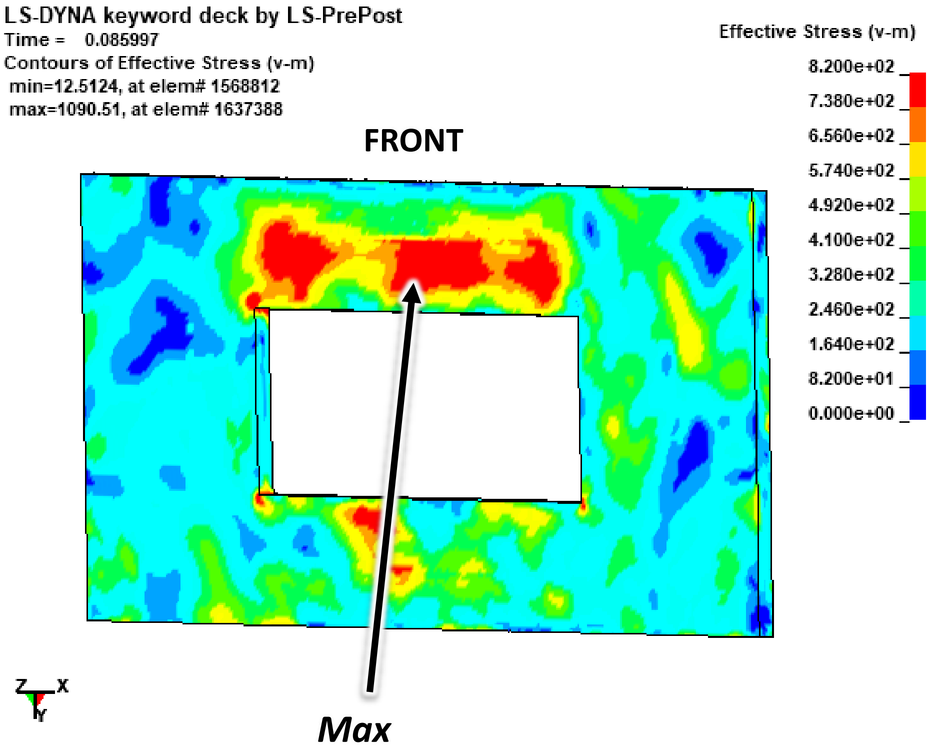

```
LS-DYNA keyword deck by LS-PrePost
Time =    0.085997
Contours of Effective Stress (v-m)
 min=12.5124, at elem# 1568812
 max=1090.51, at elem# 1637388
```

Max
820 MPa

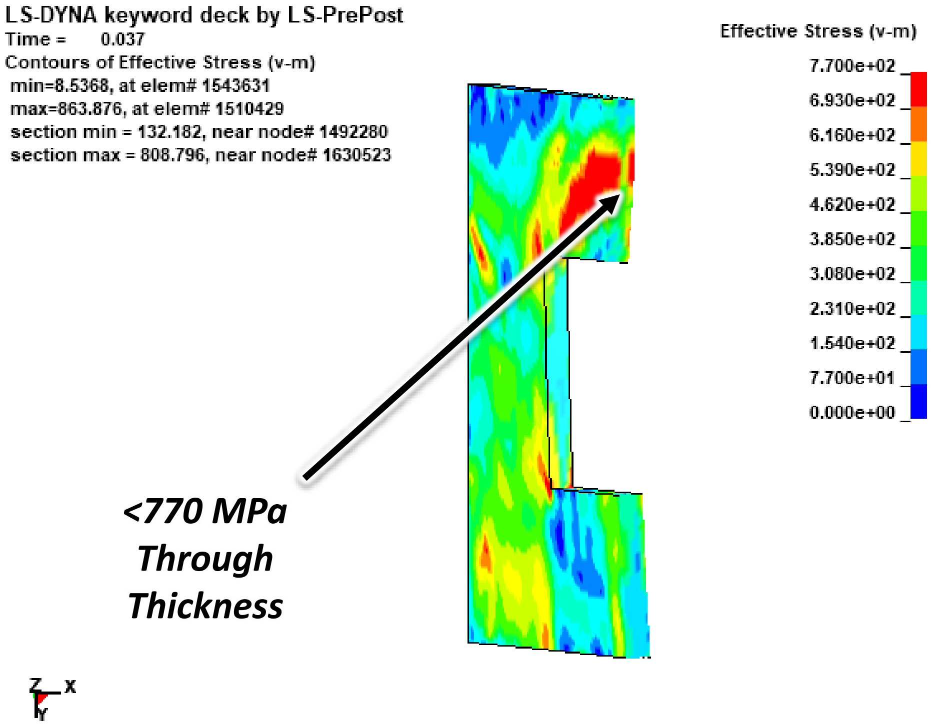

```
LS-DYNA keyword deck by LS-PrePost
Time =    0.037
Contours of Effective Stress (v-m)
 min=8.5368, at elem# 1543631
 max=863.876, at elem# 1510429
 section min = 132.182, near node# 1492280
 section max = 808.796, near node# 1630523
```

<770 MPa
Through
Thickness

Tantalum, Plastic Strain Results

2.1 MJ Energy
1 g Mass
5 mm Polycarbonate

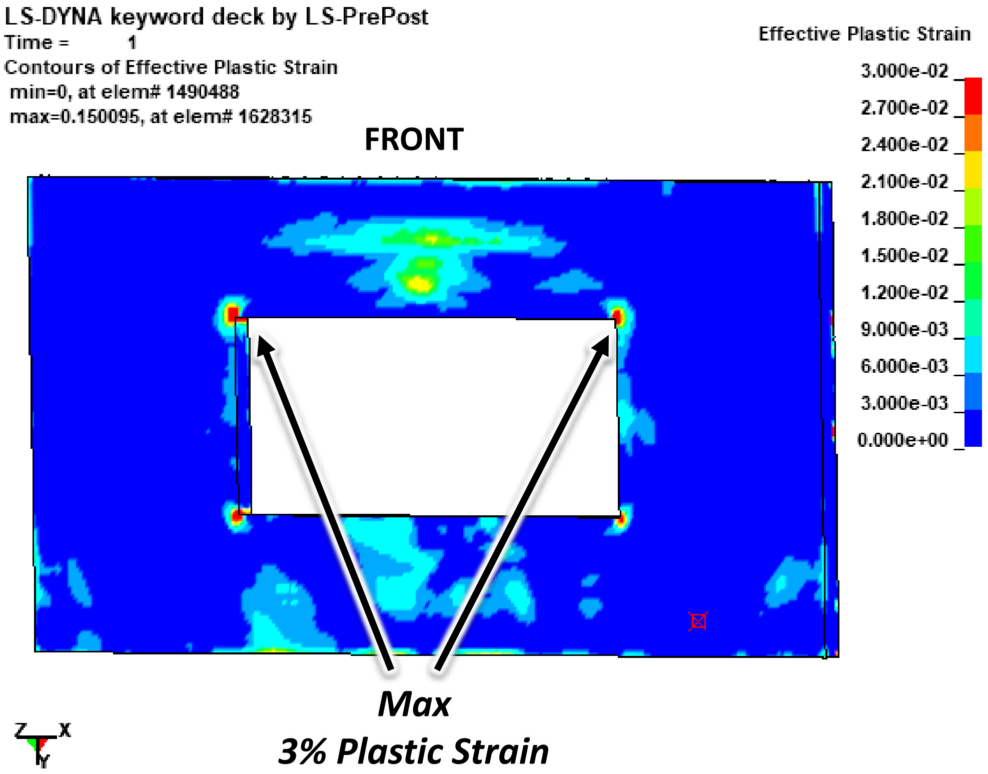

LS-DYNA keyword deck by LS-PrePost
Time = 1
Contours of Effective Plastic Strain
min=0, at elem# 1490488
max=0.150095, at elem# 1628315

FRONT

Max
3% Plastic Strain

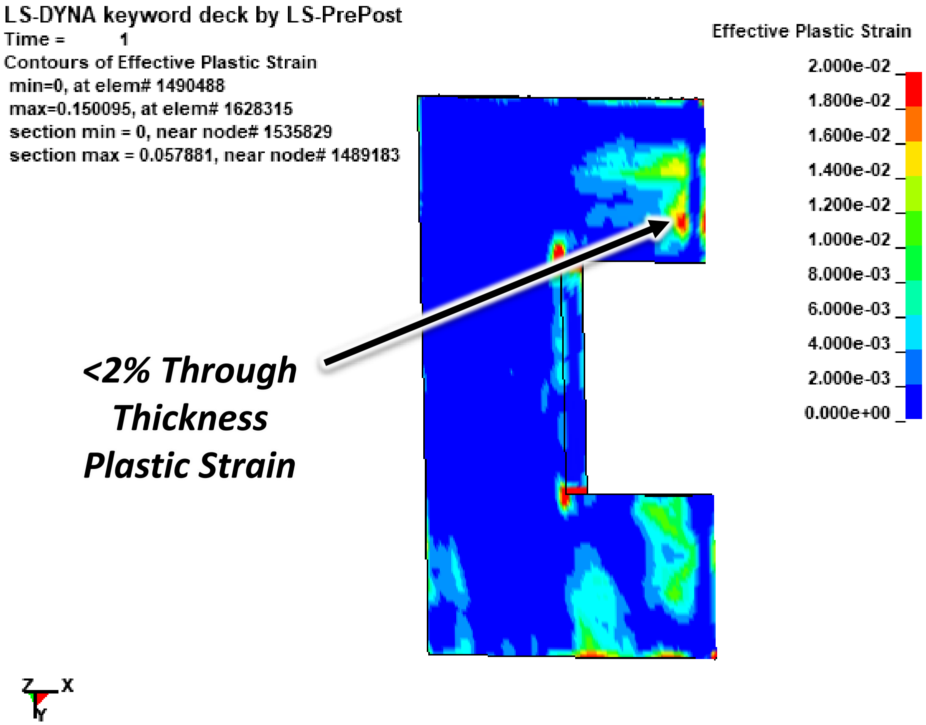

LS-DYNA keyword deck by LS-PrePost
Time = 1
Contours of Effective Plastic Strain
min=0, at elem# 1490488
max=0.150095, at elem# 1628315
section min = 0, near node# 1535829
section max = 0.057881, near node# 1489183

<2% Through
Thickness
Plastic Strain

Retaining Cover, Von Mises Stress Results

2.1 MJ Energy
1 g Mass
5 mm Polycarbonate

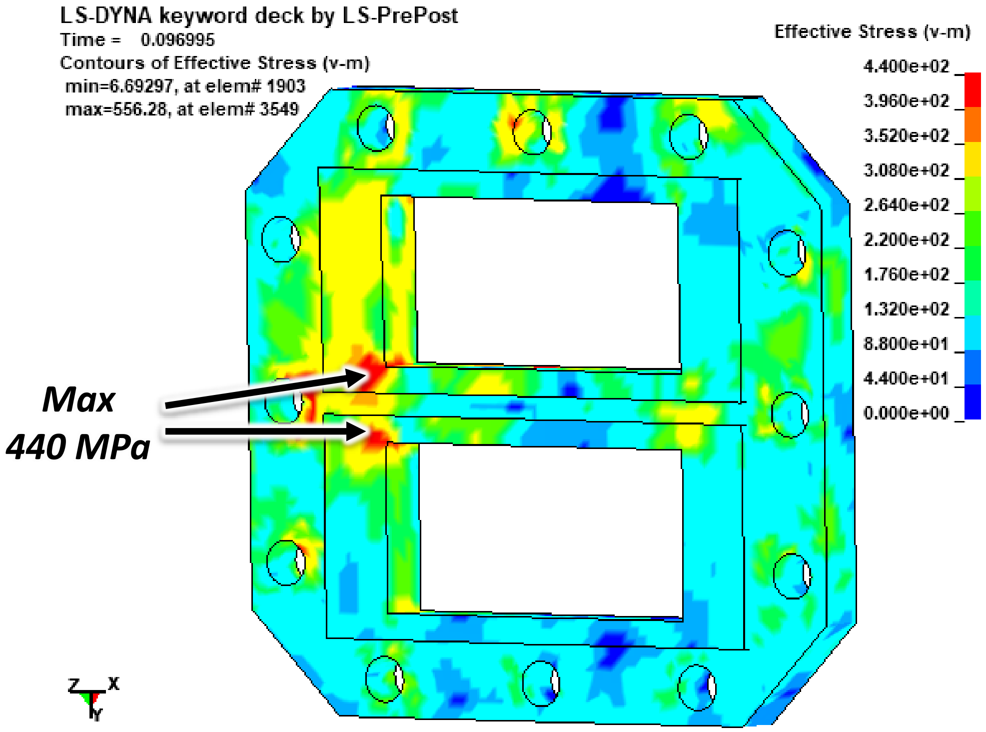

LS-DYNA keyword deck by LS-PrePost
Time = 0.096995
Contours of Effective Stress (v-m)
min=6.69297, at elem# 1903
max=556.28, at elem# 3549

FRONT

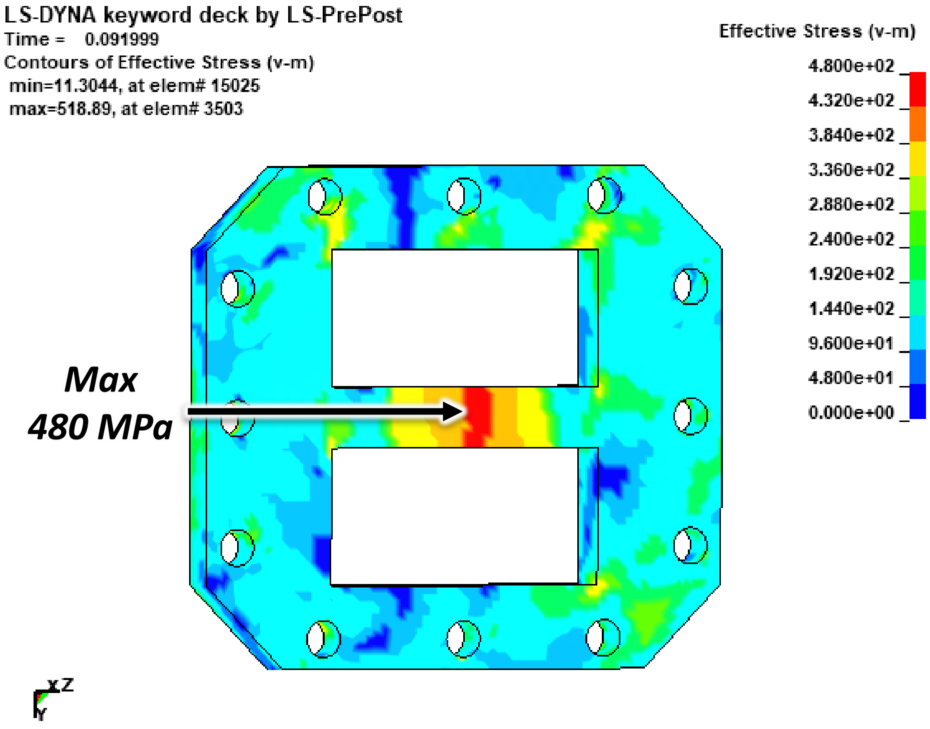

LS-DYNA keyword deck by LS-PrePost
Time = 0.091999
Contours of Effective Stress (v-m)
min=11.3044, at elem# 15025
max=518.89, at elem# 3503

REAR

Retaining Cover, Plastic Strain Results

2.1 MJ Energy
1 g Mass
5 mm Polycarbonate

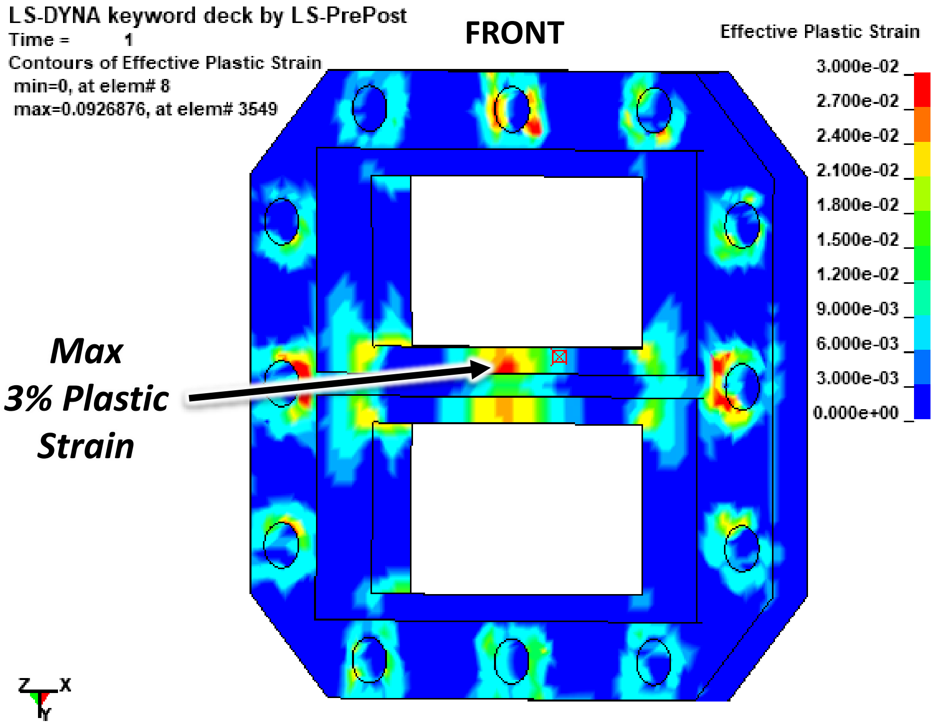

Max
3% Plastic
Strain

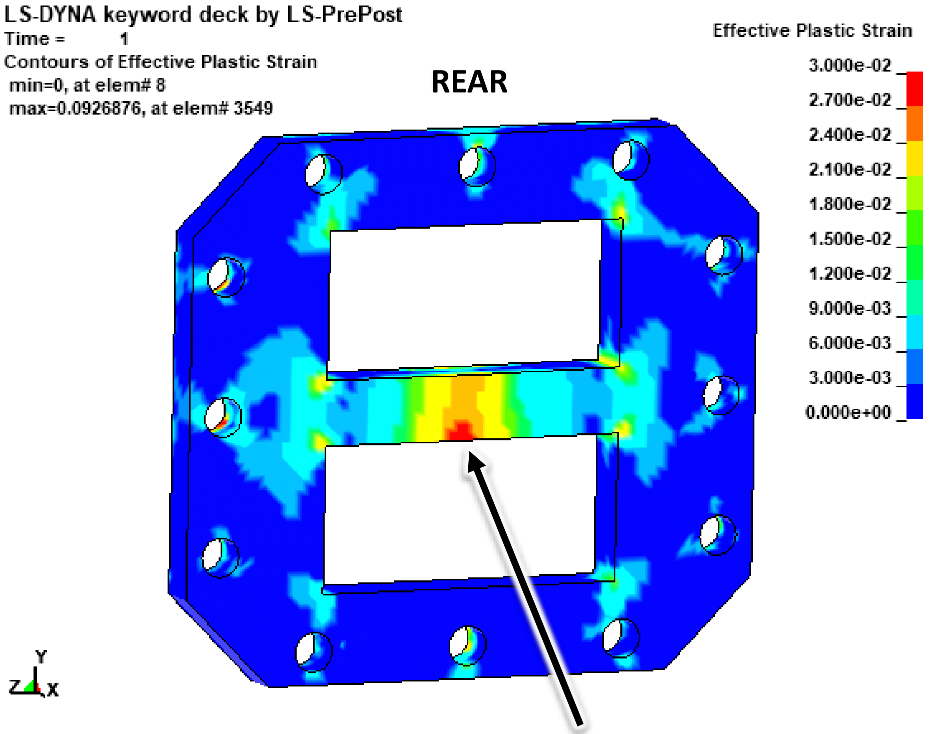

Max
3% Plastic Strain

Retaining Cover, Plastic Strain Cont.

2.1 MJ Energy
1 g Mass
5 mm Polycarbonate

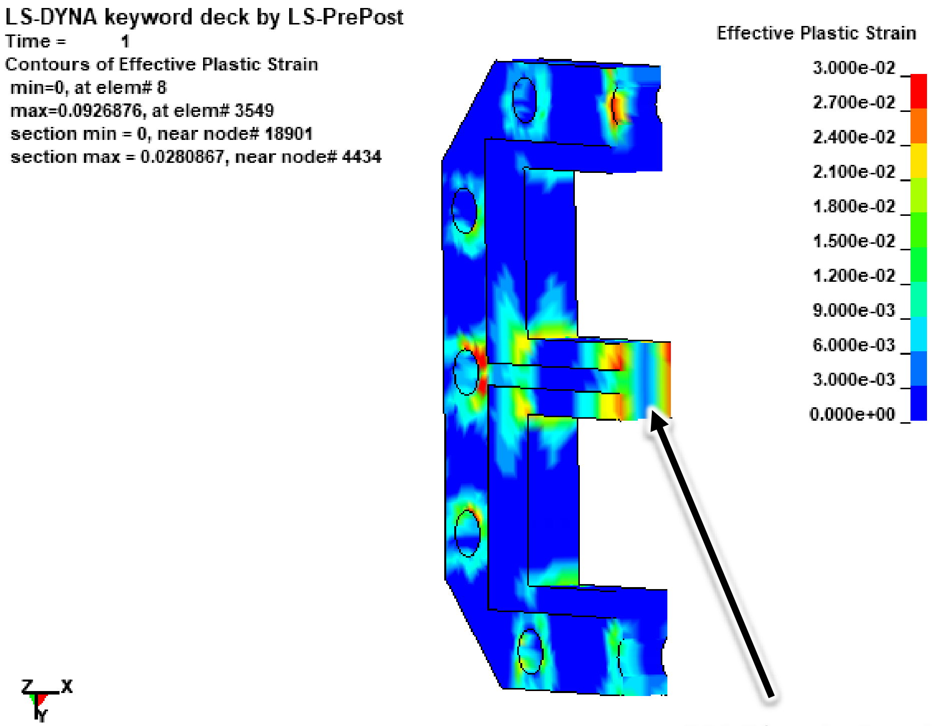

LS-DYNA keyword deck by LS-PrePost
Time = 1
Contours of Effective Plastic Strain
min=0, at elem# 8
max=0.0926876, at elem# 3549
section min = 0, near node# 18901
section max = 0.0280867, near node# 4434

<3% Plastic Strain Through Thickness

2.1 MJ, 3 mm Polycarbonate Results

Nose-Cap, Von Mises Stress Results

2.1 MJ Energy
1 g Mass
3 mm Polycarbonate

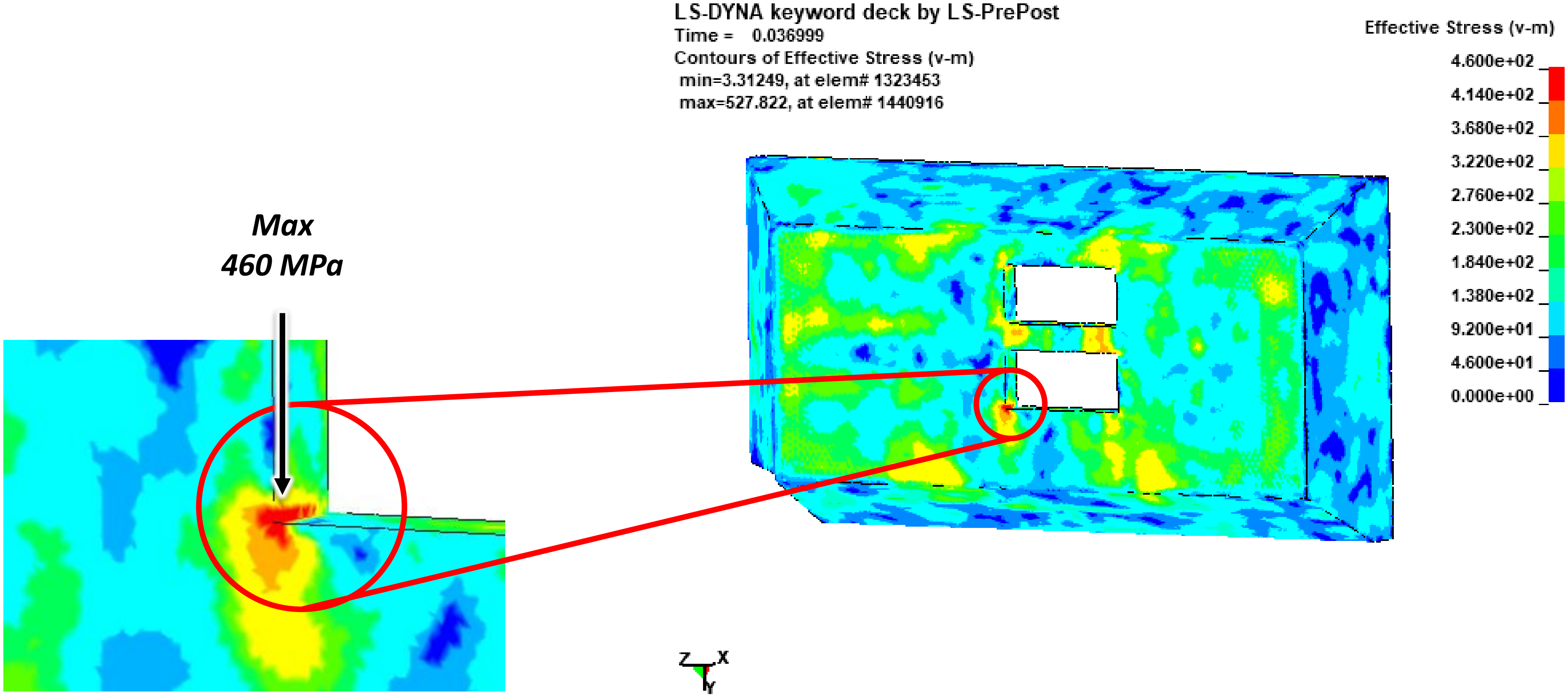

Max
460 MPa

Nose-Cap, Von Mises Stress Results Cont.

2.1 MJ Energy
1 g Mass
3 mm Polycarbonate

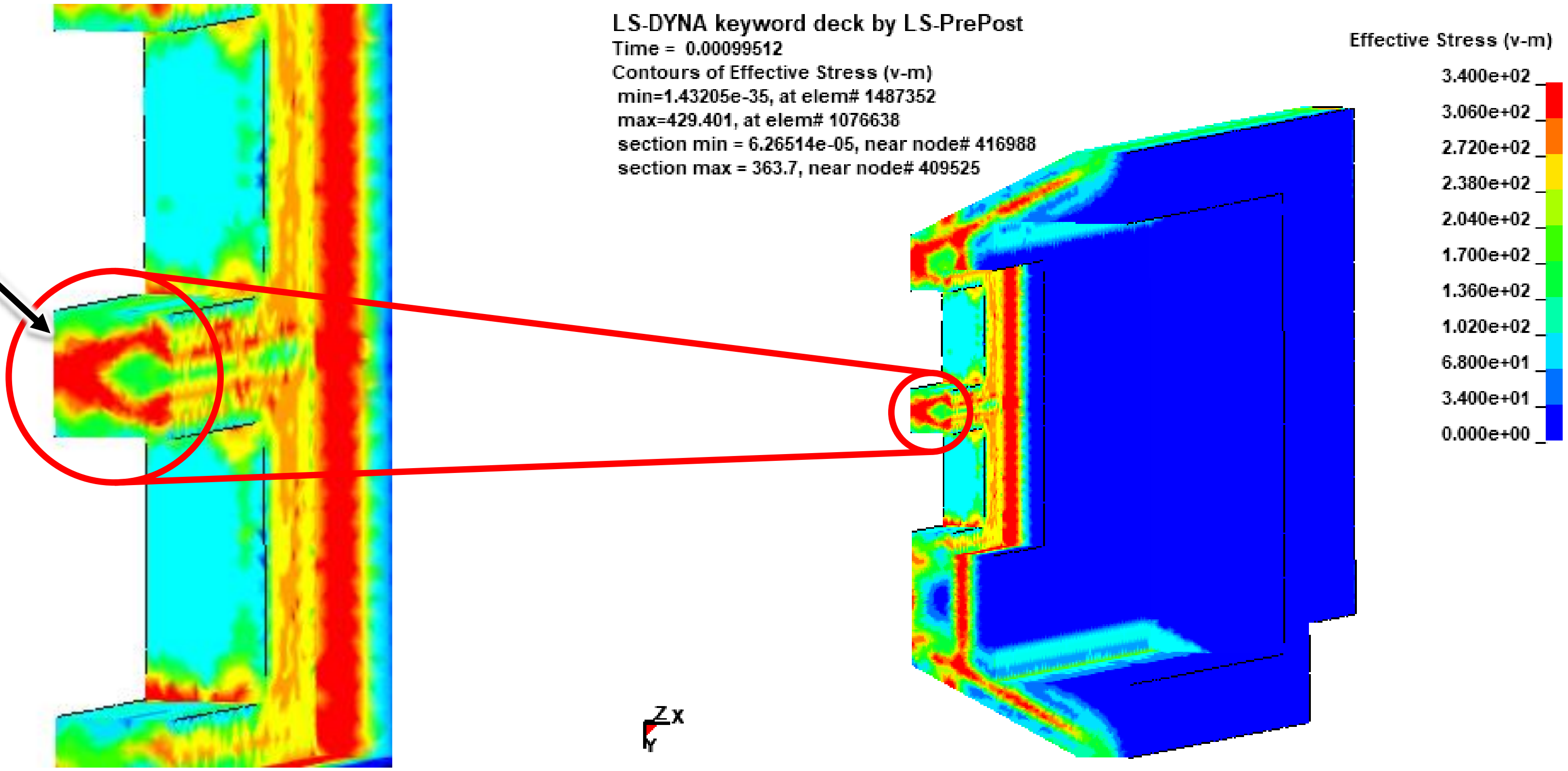

Max
340 MPa

```
LS-DYNA keyword deck by LS-PrePost
Time =  0.00099512
Contours of Effective Stress (v-m)
 min=1.43205e-35, at elem# 1487352
 max=429.401, at elem# 1076638
 section min = 6.26514e-05, near node# 416988
 section max = 363.7, near node# 409525
```

Nose-Cap, Plastic Strain Results

2.1 MJ Energy
1 g Mass
3 mm Polycarbonate

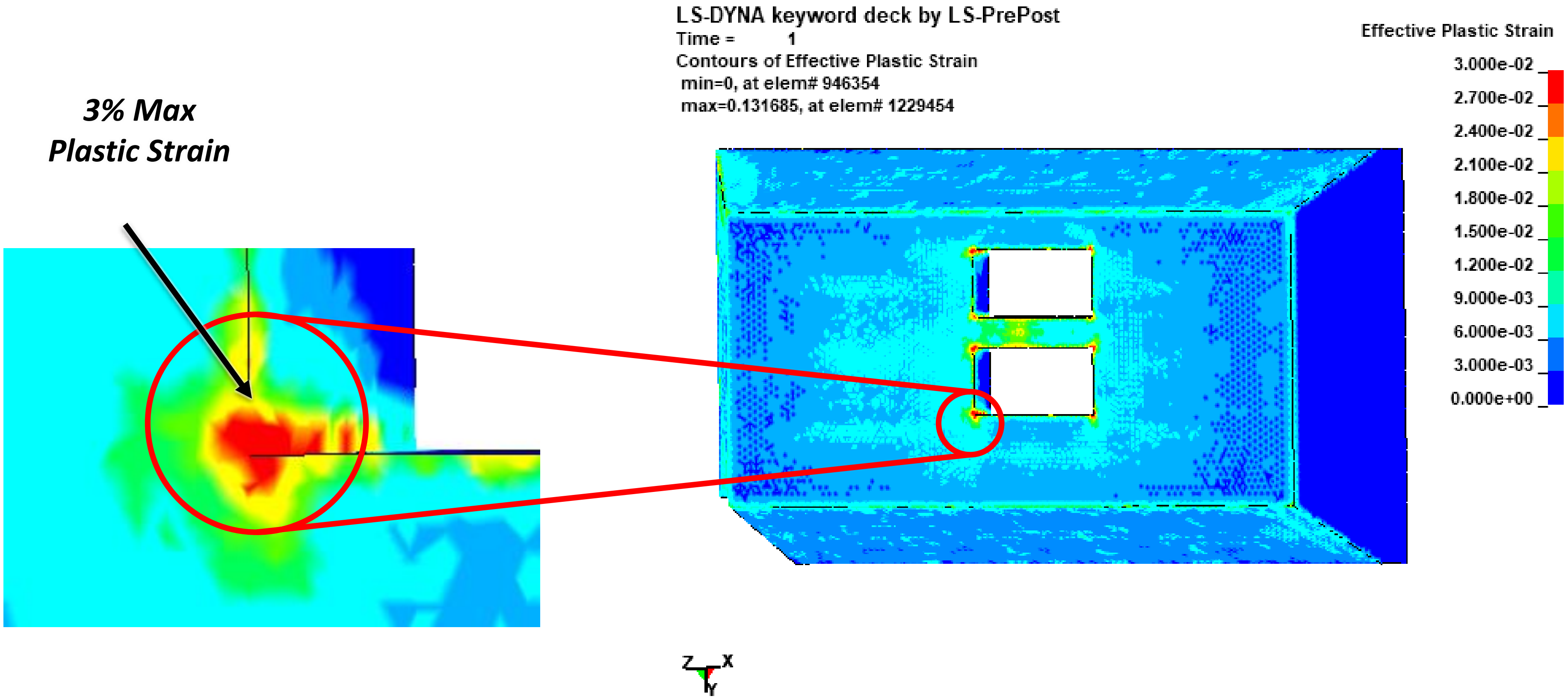

3% Max
Plastic Strain

LS-DYNA keyword deck by LS-PrePost
Time = 1
Contours of Effective Plastic Strain
min=0, at elem# 946354
max=0.131685, at elem# 1229454

Nose-Cap, Plastic Strain Results Cont.

2.1 MJ Energy
1 g Mass
3 mm Polycarbonate

<2% Plastic Strain Through Thickness

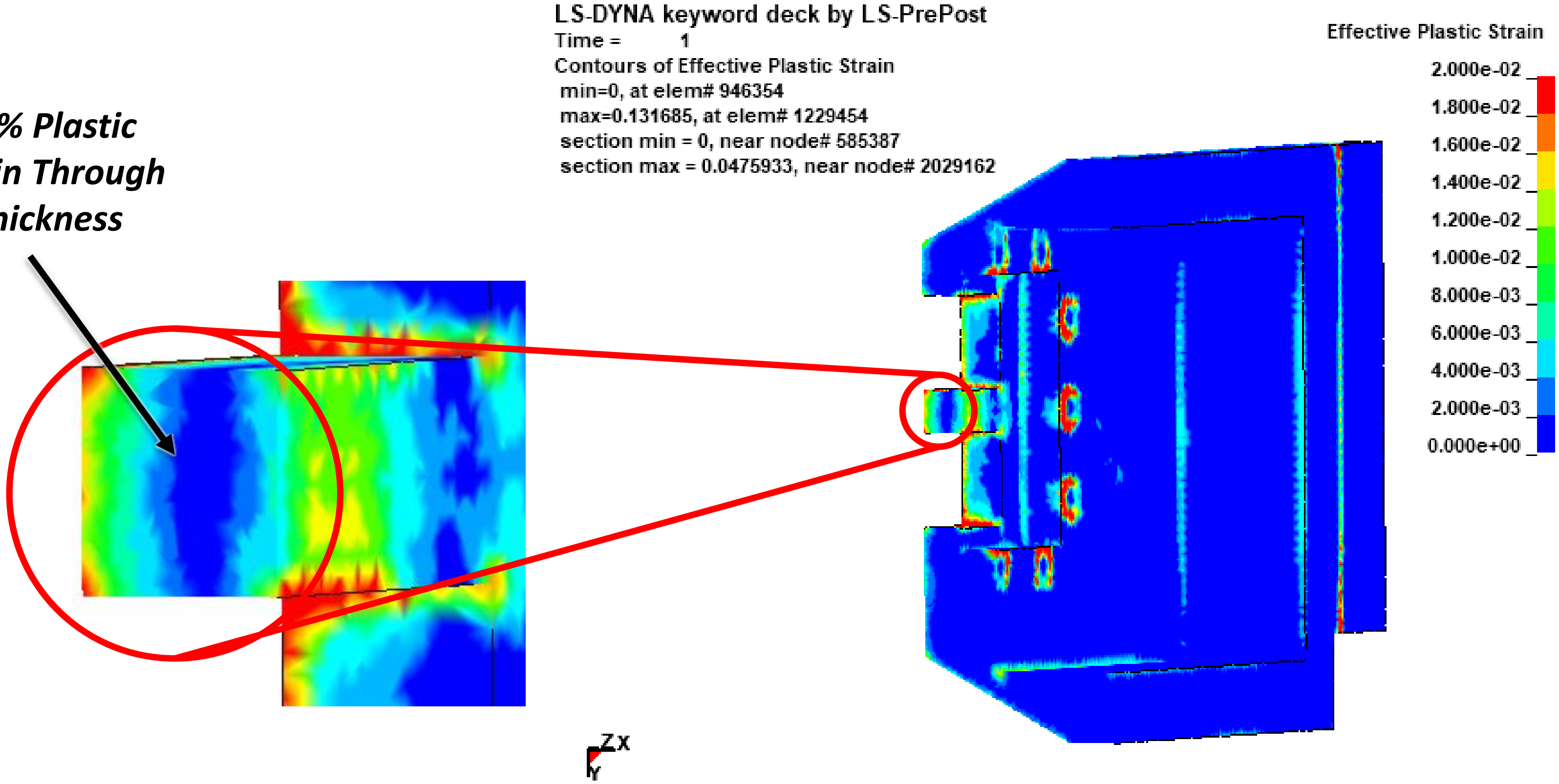

LS-DYNA keyword deck by LS-PrePost
Time = 1
Contours of Effective Plastic Strain
min=0, at elem# 946354
max=0.131685, at elem# 1229454
section min = 0, near node# 585387
section max = 0.0475933, near node# 2029162

Tantalum, Von Mises Stress Results

2.1 MJ Energy
1 g Mass
3 mm Polycarbonate

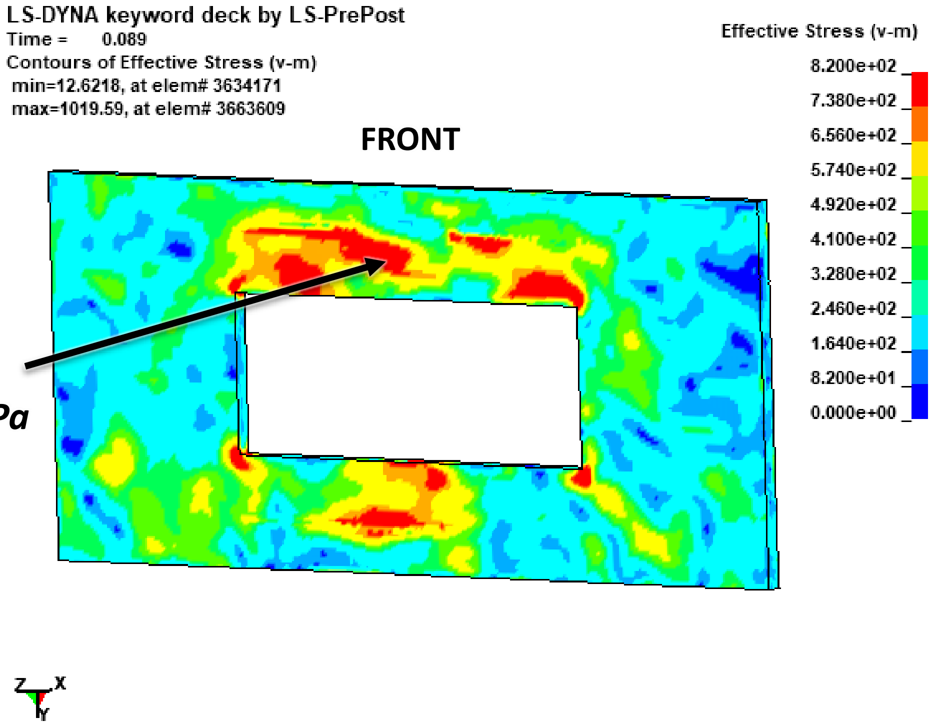

LS-DYNA keyword deck by LS-PrePost
Time = 0.089
Contours of Effective Stress (v-m)
min=12.6218, at elem# 3634171
max=1019.59, at elem# 3663609

Max
820 MPa

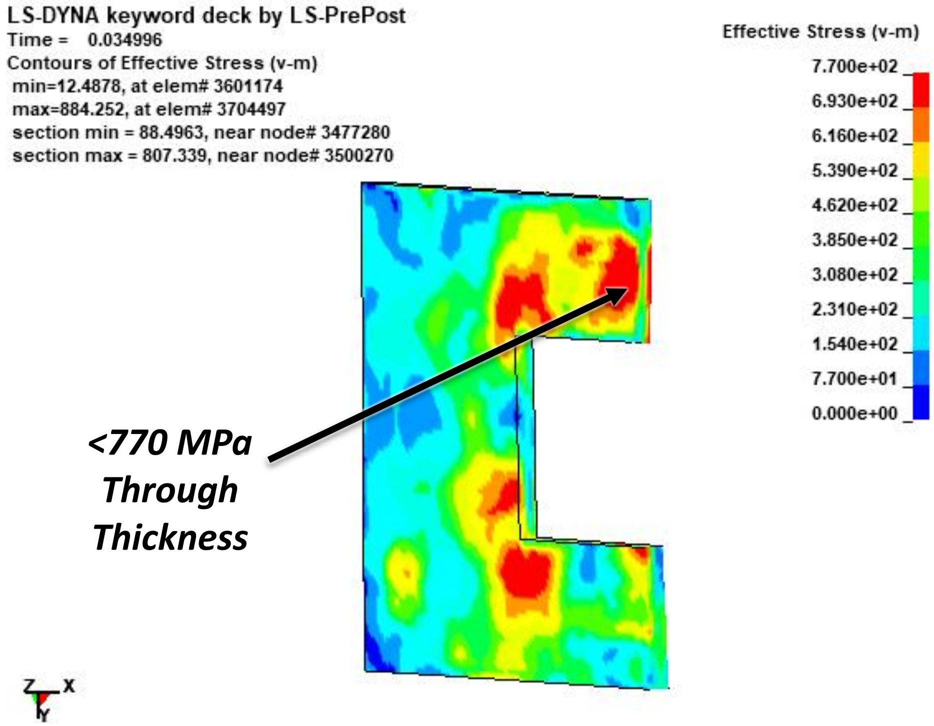

LS-DYNA keyword deck by LS-PrePost
Time = 0.034996
Contours of Effective Stress (v-m)
min=12.4878, at elem# 3601174
max=884.252, at elem# 3704497
section min = 88.4963, near node# 3477280
section max = 807.339, near node# 3500270

<770 MPa
Through
Thickness

Tantalum, Plastic Strain Results

2.1 MJ Energy
1 g Mass
3 mm Polycarbonate

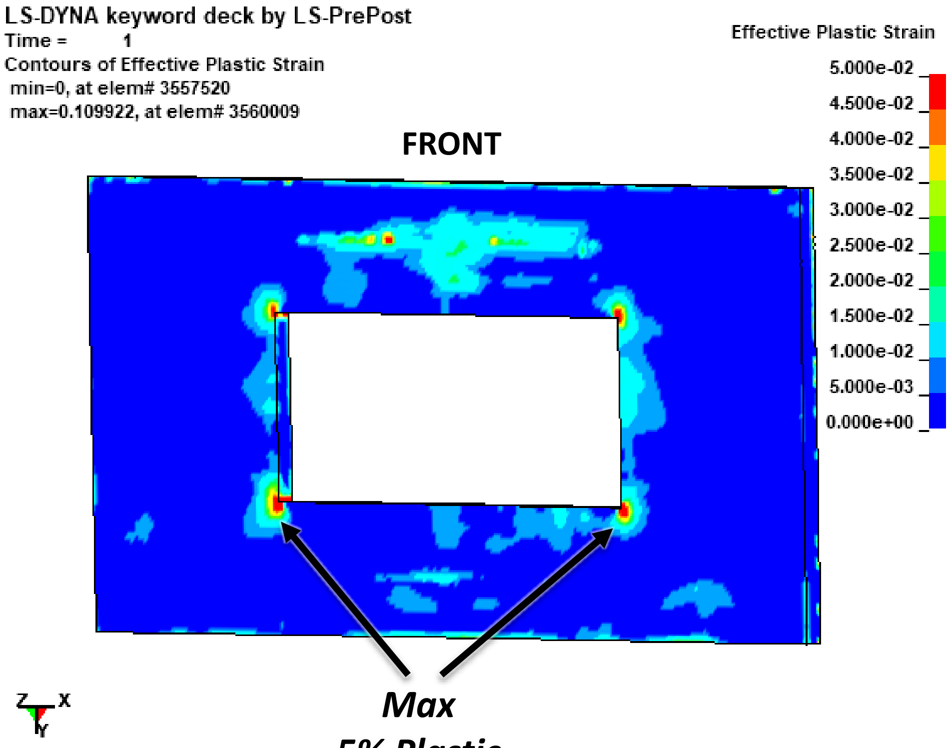

Max
5% Plastic
Strain

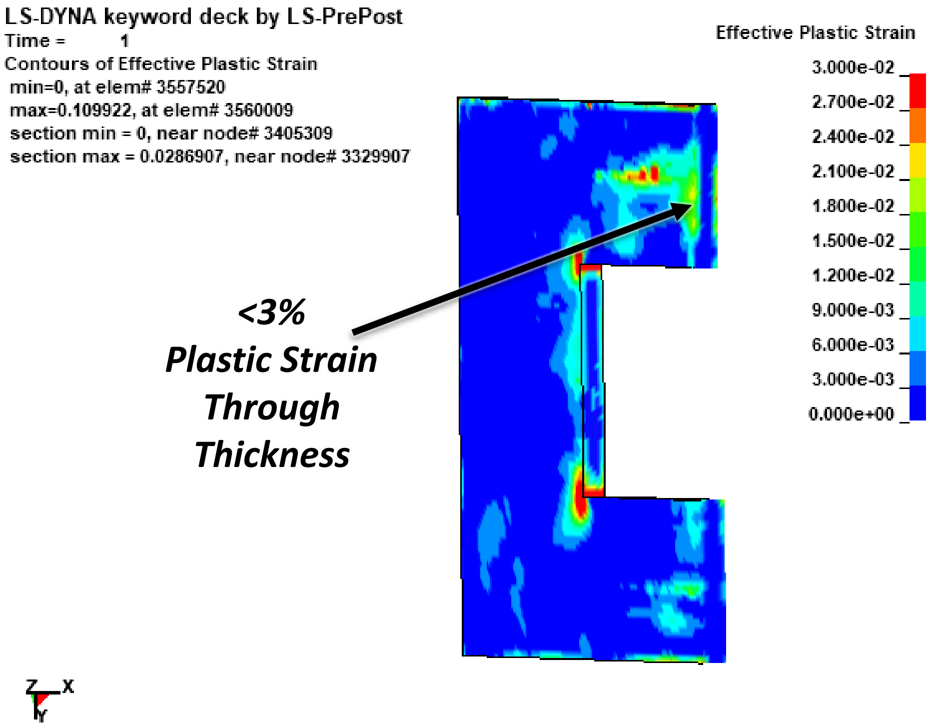

<3%
Plastic Strain
Through
Thickness

Retaining Cover, Von Mises Stress Results

2.1 MJ Energy
1 g Mass
3 mm Polycarbonate

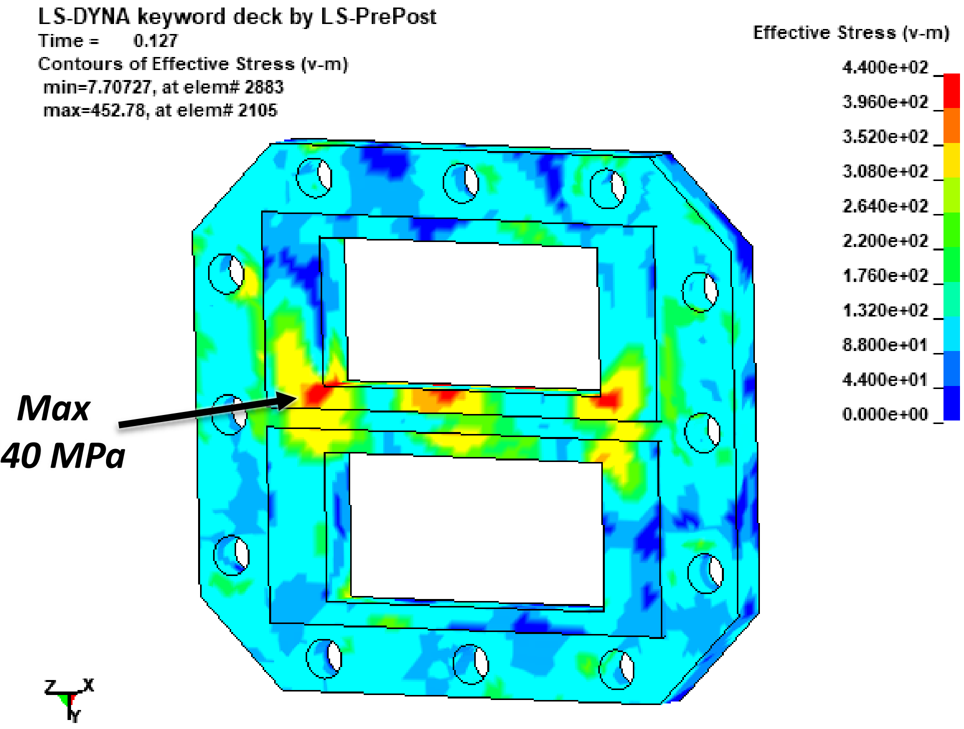

LS-DYNA keyword deck by LS-PrePost
Time = 0.127
Contours of Effective Stress (v-m)
min=7.70727, at elem# 2883
max=452.78, at elem# 2105

Max
440 MPa

FRONT

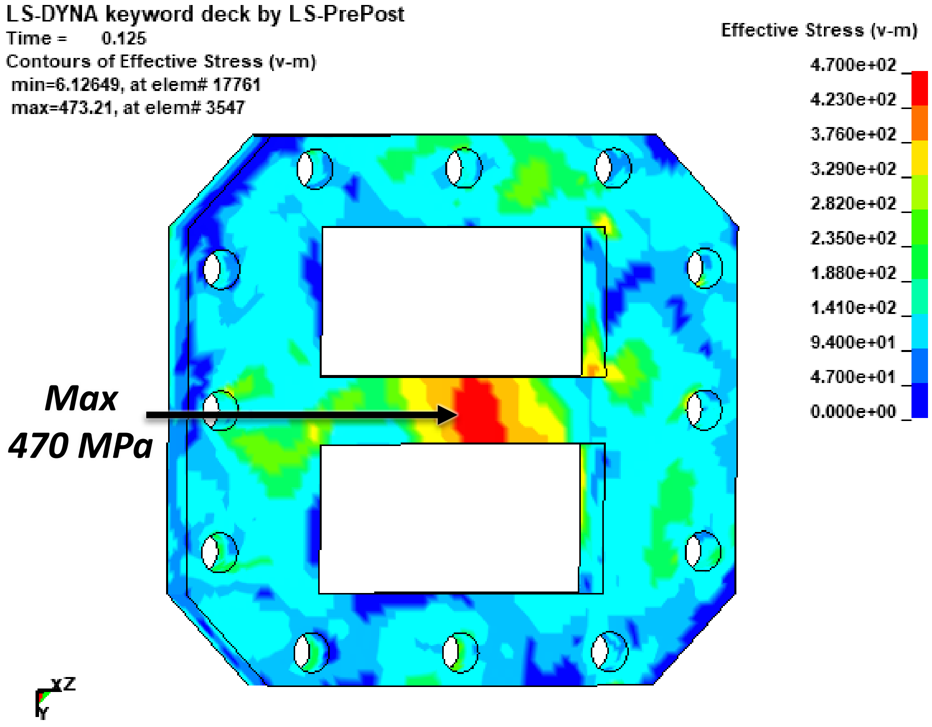

LS-DYNA keyword deck by LS-PrePost
Time = 0.125
Contours of Effective Stress (v-m)
min=6.12649, at elem# 17761
max=473.21, at elem# 3547

Max
470 MPa

REAR

Retaining Cover, Von Mises Stress Results Cont.

2.1 MJ Energy
1 g Mass
3 mm Polycarbonate

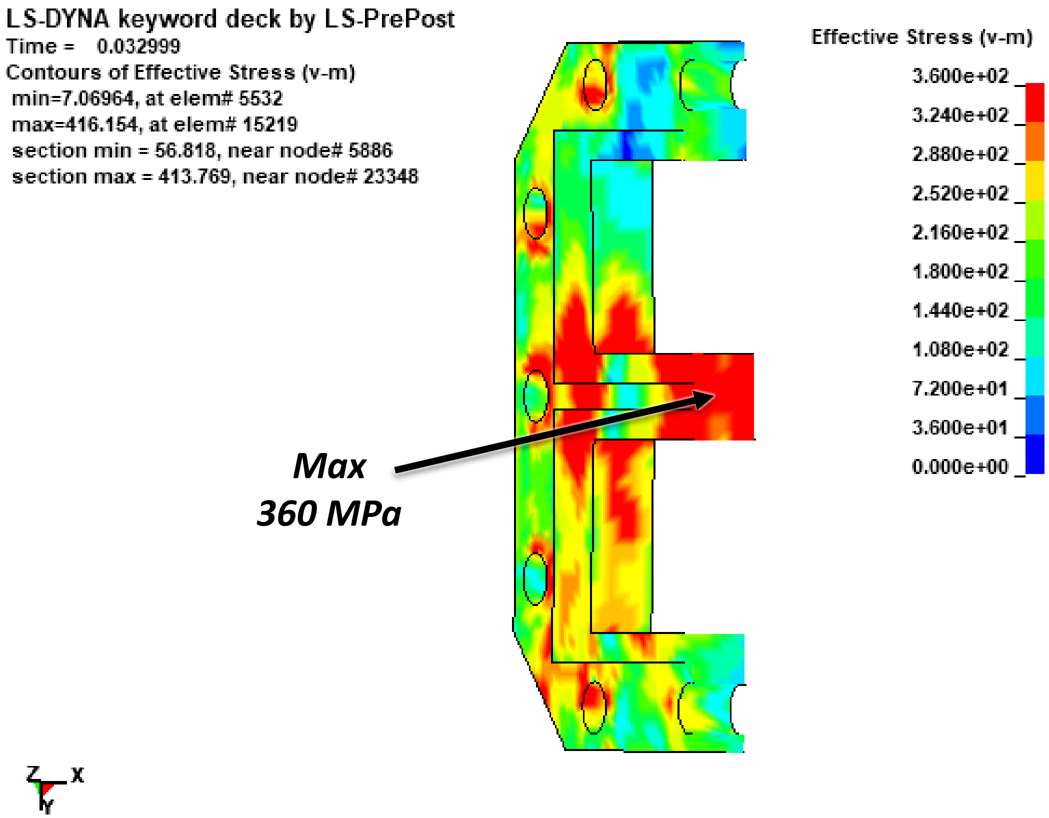

LS-DYNA keyword deck by LS-PrePost
Time = 0.032999
Contours of Effective Stress (v-m)
min=7.06964, at elem# 5532
max=416.154, at elem# 15219
section min = 56.818, near node# 5886
section max = 413.769, near node# 23348

Max
360 MPa

Retaining Cover, Plastic Strain Results

2.1 MJ Energy
1 g Mass
3 mm Polycarbonate

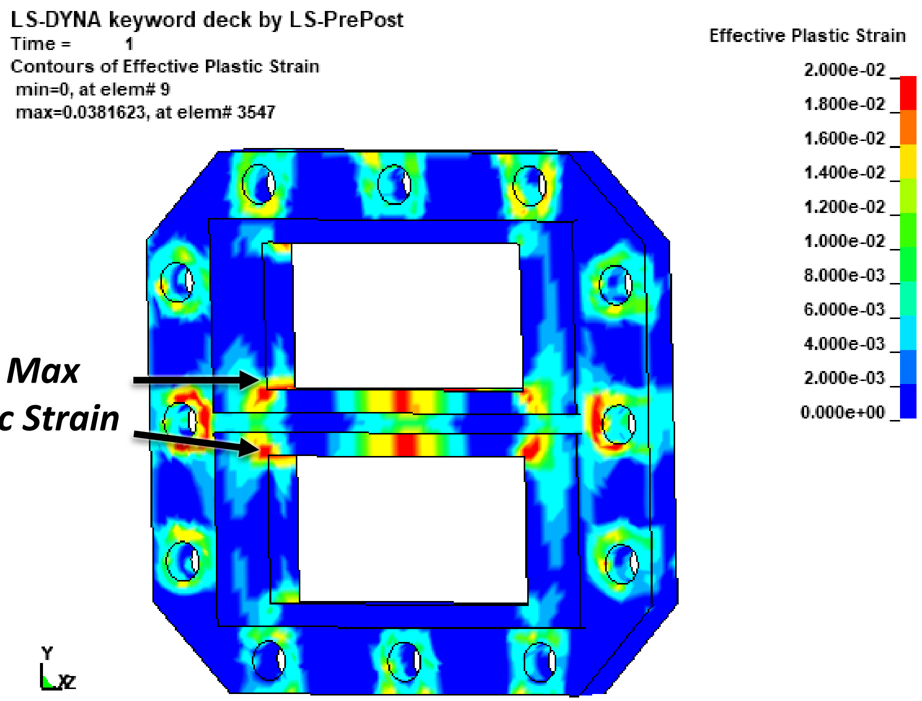

2% Max Plastic Strain

FRONT

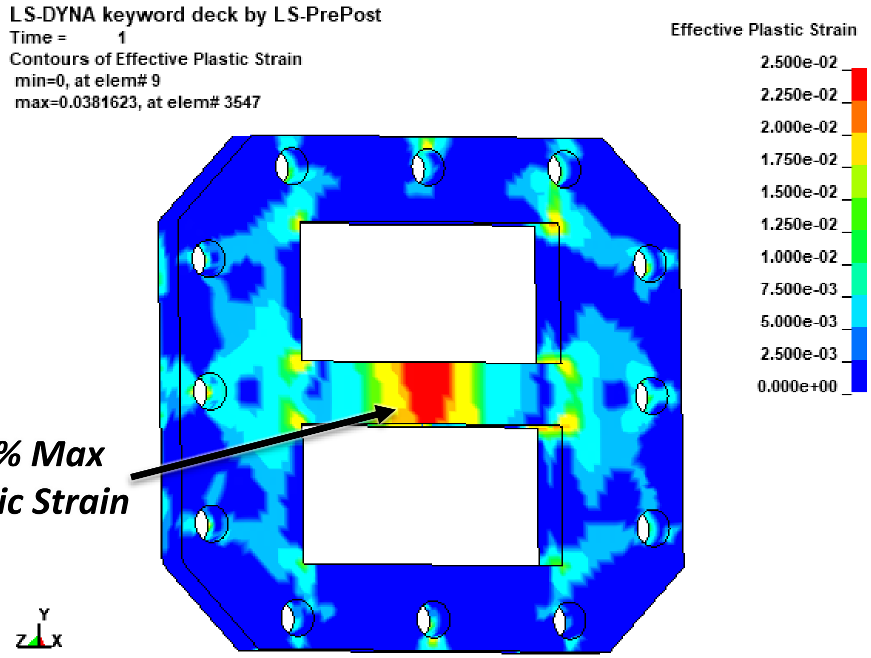

2.5% Max Plastic Strain

REAR

Retaining Cover, Plastic Strain Results Cont.

2.1 MJ Energy
1 g Mass
3 mm Polycarbonate

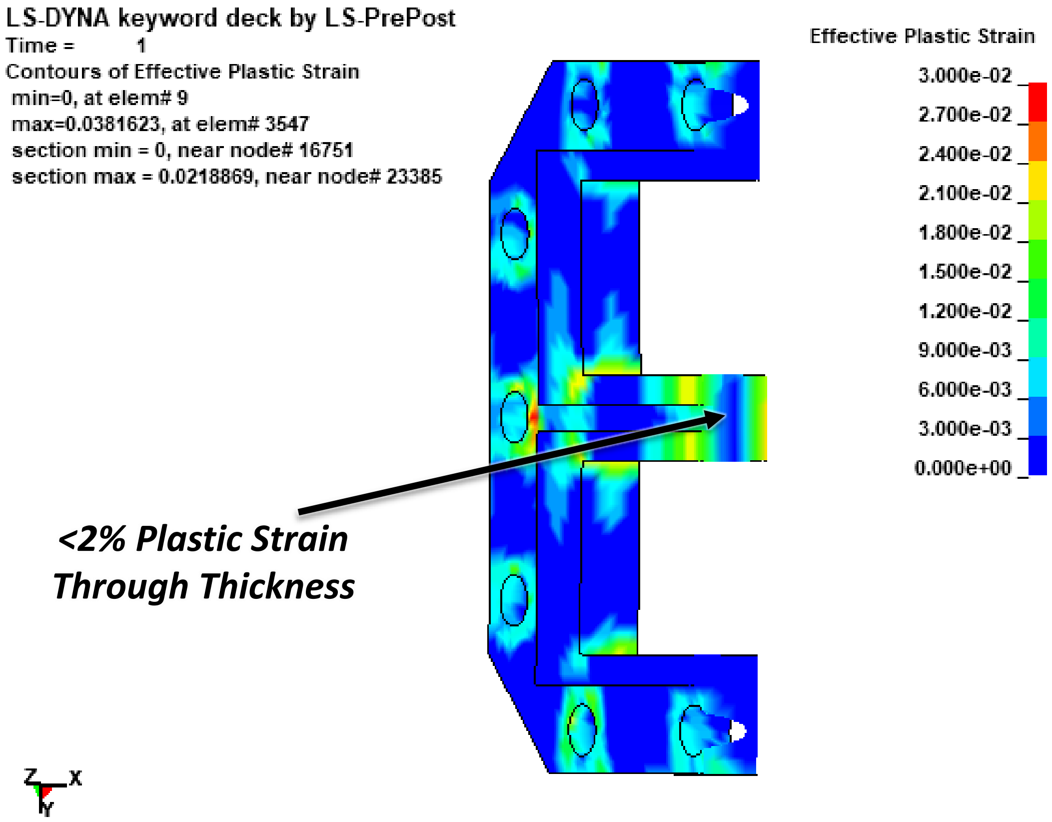

```
LS-DYNA keyword deck by LS-PrePost
Time =         1
Contours of Effective Plastic Strain
 min=0, at elem# 9
 max=0.0381623, at elem# 3547
 section min = 0, near node# 16751
 section max = 0.0218869, near node# 23385
```

<2% Plastic Strain
Through Thickness

Appendix C

FLEXURE HAND CALCULATIONS

C.1 Sizing Blade Flexure Length

Two separate hand calculations were performed to serve as a baseline for the design of the compact Biflex flexure. The first was based on calculations from Qingsong Xu's paper to determine the max travel range based on material properties and desired flexure size [30]. These calculations were based on flexible spring element displacement calculations. The relation used was:

$$x_N^{max} = \frac{N\sigma_y l^2}{3Eh} \tag{C.1}$$

Where:

N is the number of stacked parallel flexure units used

σ_y is the yield strength of the material

l is the length of the blade flexure

E is the Young's Modulus of the material

h is the blade flexure thickness

Since we know the desired travel range of the flexures, the relation can be rearranged to solve for the required blade flexure length:

$$l = \sqrt{\frac{3x_N^{max}Eh}{N\sigma_y}} \tag{C.2}$$

The material properties for Titanium 6AL-4V are listed as: $E = 113.8$ GPa, $\sigma_y = 880$ MPa, and since the Biflex is only one stacked unit N was set to 1. For a wire EDM process, thicknesses of 0.25 mm are possible, so this value was selected to maximize performance. With a maximum desired travel of 2 mm the blade flexure length can be solved for:

$$l = \sqrt{\frac{3(2mm)(113.8 * 10^3 MPa)(0.25mm)}{(1)(880MPa)}}$$

$$l = 13.92mm$$

For simplicity the blade flexure length was rounded to 14 mm. To also have some factor of safety the displacement of the flexures was reduced to 1.5 mm.

C.2 Estimating Stress Developed in Blade Flexures

The second set of hand calculations performed was to estimate the stress developed near the joints of the blade flexures. Roark's equations were leveraged to estimate the stress developed with a provided deflection [38].

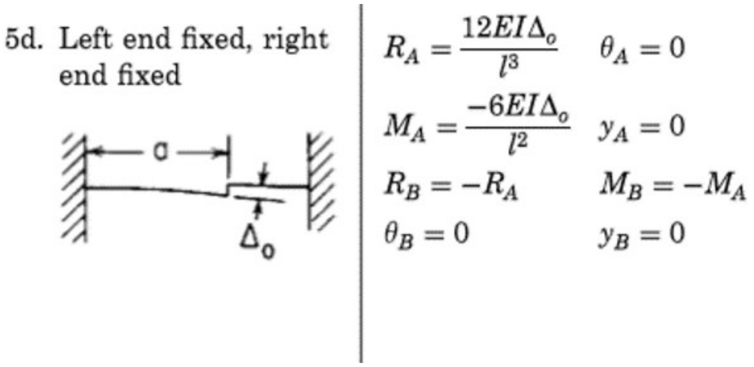

5d. Left end fixed, right end fixed

$R_A = \frac{12EI\Delta_o}{l^3}$ $\theta_A = 0$

$M_A = \frac{-6EI\Delta_o}{l^2}$ $y_A = 0$

$R_B = -R_A$ $M_B = -M_A$

$\theta_B = 0$ $y_B = 0$

Figure C.1: Left end fixed, right end fixed Beam Model [38]

The end reaction and moment were calculated and then used to determine the max normal and shear stress developed. The parameters used in these equations are:

E is the Young's Modulus of the material

I is the moment of inertia of the cross section

Δ_0 is the displacement of the flexure

l is the length of the blade flexure

Most of the material and system parameters can be borrowed from the previous hand calculation. The moment of inertia for the cross section needs to be calculated for the flexure. For a rectangular cross section the moment of inertia is calculated as:

$$I = \frac{bh^3}{12} \tag{C.3}$$

For the flexure, the base is 8 mm (the true height of the flexure) and the height corresponds to the blade flexure thickness of 0.25 mm. The moment of inertia is calculated to be:

$$I = \frac{((8mm)(0.25mm)^3)}{12}$$

$$I = 0.01mm^4$$

Using the same material properties listed in the previous hand calculation, the moment and reactions can be calculated as follows.

Reactions:

$$R_a = \frac{12EI\Delta_0}{l^3} \tag{C.4}$$

$$R_a = \frac{(12(113.8 * 10^3 MPa)(0.01mm^4)(1.5mm))}{(14mm)^3.}$$

$$R_a = 7.77N$$

Moments:

$$M_a = \frac{(-6EI\Delta_0)}{l^2} \tag{C.5}$$

$$M_a = \frac{(-6(113.8 * 10^3 MPa)(0.01mm^4)(1.5mm))}{(14mm)^2}$$

$$M_a = -54.43N - mm$$

The maximum normal stress can be calculated from:

$$\sigma_N = \frac{Mc}{I} \tag{C.6}$$

Where c is the distance from the center of the cross section to the vertical outer surface. For the flexures, c would be half of the blade flexure thickness. The normal stress developed can be calculated as:

$$\sigma_N = \frac{((-54.43N - mm)(0.125mm)}{(0.01mm^4)}$$

$$\sigma_N = 653.2MPa$$

The maximum shear stress for rectangular cross sections can be found through the relation:

$$\tau_s = \frac{3V}{2A}$$

For our system parameters this is calculated as:

$$\tau_s = \frac{3(7.77N)}{2(0.25mm)(8mm)}$$

$$\tau_s = 5.83MPa$$

Finally, the Von-Mises stress can be calculated based on the in-plane stress:

$$\sigma_{vm} = \sqrt{\sigma_N^2 + 3\tau_s^2} \tag{C.7}$$

The Von-Mises stress was calculated to be:

$$\sigma_{vm} = \sqrt{(653.2MPa)^2 + 3(5.83MPa)^2}$$

$$\sigma_{vm} = 653.3MPa$$

As expected the normal stress dominates in terms of calculating the Von-Mises stress. Comparing to the yield strength of Titanium 6AL-4V a factor of safety can be calculated.

$$N = \frac{\sigma_y}{\sigma_{vm}} \tag{C.8}$$

$$N = \frac{(880MPa)}{(653.3MPa)}$$

$$N = 1.35$$

To produce a higher factor of safety, the blade flexure length can be increased or the overall range of travel can be decreased depending on the need. This blade flexure length was used to model the Biflex design.